UNIVERSITY OF CALIFORNIA,
IRVINE

Nanowire Spin Hall Oscillators

DISSERTATION

submitted in partial satisfaction of the requirements
for the degree of

DOCTOR OF PHILOSOPHY

in Physics

by

Andrew Smith

Dissertation Committee:
Professor Ilya Krivorotov, Chair
Assistant Professor Matt Law
Professor Peter Taborek

2016

TABLE OF CONTENTS

LIST OF FIGURES

ACKNOWLEDGMENTS

I would like to express my gratitude to my committee chair, Dr. Ilya Krivorotov, for allowing me to commence my journey of self discovery and scientific insight under his guidance. A half decade latter and I am still surprised by the breadth of his knowledge, intuition and leadership. I would also like to thank my committee members, Dr. Matt Law and Dr. Peter Taborek for taking time out of their busy schedules to help me accomplish this daunting task.

I would like to thank everyone that I had the pleasure to call a labmate over the years: Dr. Jian Zhu, Dr. Graham Rowlands, Dr. Zheng Duan, Dr. Igor Barsukov, Dr. Brian Youngblood, Dr. Liu Yang, Yu-Jin Chen, Han Kyu Lee, Jenru Chen, Jieyi Zhang, Alejandro Jara, Chris Safranski, Chengcen Sha, Dr. Eric Montoya, Josh Dill, Alexandre Goncalves, Riccardo Tomasello and Tobias Schneider. Whether it be scientific or social needs, there was always a helping hand. I would also like to thank my collaborators including Dr. Jurgen Linder, Dr. Vladislav E. Demidov, Dr. Sergej O. Demokritov, Dr. Roman Verba, Dr. Vasil Tiberkevich, Dr. Andrei N. Slavin, Dr. Rodrigo Arias and Kemal Sobotkiewich. I would like to thank the staff members of LEXI and INRF that have helped me fabricate and characterize samples throughout the years with special recognition to Dr. Qiyin Lin for your XRD expertise and Mo Kebaili, Jake Hes and Ryan Smith for all of the clean room assistance. I would like to acknowledge Nature Communications for allowing the use of "Nanowire spin torque oscillator driven by spin orbit torques" for chapter 4 of this dissertation.

I would also like to thank my friends and family for haboring my escape from grad school in times of need. Whether they were near or far, their love, support and joyfulness was always felt. Lastly, I would like to thank my girlfriend, Dr. Amanda Weber, for without her infectious brightness and unending support, this would not be possible. In the most stressful moments, you were always there to listen to me rant and encourage me to push through or take a step back and relax.

CURRICULUM VITAE

Andrew Smith

EDUCATION

Doctor of Philosophy in Chemical and Materical Physics **2016**
University of California, Irvine *Irvine, California*

Master of Science in Chemical and Materical Physics **2016**
University of California, Irvine *Irvine, California*

Bachelor of Science in Physics **2010**
Marquette University *Milwaukee, Wisconsin*

RESEARCH EXPERIENCE

Graduate Research Assistant **2011–2016**
University of California, Irvine *Irvine, California*

Undergraduate Research Assistant **2008–2009**
Marquette University *Milwaukee, Wisconsin*

TEACHING EXPERIENCE

Teaching Assistant **2010–2011**
University of California, Irvine *Irvine, California*

Teaching Assistant **2007–2010**
Marquette University *Milwaukee, Wisconsin*

REFEREED JOURNAL PUBLICATIONS

L. Yang, R. Verba, V. Tiberkevich, T. Schneider, **A. Smith**, et al. Reduction of phase noise in nanowire spin orbit torque oscillators. *Sci. Rep.* 5, 16942 (2015)

Z. Duan*, **A. Smith***, L. Yang*, B. Youngblood*, et al. Nanowire spin torque oscillator driven by spin orbit torques. *Nat. Commun.* 5:5616 (2014)

Andrew Kunz, Eric C. Breitbach and **Andrew Smith**. Anti-vortex dynamics in magnetic nanostripes. *Journal of Applied Physics.* 105, 07D502 (2009)

REFEREED CONFERENCE PUBLICATIONS

Andrew Smith, Tobias Schneider, Liu Yang, Zheng Duan and Ilya N. Krivorotov. Dimensional crossover in spin Hall oscillators. *American Physics Society - March Meeting.* Oral (2016)

Andrew Smith, Tobias Schneider, Liu Yang, Zheng Duan and Ilya N. Krivorotov. Dimensional crossover in spin Hall oscillators. *Magnetism and Magnetic Materials.* Poster (2016)

Andrew Smith, Liu Yang, Brian Youngblood, Zheng Duan and Ilya N. Krivorotov. Time domain measurements of a spin torque oscillator driven by spin orbit torques. *Magnetism and Magnetic Materials.* Oral (2014)

Andrew Smith, Zheng Duan, Liu Yang, Brian Youngblood and Ilya N. Krivorotov. Nanowire spin torque oscillator driven by spin orbit torques. *American Physics Society - March Meeting.* Oral (2014)

ABSTRACT OF THE DISSERTATION

Nanowire Spin Hall Oscillators

By

Andrew Smith

Doctor of Philosophy in Physics

University of California, Irvine, 2016

Professor Ilya Krivorotov, Chair

The field of spintronics deals with the use of the spin degree of freedom of the electron and the spin current that arises from it. There are many static and dynamic applications for spin current whether it is supplied by spin polarized electric current from a magnetic layer or from pure spin current arising from spin orbit interaction such as the spin Hall effect. This dissertation focuses on the later where the spin Hall effect in platinum supplies a spin torque on an adjacent ferromagnetic layer and thereby excites auto-oscillations of its magnetization. Previous studies of magnetization dynamics excited by direct spin currents have demonstrated the existence of phase coherent auto-oscillations of magnetization in the 0-dimensional structures and its absence in the 2D case therefore the 1D case, a ferromagnetic nanowire, is presented here. This will cover the first instance of a micrometer scale STO and will show the excited modes are the edge and bulk spin wave eigenmodes of the nanowire. Additionally, the evolution of the auto-oscillation characteristics as the width of the wire is increased is shown which reveals the mechanisms of the auto-oscillation suppression as the system effective dimensionality crosses of over from the 1D to the 2D regime. Lastly, a novel type of spin torque oscillator with easy plane magnetic anisotropy is discussed; its properties are predicted via micromagnetic simulations and initial experimental data on this type of oscillator are presented.

Chapter 1

Introduction

Spintronics has become an important branch of condensed matter physics for a reason. In metals with low spin orbit coupling (SOC), the spin of the electrons are orientated randomly resulting in no spin current when electric current is applied. However, if the material is magnetic or has large SOC, the spins become polarized when electric current is applied thus resulting in a spin current. These spin currents can then interact with other magnetic layers via spin transfer torque (STT) allowing for local manipulation of magnetic moments. The origin of this interaction is rooted in the exchange interaction between the quasi-localized d-electrons and the spin polarized, conduction s-electrons which results in a torque that aligns the two. This can result in the rotation of the magnetization towards the spin current polarization or can modify the effective Gilbert damping of the magnetization. Additionally, if the spin current has periodicity in the microwave range, STT can excite the spin wave eigenmodes of the magnetic system.

By utilizing the the spin degreee of freedom of an electron, new nanoscale devices are now possible. One example is spin transfer torque magnetic random access memory (STT-MRAM)[1–3] where a free magnetic layer is switched parallel or antiparallel to a reference

magnetic layer by STT from a sufficiently large voltage pulse across the device. The state is then read by tunneling magnetoresistance which has low resistance (0) when the layers are parallel and high resistance (1) when anitparallel thus creating a binary memory cell. Another example is magnetic logic circuits[4–6] where domain walls encode the information. Different types of logic circuits can be created like shift registers and full-adders by sourcing spin current locally which drives domain wall motion.

The device of focus in this thesis is the spin torque oscillator (STO) where the Gilbert damping of a magnetic layer is cancelled out by the spin torque from a spin current which leads to self-oscillatory dynamics in the GHz range. The type of STO covered here is a nanowire spin Hall oscillator (SHO) in which the spin current is supplied by a platinum (Pt) layer and is injected into an adjacent ferromagnetic layer. In order to readout the magnetization electrically, anisotropic magnetoresistance is utilized which has a $\cos^2(\theta)$ dependence on the angle θ between the magnetization and the electrical current. The auto-oscillations of the magnetization will then result in an oscillatory magnetoresistance which combined with the electric current running through the sample, will generate a microwave voltage.

STO are one of the smallest auto oscillators in the world[7] (as small as 50 nm) and have garnered interest from industry for applications such as on-chip local oscillators, associative memory blocks for image processing, nanoscale magnetic field sensing[8], logic devices and many more. The ideal STO has high output power ($\sim$ 1 mW to drive RF block[7]), narrow linewidths (<1 Hz[9,10]), and low operational currents and voltages (<1 V for complementary metal-oxide-semiconductor compatability[11]). No STO to date has achieved all 3 aspects therefore the exploration of different archetypes of STO is needed.

Chapter 2 will cover the background material needed to understand the results of this work. It includes a phenomenological description of STT, how to generate spin currents, and illustrates the different structures used for spintronic devices and their associated magnetoresistances. Additionally, the equations that govern magnetization dynamics and how

they are solved is covered. The tools used to characterize SHO and the previous work done is discussed too.

Chapter 3 provides recipes and instructions on how to perform the necessary tasks utilized in the work presented. It includes the basics of e-beam lithography and ion milling necessary to fabricate devices. Recipes for the growth of textured Pt seed layers and the full nanofabrication details needed for SHO are provided too. Additionally, instructions on how to detect the auto-oscillations of a STO and characterize the device with spin torque ferromagnetic resonance (ST-FMR) is provided.

Chapter 4 discusses the interesting role dimensionality plays in a SHO. It shows the microwave emission from a 0.19 μm wide Pt/Permalloy(Py=$Ni_{80}Fe_{20}$ nanowire at various magnetic fields, angles, and bath temperatures. Also, finite bias ST-FMR and micro-focused Brillouin light scattering is used to show that the self-oscillatory states are the spin wave eigenmodes of the nanowire.

Chapter 5 covers 1-dimensional to 2-dimensional crossover in the behavior of the nanowire SHO. The microwave emission from 0.17, 0.34, 0.53, 1.17, and 2.11 μm wide Pt/Py nanowire SHOs is shown. The spatial profiles of the spin wave eigenmodes and self-oscillatory modes are micromagnetically calculated. Additionally, the angular and temperature dependence of the integrated power and critical current is shown for the 0.53 μm wide wire.

Chapter 6 presents a new type of STO with easy plane magnetic anisotropy that significantly increase the output power of the oscillator. The self-oscillatory dynamics are micromagnetically calculated for a 45 nm wide Pt/cobalt/nickel nanowire for different oscillator sizes and magnetic anisotropies. Additionally, preliminary microwave emission measurements and what follows next is reported. Chapter 7 concludes the thoughts of this thesis.

Bibliography

[1] Yiming Huai et al. "Observation of spin-transfer switching in deep submicron-sized and low-resistance magnetic tunnel junctions". In: *Applied Physics Letters* 84.16 (2004), p. 3118. DOI: 10.1063/1.1707228. URL: http://dx.doi.org/10.1063/1.1707228.

[2] Guenole Jan et al. "Achieving Sub-ns switching of STT-MRAM for future embedded LLC applications through improvement of nucleation and propagation switching mechanisms". In: *2016 IEEE Symposium on VLSI Technology*. Institute of Electrical and Electronics Engineers (IEEE), 2016. DOI: 10.1109/vlsit.2016.7573362. URL: http://dx.doi.org/10.1109/VLSIT.2016.7573362.

[3] Chando Park et al. "Temperature Dependence of Critical Device Parameters in 1 Gbit Perpendicular Magnetic Tunnel Junction Arrays for STT-MRAM". In: *IEEE Transactions on Magnetics* (2016), pp. 1–1. DOI: 10.1109/tmag.2016.2615816. URL: http://dx.doi.org/10.1109/TMAG.2016.2615816.

[4] J. A. Currivan-Incorvia et al. "Logic circuit prototypes for three-terminal magnetic tunnel junctions with mobile domain walls". In: *Nature Communications* 7 (2016), p. 10275. DOI: 10.1038/ncomms10275. URL: http://dx.doi.org/10.1038/ncomms10275.

[5] D. A. Allwood. "Magnetic Domain-Wall Logic". In: *Science* 309.5741 (2005), pp. 1688–1692. DOI: 10.1126/science.1108813. URL: http://dx.doi.org/10.1126/science.1108813.

[6] Jean Anne Currivan et al. "Low Energy Magnetic Domain Wall Logic in Short, Narrow, Ferromagnetic Wires". In: *IEEE Magnetics Letters* 3 (2012), pp. 3000104–3000104. DOI: 10.1109/lmag.2012.2188621. URL: http://dx.doi.org/10.1109/LMAG.2012.2188621.

[7] Patrick Villard et al. "A GHz Spintronic-Based RF Oscillator". In: *IEEE Journal of Solid-State Circuits* 45.1 (2010), pp. 214–223. DOI: 10.1109/jssc.2009.2034432. URL: http://dx.doi.org/10.1109/JSSC.2009.2034432.

[8] P M Braganca et al. "Nanoscale magnetic field detection using a spin torque oscillator". In: *Nanotechnology* 21.23 (2010), p. 235202. DOI: 10.1088/0957-4484/21/23/235202. URL: http://dx.doi.org/10.1088/0957-4484/21/23/235202.

[9] Shingo Tamaru et al. “Extremely Coherent Microwave Emission from Spin Torque Oscillator Stabilized by Phase Locked Loop”. In: *Sci. Rep.* 5 (2015), p. 18134. DOI: 10.1038/srep18134. URL: http://dx.doi.org/10.1038/srep18134.

[10] Shingo Tamaru et al. “Analysis of phase noise in a spin torque oscillator stabilized by phase locked loop”. In: *Appl. Phys. Express* 9.5 (2016), p. 053005. DOI: 10.7567/apex.9.053005. URL: http://dx.doi.org/10.7567/APEX.9.053005.

[11] Hsieh-Hung Hsieh and Liang-Hung Lu. “A High-Performance CMOS Voltage-Controlled Oscillator for Ultra-Low-Voltage Operations”. In: *IEEE Transactions on Microwave Theory and Techniques* 55.3 (2007), pp. 467–473. DOI: 10.1109/tmtt.2006.891471. URL: http://dx.doi.org/10.1109/TMTT.2006.891471.

Chapter 2

Background

2.1 Spin Transfer Torque

The concept of spin transfer torque (STT) was first proposed by Slonczewski[12] and Berger[13] in 1996. The equation describing STT when a spin current is injected into a ferromagnetic layer is

$$\tau_{ST} = \left|\frac{\hbar}{\mu_o e}\right| \frac{J}{dM_s} \frac{P\Lambda^2}{(\Lambda^2+1)+(\Lambda^2-1)(\mathbf{m}\cdot\mathbf{p})} (\mathbf{m}\times\mathbf{m}\times\mathbf{p} + C\mathbf{m}\times\mathbf{p}) \tag{2.1}$$

where $\hbar$ is the reduced Planck constant, μ_o is the permeability of free space, e is the charge of the electron, J is the current density, d is the thickness of the magnetic material, M_s is the saturation magnetization, P is the spin current polarization, Λ is the spin torque asymmetry parameter, $\mathbf{m}$ is magnetization unit vector, $\mathbf{p}$ is the spin current polarization unit vector, and C is the ratio between the damping-like spin torque (the first term) and the field-like spin torque (the second term). The damping-like term describes the longitudinal component of the STT which aligns the magnetization with the spin polarization axis. Additionally, The functional form of this term allows STT to modify the damping of the magnetic system

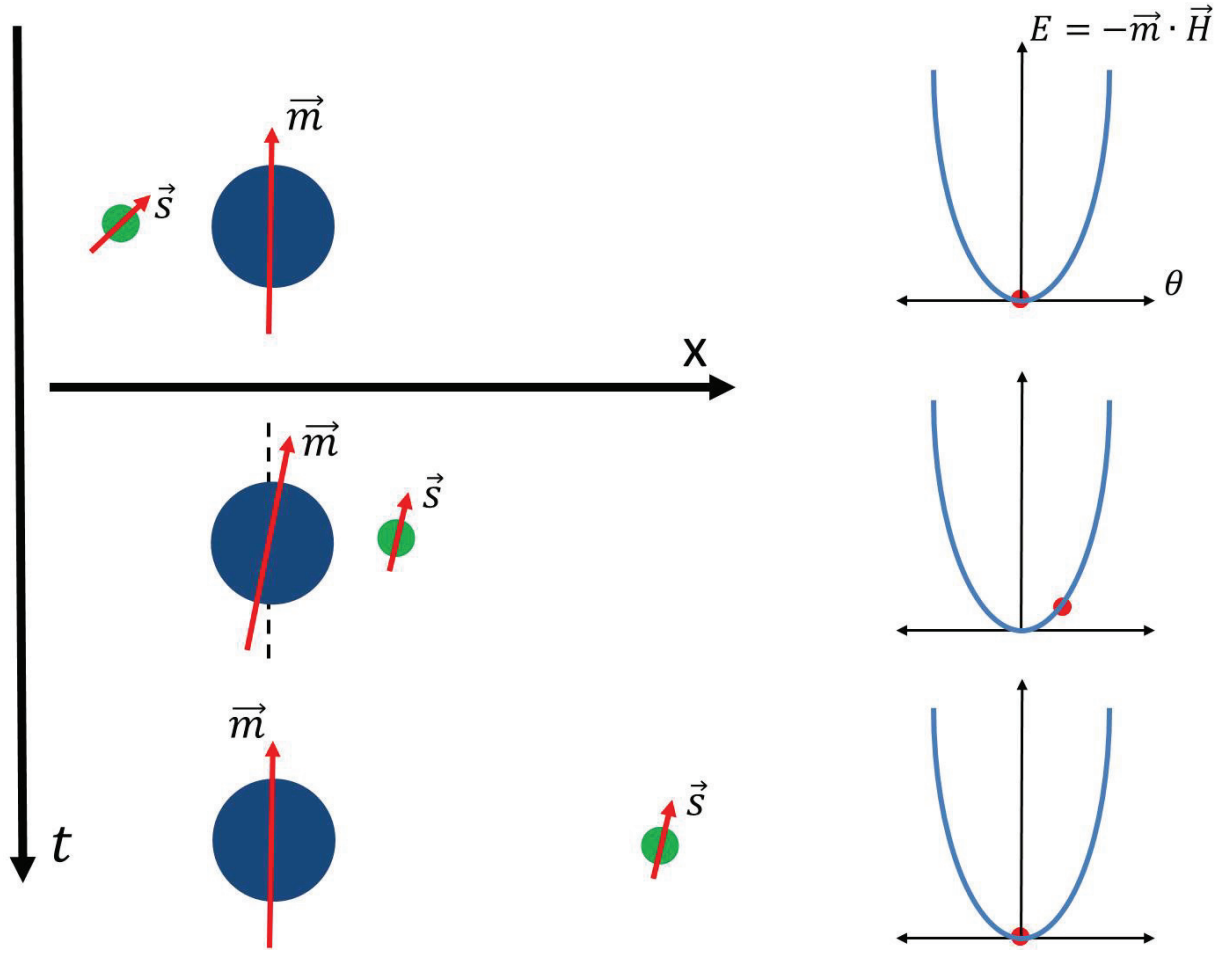

Figure 2.1: **Spin transfer torque.** Illustration of spin torque where conduction electron and localized magnetic moment exert torques on each other which temporarly shifts the moment away from equalibrium. The Zeeman energy as a function of the localized moment angle relative to the applied magnetic field is shown on right for each stage.

which will be discussed in more detail in Sec. 2.5. The field-like torque term (FLT) describes the transverse component of the STT which causes the magnetization to precess about the spin polarization direction. This term is typically less than the damping-like term and can be small enough that it can be ignored in some cases.

The origins of STT is best understood in the framework of exchange interactions between quasi-localized and conduction electrons as illustrated in Fig. 2.1. The local d electron responsible for ferromagnetism of a material are initially with its spin aligned with the local magnetic field which minimizes the Zeeman energy. When a conduction electron

that is polarized in a different direction than the local moment passes by, the two spins exert torque onto each other due to the exchange interaction. This causes both electrons to deflect from their original directions, which has two consenquences. The first is that the conduction electron will leave the site with the spin information of the local moment which can then interact with other local moments. Secondly, the local moment will now be tilted away from the energy minimum and subsequently relaxes to its ground state.

If now there is a constant flow of electrons with the spins polarized along a given direction, then the local moment will be continuously kicked in that direction and will remain there as long as the current is present. Once the current is removed, the local moment will then return back to an energy minimum. In the case of a constant flow of electrons but the spins are polarized in random directions, then the local moment will be kicked around in random directions which average out to 0 leading to the moment staying aligned along the local magnetic field. In either case, this incident electric current will then be converted into electric and spin current with its polarization in the direction of the local moment which can then be used to tilt magnetization of another ferromagnetic layer.

2.2 Generation of Spin Current

2.2.1 Spin Polarizer

A spin valve, shown in Fig. 2.2, consists of a normal metal (NM)/ferromagnetic metal (FM)/NM stack where the FM is relatively thick ($\sim$ 10 nm) and thus called the fixed layer. When electric current is applied through the sample, the spins of the electrons before the FM are orientated randomly. As the electrons encounter the interface between the NM and FM, the electrons spin polarized parallel to the FM magnetization (spin up) can easily pass through while the anti-parallel spins (spin down) are reflected back due to the increased

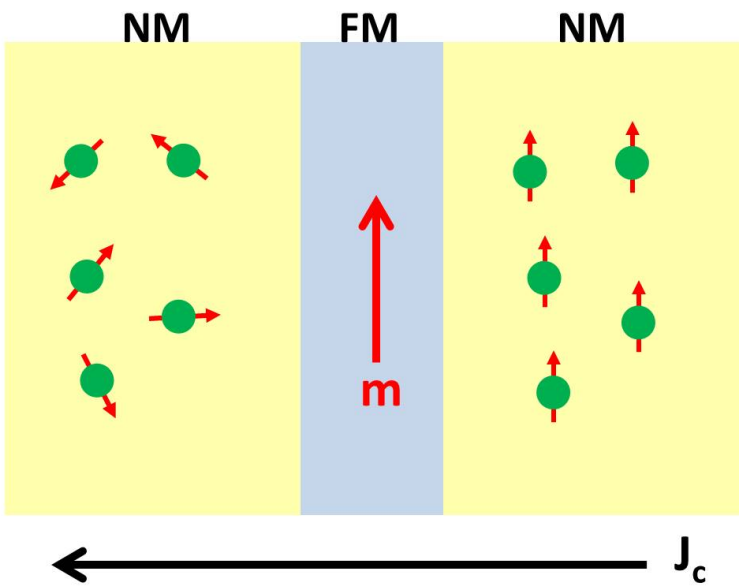

Figure 2.2: **Spin polarizer.** Illustration of a spin polarizer where electric current is applied right to left through a NM/FM/NM stack resulting in the electrons flowing left to right and becoming spin polarized.

(decreased) density of states of the spin up (down) conduction bands compared to the NM. The electrons then move to the next NM and maintain the spin orientation thus creating a spin current. The efficiency of this spin polarization processs is called the spin current polaration, P, such that when all of the spins of the conductions are spin up, then P = 1 and if all of them are down, P = -1[14]. Additionally, the reflected electrons create a spin current that has an opposite spin polarity and is in the opposite direction. The ratio of magnetitude of this backflow spin current to the foward flow spin current is described by the assymmetry parameter, Λ, as shown in Eq. (2.1). Therefore, the polarity of the spin current is determined by the polarity of the electrical current. This spin current decays over a characteristic length called the spin diffusion length due to spin flip events that take place in the NM therefore this layer is commonly $\sim$ 1-100 nm.

Spin polarizers are commonly used in conjunction with another FM layer of interest called the free layer resulting in a spin valve. This layer is typically thinner than the fixed layer so that the spin torque is larger in the free layer than the fixed layer as seen in Eq. (2.1)

since both layers will generate a spin current and thus, enact a spin torque on each other. Often times, the fixed layer consists of additional layers that help increase the coericive field, the magnetic field necessary to switch a ferromagnetic layer, in order to improve the stability of the magnetization direction of the fixed layer. Now the spin current polarization of the spin current in this structure depends on the spin dependent band structure of the whole system. As the spin polarized conduction electrons pass through the structure, spin flip and reflection events take place predominately at interfaces and are governed by the band structure mismatch of the dissimilar materials. Therefore, the total polarization effeciency is then defined as the net spin current to charge current ratio that enters the free layer. This value is typically between 0.1-0.5 and is highly dependent on not only the ferromagnetic materials but also the spacer layer. Additionally, the FLT term in Eq. (2.1) is typically absent in all metallic systems due to the transverse compontents of the spin polarization averaging out to zero.

A variation of the just described all-metallic spin valve is also commonly seen called the magnetic tunnel juction (MTJ). For this stack, the metallic spacer layer between the two FM layers is replaced with an ultra-thin insulating layer. This blocks the flow of the conduction electrons and thus, electron tunneling occurs. This involves only select states on the Fermi suface that have the highest probability for tunneling between the two FM layers. Since the density of states is largest for the spin up electrons, a spin current is still generated, however, the magntitude of the spin current now depends on the voltage applied across the device instead of the current. Addtionally, due to the restriction of the available spin up states that generate the spin current, large transverse components of the spin polarization are possible leading to large FLT[15].

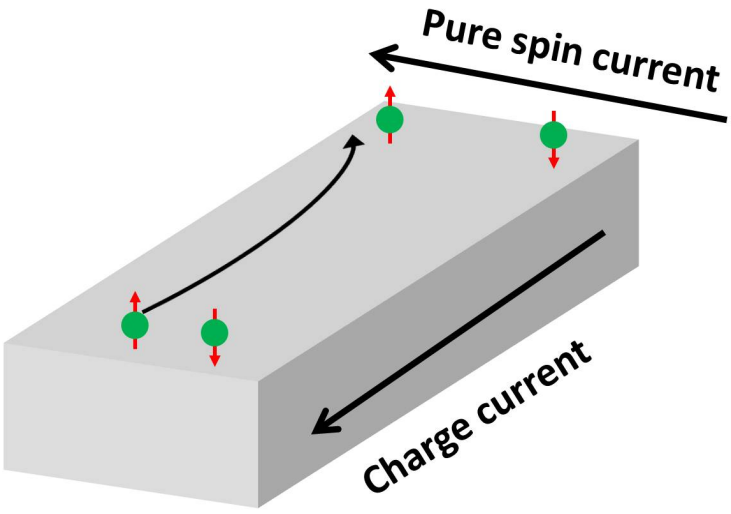

Figure 2.3: **Spin Hall effect.** Illustration of the spin Hall effect where a pure spin current is generated from electric current with the spin polarization perpendicular to both.

2.2.2 Spin Hall Effect

Recently, the spin Hall effect (SHE) has become of great interest in the spintronics community because of its ability to generate spin current without the use of a ferromagnetic reference layer[16,17]. The origin of the SHE in heavy, nonmagnetic metals is rooted in the spin orbit coupling (SOC) of the material. In the atomistic scale, SOC occurs due to the interaction of the electron's spin and the magnetic field generated by the motion of the electron about the nucleus. This causes splitting of the atomic energy levels due to the change in Zeeman energy between spin up and spin down electrons. This can then be extended to solids where the magnetic field generated from the movement of the electrons interacts with the spin of the electrons which lifts the degeneracy of the conduction bands creating a spin dependent band structure. For example, for a spin up conduction electron that rotates in a circle clockwise, the magnetic field generated by the motion will be in the same direction as the intrinsic magnetic moment of the electron thus minimizing the Zeeman energy.

Now, instead of the ferromagnet, a nonmagnetic material with strong SOC such as platinum or tantalum can be used. Due to spin dependent scattering, a pure spin current is generated transverse to the injected electric current with its polarization transverse to both as shown in Fig. 2.3. The ratio of spin current to charge current is called the spin Hall angle (SHA) and can reach as high as 33 percent[18]. The physics describing the SHE is the same as for the anomalous Hall effect in ferromagnets which is described by both intrinsic and extrinsic contributions.

The intrinsic contribution results from the Berry phase accumulated by the electrons at the Fermi surface therefore this happens inbetween scattering events.[19–21] The Berry phase is maximized when SOC splits a band such that one spin orientation lies just below the fermi surface while the other just above such that their respective phases are not cancelled out[22]. This phase acts as an addition spin dependent transverse voltage to the applied voltage which deflects spins in different directions based on their spin orientation.

The extrinsic contribution is due to two mechanism both of which occur due to scattering events. The first is skew scattering where electrons with opposite spin are deflected in opposite directions due to the difference of the SOC of the host material and the impurity[23]. The second is side jump scattering where electrons of opposite spin are shifted instead of deflected in opposite directions[24]. This results in spin accumulation transverse to the applied voltage and may have a different sign as the intrinsic contribution.

2.3 Magnetoresistance

The use of magnetoresistance (MR) is critical in magnetics since it allows the magnetic state to be observed by electrical means. Without it, magnetic memory would have never became the mainstream research direction in the semiconductor industry. Although there are many

different types of magnetoresistances, the three that appear the most are anisotropic magnetoresistance (AMR), giant magnetoresistance (GMR), and tunneling magnetoresistance (TMR).

Anisotropic magnetoresistance, discovered in 1857 by Lord Kelvin, is an effect such that the resistance of the ferromagnetic layer depends on the orientation of the magnetization and the electric field where the resistance is maximum when the two are aligned and minimum when they are transverse[25]. This magnetoresistance is described by

$$R = R_o + R_{AMR}\cos^2(\theta) \tag{2.2}$$

where R is the total resistance, R_o is the background resistance, R_{AMR} is the full AMR resistance, and θ is the angle between the electric field and the magnetization. This is due to increased s-d scattering in the direction of the magnetization from SOC. Although typical AMR ratios range from 0.5-5 percent in bulk materials and typically decreases with decreasing thickness, it only requires a single ferromagnetic layer unlike other commonly utilized magnetoresistances[26].

Giant magnetoresistance, a magnetoresistance so important that its discovers, Albert Fert and Peter Grnberg, were awarded a Nobel prize in 2007, relies on 2 magnetic layers seperated by a nonmagnetic metallic spacer layer also know as a spin valve[27,28]. The resistance of the overall structure depends on the angle between the 2 magnetizations and typically is minimum when they are parallel to each other and maximum when anti-parallel. The GMR ratio, which can be as high as 220 percent[29], depends on the band structure of all 3 layers and can best be understood as a simple 2 channel resistor problem, one for spin up and the other for spin down as illustrated in Fig. 2.4[30].

A spin up electron can more easily pass through a ferromagnetic material if it is also spin up due to the increased density of states (DOS) of the majority conduction band.

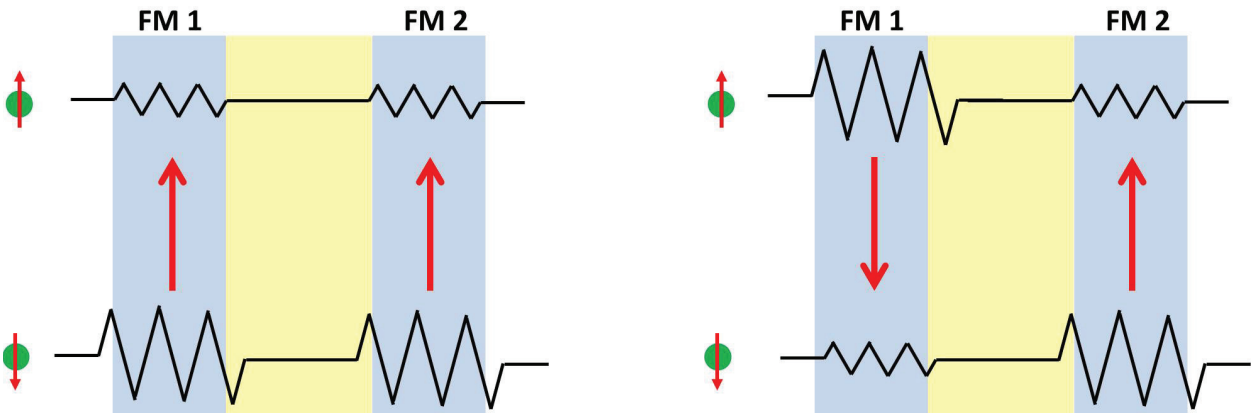

Figure 2.4: **Giant magneto-resistance.** Diagram illustrating low resistance (left) and high resistance (right) states for giant magneto-resistance of a spin valve.

On the other hand, if the ferromagnetic material is of opposite spin, there will be increased resistance as there is a lower DOS for the minority conduction band. Therefore, if both ferromagnetic layers are spin up, then the spin up electrons will easily pass through the structure while the spin down electrons are blocked. Eventually, these blocked spin down electrons will undergo a spin flip event and then be allowed to pass. This can be viewed as shorting out the circuit along the spin up channel. Now, if one layer is spin up, and the other is spin down, the electrons that can easily pass through one layer are blocked by the other. In this configuration, the circuit is no longer shorted so the resistance is higher.

Tunneling magnetoresistance is very similar to GMR however, instead of a metallic spacer layer, an insulating layer is used. Because of this, the electrons must tunnel across the insulating layer which greatly limits the available states for transport. Since tunneling is required, the non spin dependent transport is severly reduced which then allows for much higher MR ratios of up to 1144 percent[31]. Currently, TMR is used in read heads for hard drives and the building block for MRAM.

2.4 Structures

Although there are many different ways a spin torque device can take shape, there are three main categories that most belong in such that high current densities needed for spin torque manipulation are achieved. The first is the nanopillar structure as shown in Fig. 2.5(a) where there is a free layer and a spin polarizer that supplies the spin current. Both parts are patterned into a nanoscale structure ($\sim$100 nm) and an electric current is applied vertically through the structure. This leads to a spin current in the same direction due to the spin filtering by the fixed ferromagnetic layer which then manipulates the free layer. In order to read the state, GMR or TMR is used depending on the spacer layer.

The second structure is the point contact configuration as shown in Fig. 2.5(b) and is very similar to the nanopillar. Instead of patterning the free layer and the fixed layer, it is left as a thin film. In order to provide the high current densities needed for applications, a very small ($\sim$10 nm) nonmagnetic contact is fabricated ontop of the film. The current-driven magnetization dynamics of these structures differs from nanopillar devices due the interactions between the magnetization under the point contact and the rest of the film.

The third structure called the spin Hall geometry shown in Fig. 2.5(c) is unlike the other two. Instead of a fixed magnetic layer spin-polarizing electrical current, a spin Hall (SH) material such as platinum is used. Electric current is then applied longitudinally through the FM and SH layers which injects spin current vertically into the FM. The state of the magnetization can then be determined through AMR instead of GMR or TMR since there is only one magnetic layer. Even though the magnetoresistance of this structure type is smaller compared to the vertical current counterparts, it has exploded in popularity due to the ease of fabrication along with the polarization of the spin current always being normal to the flow of the electric current.

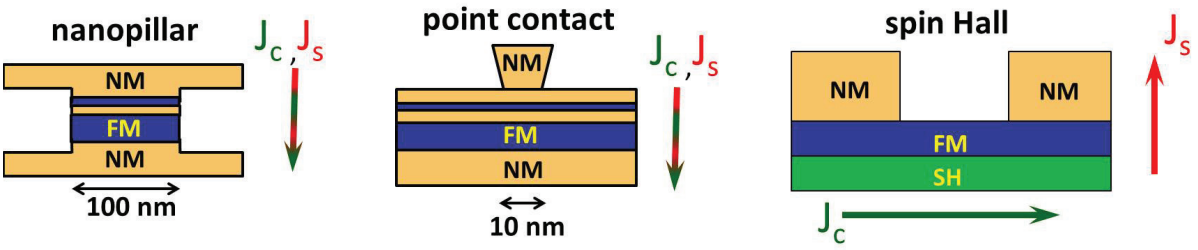

Figure 2.5: **Spintronic device structures.** Illustrations of device geometries with electric current in green and spin current in red for **(a)** nanopillar, **(b)** point contact and **(c)** spin Hall structures.

2.5 Magnetization Dynamics

How magnetization responds to magnetic fields is described by the Landau Lifshitz (LL) equation[32,33] which is

$$\frac{d\mathbf{m}}{dt} = -\gamma \left(\mathbf{m} \times \mathbf{H}_{eff} + \alpha \mathbf{m} \times \mathbf{m} \times \mathbf{H}_{eff}\right) \tag{2.3}$$

where $\mathbf{H}_{eff}$ is the effective magnetic field, α is the Gilbert damping constant, γ is the gyromagnetic ratio, and $\mathbf{m}$ is the magnetization unit vector. This equation shows that a magnetic moment in the presence of a magnetic field will experience two torques. The first is the conservative field torque that causes the moment to process about the field direction. The second is a non-conservative damping torque that aligns the moment with the magnetic field direction. This means, when a moment is not aligned with the magnetic field, the moment will oscillate as its time averaged component moves towards the field direction. As the moment approaches the field direction, the oscillations will start decaying eventually leading to a static moment in the direction of the field.

If now spin current is present, two addition torques get added to Eq. (2.3) called the Slonczewski terms[12], shown in Eq. (2.1), which leads to

$$\frac{d\mathbf{m}}{dt} = -\gamma\left(\mathbf{m}\times\mathbf{H}_{eff} + \alpha\mathbf{m}\times\mathbf{m}\times\mathbf{H}_{eff} + \beta\mathbf{m}\times\mathbf{m}\times\mathbf{p} + \beta'\mathbf{m}\times\mathbf{p}\right) \tag{2.4}$$
$$\beta = \left|\frac{\hbar}{\mu_o e}\right|\frac{J}{dM_s}\frac{P\Lambda^2}{(\Lambda^2+1)+(\Lambda^2-1)(\mathbf{m}\cdot\mathbf{p})} \qquad \beta' = C*\beta$$

where $\hbar$ is the reduced Planck constant, μ_o is the permeability of free space, e is the charge of the electron, J is the current density, d is the thickness of the magnetic material, M_s is the saturation magnetization, P is the spin current polarization, Λ is the spin torque asymmetry parameter, $\mathbf{m}$ is magnetization unit vector, $\mathbf{p}$ is the spin current polarization unit vector, and C is the ratio between the two spin torques. Again, there is a field like torque and a non conservative damping like torque resulting from the spin current where the polarization direction replaces the field direction. Generally, the field like torque is small and is often omited except for magnetic tunnel junction and some spin Hall devices. The damping like torque however, allows for a lot of different phenomena as it can modulate the effective magnetic damping in the system. If the spin torque is large enough, it can overcome the magnetic damping in the system and rotate the magnetization away from the magnetic field direction as discussed in section 2.1. Solving Eq. (2.4) is fundamental to understanding all types of magnetic phenomena ranging from switching a magnetic element to exciting GHz frequency auto-oscillations.

2.5.1 Micromagnetics

A useful tool for understanding experimental data is micromagnetics which involves breaking up a layer of magnetic material into cells and solving the LLG equation. The size of the cells is determined by the exchange length ($\lambda_{exch} = A/M_s^2$ where A is the exchange stiffness and M_s is the saturation magnetization), which is the length over which the magnetic moments

are parallel to each other and thus, can be assumed as a single spin. The most common micromagnetic software is Object Orientated Micromagnetic Framework (OOMMF) developed by NIST which is open source and CPU based[34]. Micromagnetics is heavely used for studying ferromagnetic layers because neighboring atomic spins are parallel to each other due to the exchange interaction being the dominate energy. This allows for an intermediate characterisitc length scale ($\lambda_{exch} \sim 5$ nm) to be used that has a manageable number of sites (magnetic moments) compared to atomic scale such that the LLG equation can be numerically solved. At this scale, other energies become more relavent which can rotate the magnetization of one cell away from another cell leading to spatially varying magnetization profiles.

The energy of a magnetic moment is described by Eq. (2.5) and the effective magnetic field resulting from this energy is described by Eq. (2.6).

$$E = E_{exch} + E_{demag} + E_{anis} + E_{ext} \tag{2.5}$$

$$\mathbf{H}_{eff} = -\frac{\partial E}{\partial \mathbf{m}} \tag{2.6}$$

The first term is the exchange energy which, as discussed earlier, tends to align neighboring moments in a ferromagnet. The second term is the demagnetization energy which tends to align the magnetization along the surfaces in order to reduce surface magnetic charges which results in a curvature of the magnetization. The competetion between these two energies provide the main contributions to the curl of the magnetization. The third term is the anisotropy energy which to aligns the magnetization along a perfered axis or plane. The last term is due to an external magnetic field being applied to the sample and which tends to align the moment to this field. Therefore, the process for micromagnetics is to calculate the energy for the current magnetization state using Eq. (2.5), use that to calculate the magnetic field using Eq. (2.6), which is then plugged into Eq. (2.4) and calculated for a small timestep which then produces a new magnetic state. This then is repeated until $\frac{d\mathbf{m}}{dt}$

is below a threshold such that an energy minimum is found or a certain amount of time has passed.

For some simulations, the final state can actually be a persistent dynamical state rather than a static state therefore reaching the energy minimum is not a viable ending criteria. Instead, performing a slidding fast fourier transform (FFT) of the magnetization data to frequency domain is needed. The frequency response of the magnetization over different sections of time can then be compared such that when the previous section matches the next section, the final state is found. For example, a simulation is ran for 1 μs and the magnetization data is then split up into 10 sections of 100 ns each. An FFT is performed on each section such that 10 frequency spectra of the magnetization are generated. The initial sections will contain signatures of transient dynamics that will be reduced in each following FFT until the steady state solution is found.

2.5.2 Magnetic Anisotropy

Magnetic anisotropy is responsible for the symmetry breaking of the magnetization in zero applied fields due to the magnetization having a prefered axis. The first source of magnetic anisotropy is called shape anisotropy which results from the surface magnetic charges that result from the magnetization pointing normal to a surface. These charges create a dipolar field, the demagnetization field, that cancels out the dipolar field from the local moment. Therefore, the strength of demagnetization field depends the saturation magnetization of the material and the separation distance between the magnetic charges and thus, the shape of the element, resulting in

$$\mathbf{H}_{demag} = \overleftrightarrow{\mathbf{N}} \cdot \mathbf{M} \tag{2.7}$$

where $\mathbf{H}_{demag}$ is the demagnetization field vector, $\overleftrightarrow{\mathbf{N}}$ is the demagnetization tensor that is determined by the shape of the material, and $\mathbf{M}$ is the magnetization vector. This means the demagnetization field is maximum when the magnetization points along the shortest length of the element and is strongest at the edges and weakest at the center of the element. This results in the magnetization having a prefered axis along the longest axis of the element.

The second type of magnetic anisotropy originates from SOC and can be characterized as either bulk or interfacial. The strength of bulk magnetic anisotropy is independent of the thickness of the material and is commonly magnetocrystalline, which depends on the magnetization direction relative to a crystal axis, or magnetoelastic, which arrises from strain in the film along a crystal axis. The strength of the interfacial anisotropy scales inversely with the thickness of the material is typically due to symmetry breaking at the interface[35].

Whatever the source of the anisotropy, it can be described as either, uniaxial, easy-plane, triaxial, or cubic which determines the angular dependence of the anisotropy. Uniaxial anisotropy, which is used predominately in this thesis, describes an anisotropy energy that has a single prefered axis called the easy-axis and is given to first order by

$$E_{uni} = KV\sin^2\theta \tag{2.8}$$

where K is the anisotropy constant, V is the volume of the ferromagnetic element, and θ is the angle between the magnetization and the easy-axis. Easy-plane anisotropy is similar to uniaxial anisotropy except that now there is only a high energy axis called the hard-axis. This is described by either using a negative anisotropy constant for the uniaxial equation or by combining 2 uniaxial anisotropies of equal magnitude that are orthogonal. For example, the shape anisotropy of a nanowire ferromagnetic element can be combined with an out-of-plane (OOP) interfacial anisotropy to create an easy-plane magnetic anisotropy with the

hard-axis along the width of the nanowire if balanced correctly. An example of such a case is covered in Chapter 6.

When magnetization dynamics is excited in the absence of Gilbert damping, the magnetization will precess on a conservative energy trajectory that is greatly affected by magnetic anisotropy. If an external magnetic field is applied to a sample along the y-axis without the presence of magnetic anisotropy, the trajectory will be circular about the y-axis. If now shape anisotropy is introduced such that x-axis is the longest axis of the element while z-axis is the shortest, the trajectory will now become elliptical (short side along z-axis) due to it costing more energy for the magnetization to rotate along the z-axis than the x-axis. An circular trajectory about the y-axis can then be recovered again if an uniaxial anisotropy along the z-axis is introduced to create an easy-plane anisotropy in the x-z plane.

2.5.3 Spin Waves

A spin wave is a disturbance in the magnetic order that is also a eigenmode of the magnetic system. The simpliest form is a plane wave solution such that it can be written as an oscillation of the magnetic moment about a time independent equalibrium magnetization ($\mathbf{m}_\mathrm{o}$).

$$\mathbf{m}(\mathbf{r},t) = \mathbf{m}_\mathrm{o} + \Delta\mathbf{m}(\mathbf{r})e^{i(\mathbf{k}\cdot\mathbf{r}-\omega t)} \tag{2.9}$$

The frequency of a spin wave is in the GHz regime where its wavelength is tied to its frequency through the magnetic field dependent dispersion relation of the system. The particle version of a spin wave is called a magnon which is analogous to phonons for lattice vibrations. The easiest example of a spin wave can be seen in a 1D chain of magnetic moments as shown in Fig. 2.6 with a wavelength of five moments. The equalibrium magnetization is set by the static local field, $\mathbf{H}$, and then an external force perturbs the system which excites the spin

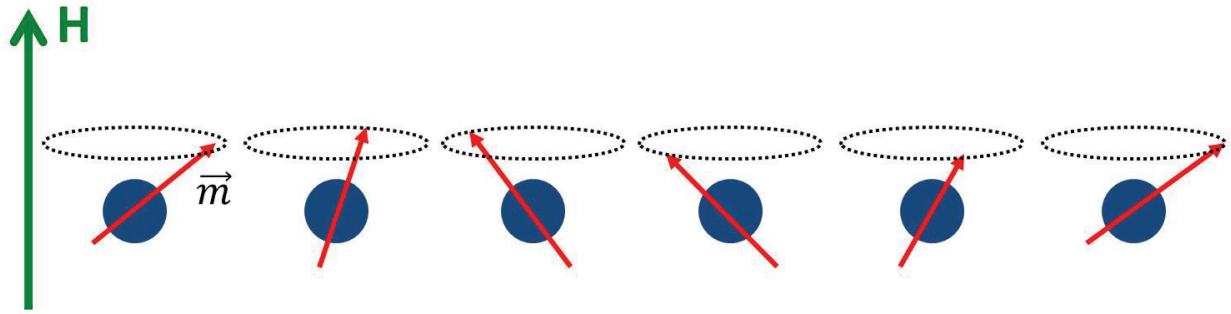

Figure 2.6: **1D spin wave.** Spin wave with a wavelength of 5 magnetic moments in a 1D chain.

wave. This excitation can be caused by various methods but the most common are thermal, which is frequency indepedent, or a GHz frequency torque, either an AC magnetic field or spin torque.

2.5.4 Spin Torque Ferromagnetic Resonance

Spin torque ferromagnetic resonance (ST-FMR) is a useful tool for measuring the spin wave eigenmodes of magnetic nanostructures. By applying an AC spin torque into a ferromagnetic layer, spin waves are resonantly excited when the injected frequency matches an eigenfrequency of the magnetic system. When a spin wave is excited, the magnetization will oscillate which generates a resistance oscillation due to the magnetoresistance present in the device at the frequency of the spin wave or its harmonics. This resistance oscillation will rectify the injected electric current generating a DC voltage[36,37]

$$V = V_{PR} + V_{PV} = I_{dc}R_{dc} + I_{ac}\delta R_{ac}\cos\phi \tag{2.10}$$

where I_{dc} (I_{ac}) is the dc (ac) current, R_{dc} (R_{ac}) is the dc (ac) resistance of the sample, and ϕ is the phase difference between the ac current and the ac resistance. Therefore, there will be either peaks or dips in the DC voltage depending on the phase difference whenever a spin

wave mode is excited. In order to see these extremas, whose linewidth is proportional to the damping of the mode, either the injected frequency or the applied magnetic field is held fixed while the other is swept.

2.5.5 Spin Torque Oscillators

Spin torque oscillators (STO) are one of the more unusual outcomes between the competition of the damping torques from an applied magnetic field and the presence of spin current. If the polarzation of the spin current has a component that is anti-parallel to the magnetic field direction as illustrated in Fig. 2.7, then the damping like torque from the spin current acts as negative damping and can cancel out the damping torque from the field. If they are of equal magnitude, then the conservative torque will cause the magnetic moment to oscillate about the equalibrium magnetization direction along a constant energy trajectory. This is an auto-oscillatory state whose frequency is determined by the eigenmode frequency of the excited state and the nonlinearities of the magnetic dynamics of the ferromagnet[38]. Typically, a self-localized bullet mode is excited whose frequency is below the spin wave spectrum, however, spin waves can be excited in certain geometries. These magnetic oscillations will then produce an AC voltage due to the oscillating resistance and the DC electric current which then can be detected with a spectrum analyzer.

The type of STO of interest for this thesis is the spin Hall oscillator (SHO) which consists of spin Hall metal, commonly Pt, and ferromagnetic bilayer, commonly Py ($Ni_{80}Fe_{20}$). By applying electrical current in the plane of the sample, as shown in Fig. 2.5, the spin torque supplied by the SHE is in the damping/anti-damping configuration when a saturating magnetic field is applied in the plane of the ferromagnetic layer perpendicular the current direction. The AMR present in the ferromagnetic layer is then used to create the microwave voltage. Due to the angular dependence of AMR, the frequency of voltage

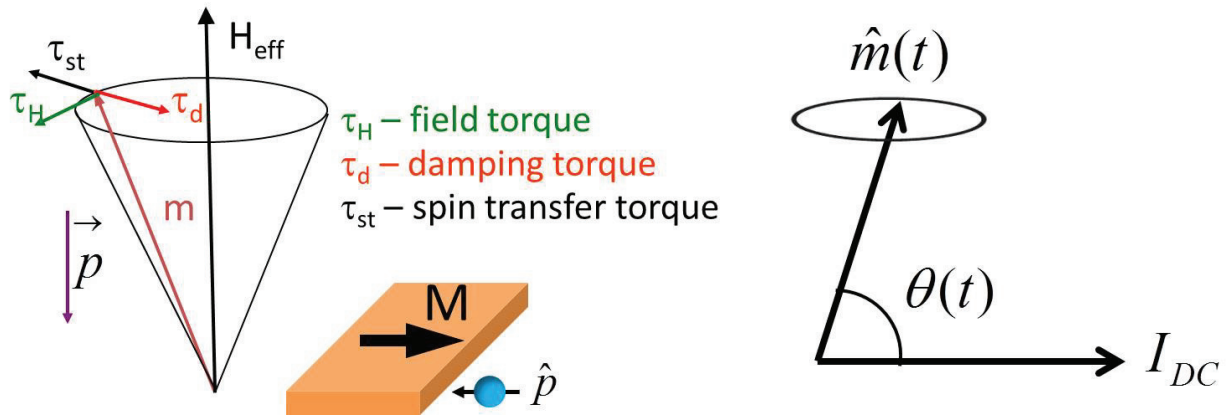

Figure 2.7: **Spin torque oscillator.** llustration of the canceling damping like torques leading resulting in self-oscillations (left) which produces an AC voltage due to the oscillating resistance (right).

generated will be twice that of the magnetization oscillations. In order to avoid this frequency doubling, the magnetic field can be tilted towards the current direction thus shifting the power into the first harmonic.

Some of the early work in SHO was done by Vladislav E. Demidov and his collaborators where they used Pt/Py bilayers and measured the magnetic oscillations using an optical technique called Brillouin light scattering (BLS). The intensity of the signal from this technique is proportional to the number of created or destructed magnons in the sample therefore, the larger the self-oscillation amplitude, the larger the signal. Their first work on SHOs involved a 2-dimensional system where a 5 μm wide Pt stripe with a 2 μm Py disk on top was used and the results of which is shown in Fig. 2.8[39]. They showed that the frequency of the oscillations redshifts with increasing current magnetitude for both polarities due to ohmic heating of the device decreasing the saturation magnetization of the Py, however, the redshift is greatly enchanced in the anti-damping current polarity, as shown in Fig. 2.8(a). Additionally, the integrated power of the signal is increased as the current is swept from postive current polarity (damping polarity) to negative current polarity (anti-damping polarity) as shown in Fig. 2.8(b). Interestly however, the intensity of the signal saturates rather than dramatically increasing with is indicative of the self-oscillatory state not being

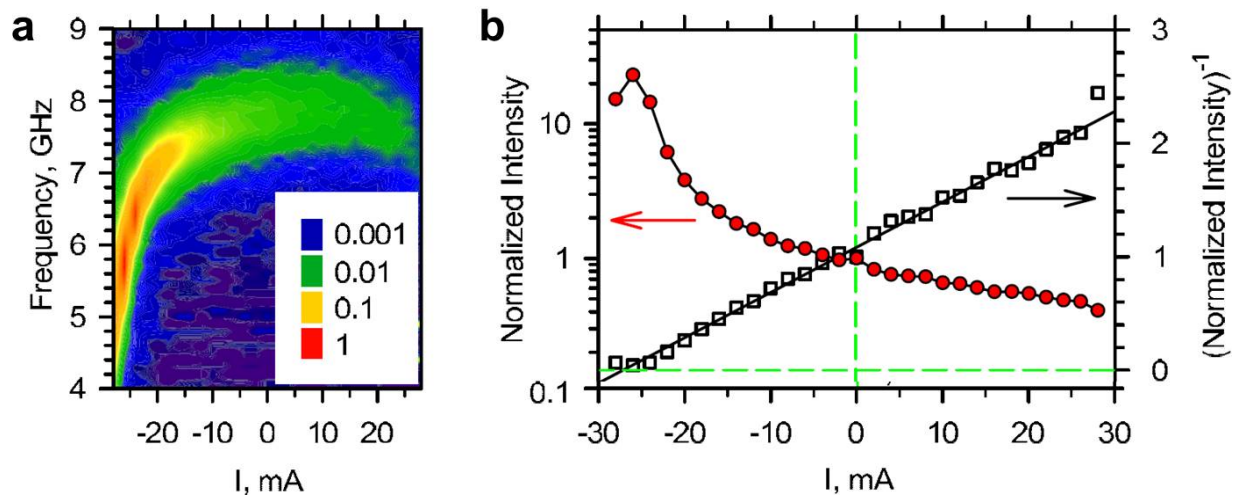

Figure 2.8: **2-dimensional oscillator.** Figure take from V. E. Demidov et al. "Control of Magnetic Fluctuations by Spin Current". Phys. Rev. Lett. 107, 107204. **(a)** Normalized BLS intensity verses frequency and current at H = 900 G applied in-plane perpendicular to the current. **(b)** Normalized integrated intensity and its inverse of the BLS signal verse current.

reached. Instead, only the thermally excited magnons are detected. This means that the spin torque reduced the saturation magnetization rather than exciting self-oscillations of the magnetization in the anti-damping configuration for a 2-dimensional system.

They next patterned electrical leads onto the Pt/Py bilayer that were separated by 100 nm thus creating a 0-dimensional system to see if self-oscillations could be excited the results of which are shown in Fig. 2.9[40]. In this dimensionality, they detected self-oscillations whose spatial profile is shown in Fig. 2.9(a). The size of the oscillatory area is similar to that of a bullet mode that is commonly found in point contact STO. The bullet mode is a self-localized soliton whose frequency lies below the ferromagnetic resonance (FMR) mode. Therefore, the frequency of the SHO along with the FMR frequency was plotted verses the magnetic field in Fig. 2.9(b). The SHO frequency is near the FMR frequency at low fields but deviates further below with increasing field. This further confirms the excited mode is in fact the bullet mode. This leaves the intermediate dimensionality, the unexplored 1-dimensional nanowire, which is studied in this thesis and described in Chapter 4.

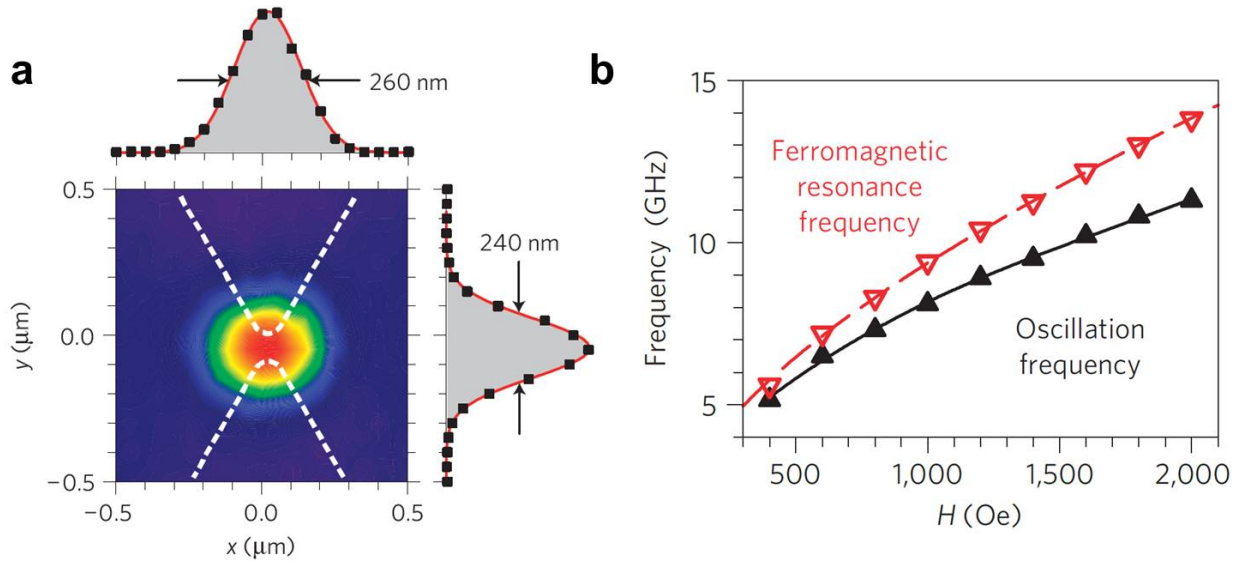

Figure 2.9: **0-dimensional oscillator.** Figure take from V. E. Demidov et al. "Magnetic nano-oscillator driven by pure spin current". Nature Materials 11, 10281031 (2012) **(a)** Spatial map of the normalized BLS intensity at $I_{dc} = 16.2$ mA and H = 900 G. The dashed lines on the map show the contours of the leads. **(b)** The SHO frequency at the onset current and the FMR frequency verses the applied magnetic field.

Bibliography

[12] J.C. Slonczewski. "Current-driven excitation of magnetic multilayers". In: *Journal of Magnetism and Magnetic Materials* 159.1-2 (1996), pp. L1–L7. DOI: doi:10.1016/0304-8853(96)00062-5. URL: http://dx.doi.org/10.1016/0304-8853(96)00062-5.

[13] L. Berger. "Emission of spin waves by a magnetic multilayer traversed by a current". In: *Phys. Rev. B* 54.13 (1996), pp. 9353–9358. DOI: http://dx.doi.org/10.1103/PhysRevB.54.9353. URL: http://dx.doi.org/10.1103/PhysRevB.54.9353.

[14] Mark Johnson and R. H. Silsbee. "Interfacial charge-spin coupling: Injection and detection of spin magnetization in metals". In: *Phys. Rev. Lett.* 55.17 (1985), pp. 1790–1793. DOI: http://dx.doi.org/10.1103/PhysRevLett.55.1790. URL: http://dx.doi.org/10.1103/PhysRevLett.55.1790.

[15] J. C. Slonczewski. "Conductance and exchange coupling of two ferromagnets separated by a tunneling barrier". In: *Phys. Rev. B* 39.10 (1989), pp. 6995–7002. DOI: http://dx.doi.org/10.1103/PhysRevB.39.6995. URL: http://dx.doi.org/10.1103/PhysRevB.39.6995.

[16] D'yakonov M.I. and Perel' V. I. "Possibility of Orienting Electron Spins with Current". In: *Sov. Phys. JETP Lett.* 13.11 (1971), p. 467. URL: http://www.jetpletters.ac.ru/ps/1587/article_24366.pdf.

[17] J. E. Hirsch. "Spin Hall Effect". In: *Phys. Rev. Lett.* 83.9 (1999), pp. 1834–1837. DOI: http://dx.doi.org/10.1103/PhysRevLett.83.1834. URL: http://dx.doi.org/10.1103/PhysRevLett.83.1834.

[18] Chi-Feng Pai et al. "Spin transfer torque devices utilizing the giant spin Hall effect of tungsten". In: *Appl. Phys. Lett.* 101.12 (2012), p. 122404. DOI: http://dx.doi.org/10.1063/1.4753947. URL: http://dx.doi.org/10.1063/1.4753947.

[19] T. Jungwirth, Qian Niu, and A. H. MacDonald. "Anomalous Hall Effect in Ferromagnetic Semiconductors". In: *Phys. Rev. Lett.* 88.20 (2002). DOI: http://dx.doi.org/10.1103/PhysRevLett.88.207208. URL: http://dx.doi.org/10.1103/PhysRevLett.88.207208.

[20] G. Y. Guo et al. "Intrinsic Spin Hall Effect in Platinum: First-Principles Calculations". In: *Phys. Rev. Lett.* 100.9 (2008). DOI: http://dx.doi.org/10.1103/PhysRevLett.100.096401. URL: http://dx.doi.org/10.1103/PhysRevLett.100.096401.

[21] T. Tanaka et al. "Intrinsic spin Hall effect and orbital Hall effect in 4 d and 5 d transition metals". In: *Phys. Rev. B* 77.16 (2008). DOI: http://dx.doi.org/10.1103/PhysRevB.77.165117. URL: http://dx.doi.org/10.1103/PhysRevB.77.165117.

[22] Axel Hoffmann. "Spin Hall Effects in Metals". In: *IEEE Trans. Magn.* 49.10 (2013), pp. 5172–5193. DOI: 10.1109/TMAG.2013.2262947. URL: http://dx.doi.org/10.1109/TMAG.2013.2262947.

[23] J. Smit. "The spontaneous hall effect in ferromagnetics {II}". In: *Physica* 24.15 (1958), pp. 39 –51. ISSN: 0031-8914. DOI: http://dx.doi.org/10.1016/S0031-8914(58)93541-9. URL: http://www.sciencedirect.com/science/article/pii/S0031891458935419.

[24] L. Berger. "Side-Jump Mechanism for the Hall Effect of Ferromagnets". In: *Phys. Rev. B* 2.11 (1970), p. 4559. URL: https://journals.aps.org/prb/pdf/10.1103/PhysRevB.2.4559.

[25] W. Thomson. "On the electro-dynamic qualities of metals: Effects of magnetization on the electric conductivity of nickel and iron". In: *Proc. Roy. Soc* 8 (1857), pp. 546–550.

[26] T. McGuire and R. Potter. "Anisotropic magnetoresistance in ferromagnetic 3d alloys". In: *IEEE Trans. Magn.* 11.4 (1975), pp. 1018–1038. DOI: 10.1109/TMAG.1975.1058782. URL: http://dx.doi.org/10.1109/TMAG.1975.1058782.

[27] M. N. Baibich et al. "Giant Magnetoresistance of (001)Fe/(001)Cr Magnetic Superlattices". In: *Phys. Rev. Lett.* 61.21 (1988), pp. 2472–2475. DOI: http://dx.doi.org/10.1103/PhysRevLett.61.2472. URL: http://dx.doi.org/10.1103/PhysRevLett.61.2472.

[28] G. Binasch et al. "Enhanced magnetoresistance in layered magnetic structures with antiferromagnetic interlayer exchange". In: *Phys. Rev. B* 39.7 (1989), pp. 4828–4830. DOI: http://dx.doi.org/10.1103/PhysRevB.39.4828. URL: http://dx.doi.org/10.1103/PhysRevB.39.4828.

[29] R. Schad et al. "Giant magnetoresistance in Fe/Cr superlattices with very thin Fe layers". In: *Appl. Phys. Lett.* 64.25 (1994), p. 3500. DOI: 10.1063/1.111253. URL: http://dx.doi.org/10.1063/1.111253.

[30] A. Fert and I. A. Campbell. "Two-Current Conduction in Nickel". In: *Phys. Rev. Lett.* 21.16 (1968), pp. 1190–1192. DOI: http://dx.doi.org/10.1103/PhysRevLett.21.1190. URL: http://dx.doi.org/10.1103/PhysRevLett.21.1190.

[31] S. Ikeda et al. "Tunnel magnetoresistance of 604% at 300 K by suppression of Ta diffusion in CoFeBMgOCoFeB pseudo-spin-valves annealed at high temperature". In: *Appl. Phys. Lett.* 93.8 (2008), p. 082508. DOI: http://dx.doi.org/10.1063/1.2976435. URL: http://dx.doi.org/10.1063/1.2976435.

[32] L. Landau and E. Lifshits. "On the theory of the dispersion of magnetic permeability in ferromagnetic bodies". In: *Physik. Zeits. Sowjetunion* 8 (1935), pp. 153–169.

[33] T.L. Gilbert. "Classics in Magnetics A Phenomenological Theory of Damping in Ferromagnetic Materials". In: *IEEE Trans. Magn.* 40.6 (2004), pp. 3443–3449. DOI: 10.1109/TMAG.2004.836740. URL: http://dx.doi.org/10.1109/TMAG.2004.836740.

[34] M.J. Donahue and D.G. Porter. *OOMMF User's Guide, Version 1.0*. Interagency Report NISTIR 6376. Gaithersburg, MD: National Institute of Standards and Technology, 1999.

[35] Gerardus Henricus Otto Daalderop. *Magnetic anisotropy from first principles*. TU Delft, Delft University of Technology, 1991.

[36] A. A. Tulapurkar et al. "Spin-torque diode effect in magnetic tunnel junctions". In: *Nature* 438.7066 (2005), pp. 339–342. DOI: 10.1038/nature04207. URL: http://dx.doi.org/10.1038/nature04207.

[37] J. C. Sankey et al. "Spin-Transfer-Driven Ferromagnetic Resonance of Individual Nanomagnets". In: *Phys. Rev. Lett.* 96.22 (2006). DOI: http://dx.doi.org/10.1103/PhysRevLett.96.227601. URL: http://dx.doi.org/10.1103/PhysRevLett.96.227601.

[38] S. I. Kiselev et al. "Microwave oscillations of a nanomagnet driven by a spin-polarized current". In: *Nature* 425.6956 (2003), pp. 380–383. DOI: 10.1038/nature01967. URL: http://dx.doi.org/10.1038/nature01967.

[39] V. E. Demidov et al. "Control of Magnetic Fluctuations by Spin Current". In: *Phys. Rev. Lett.* 107.10 (2011). DOI: http://dx.doi.org/10.1103/PhysRevLett.107.107204. URL: http://dx.doi.org/10.1103/PhysRevLett.107.107204.

[40] Vladislav E. Demidov et al. "Magnetic nano-oscillator driven by pure spin current". In: *Nature Materials* (2012). DOI: 10.1038/nmat3459. URL: http://dx.doi.org/10.1038/nmat3459.

Chapter 3

Experimental Methods, Simulations and Fabrication

3.1 Platinum Growth

A popular material to use in spintronics is platinum (Pt) due to its ability to generate pure spin current from an electrical current. This is made possible because of its large spin orbit coupling which results in a spin Hall angle of $\sim 7\%$[41]. Therefore, it is important to be able to grow Pt with different textures to serve as not only the spin current source, but also the seed layer for later layers. An ideal substrate for Pt growth and spintronics use must be electrically insulating but yet thermally conductive while also lattice matching Pt's 3.91 Å lattice constant and fcc crystal structure. This means that a textured MgO substate, fcc and a lattice constant of 4.12 Å, can be used to grow similarly textured Pt. Additionally, sapphire(0001), hcp and a lattice constant of 4.78 and 12.99 Å, can also be used to grow Pt(111) due to the ABC packing of hcp along (0001) is identical to the AB packing of fcc

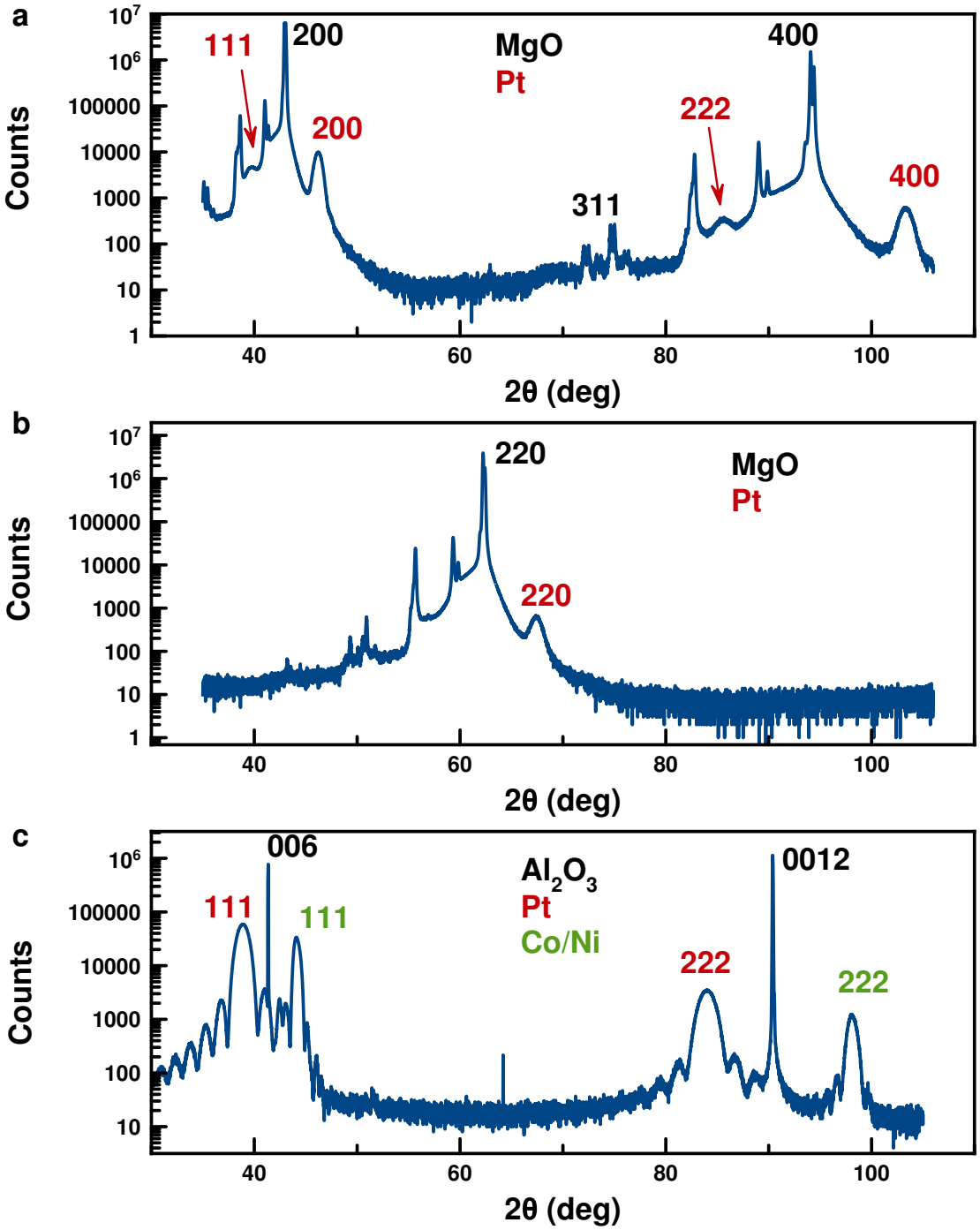

Figure 3.1: **Textured Pt growth.** Out-of-plane texture of Pt(5) grown by magnetron sputtering at 585^o C and annealed for 1 hour at same temperature on **(a)** MgO(100), **(b)** MgO(110) and **(c)** Sapphire(0001). A Ni/Co superlattice was also grown on top of the Pt for **(c)** at room temperature. The additional peaks next to the substrate peaks in **(a)** and **(b)** are due to the K_β and K_ω lines from the Cu source which is absent in **(c)** due to the addition of Ge(220) filter at the detector.

along (111) where C is 60^o rotated about A resulting in a lattice mismatch of $\sim 0.9\%$[42]. In order to grow the films by magnetron sputtering, follow the steps below.

1. Clean the chosen substrate by sonicating in acetone and then IPA for 10 mins with the polished side up.

2. Transfer the sample to the sputtering system and clap the substate in the center of the stage using 2 clips. Do not over tighten the clips as this can introduce strain in the film.

3. Heat the sample up to 585^o C over the course of 45 mins in the sputtering system.

4. Argon plasma clean the sample at 585^o C for 20 seconds at 40% power. Do not do extended cleaning as argon plasma produces long range surface corrugation[42].

5. Deposit 3-5 nm of Pt using a side gun at 1 $\mathring{A}$/s (15% power) while maintaining a temperature of 585^o C. The likelyhood of a continuous film increases with increasing Pt thickness.

6. Anneal the sample at 585^o for 1 hour.

7. Let cool for 4 hours inside the chamber.

8. If additional materials are needed, argon plasma clean at the wanted temperature for 1 min at 40% power (removing about 1 nm of material) and deposit an additional 2 nm of Pt in order to create a good interface for the next layers. Then grow the wanted materials.

9. Remove the sample from the sputtering system.

The results of the using this growth recipe is shown in Fig. 3.1 where the out-of-plane (OOP) texture is shown. For the (100) and (110) Pt growth, the substrate used was

MgO and the $K_{\alpha 2}$, $K_{\beta 1,2}$, and K_{ω} lines were not filtered out for the x-ray diffraction patterns while (111) Pt was grown on Al_2O_3(0001) with a Ge(220) filter that only allows the K_{α} line. The OOP texture for Pt(5) grown on MgO(100) is shown in Fig. 3.1(a) where the (200) and (400) peaks of the MgO substrate and Pt are clearly seen. However, the (111) and (222) peaks of Pt is also seen which indicates additional tuning is needed. One possible path is an improved substate as the (311) peak of MgO is seen which indicates poor phase purity of the substate. Another path is to change to strontium titanate as this has been shown to produce higher quality films. When Pt(5) is grown on MgO(110), shown in Fig. 3.1(b), only the (220) peak is seen for both MgO and Pt resulting in good films. Lastly, the OOP texture of Pt(7)/[Co(0.5)/Ni(1)]$_1$0/Al(2) on sapphire(0001) is shown in Fig. 3.1(c) where only the (006) and (0012) peaks of sapphire and the (111) and (222) peaks of Pt, Co, and Ni are seen. Additionally, Pendelösung fringes are seen which indicates a very smooth film[43]. Similar results for the (111) Pt growth can be achieved if the sapphire substrate is replaced with MgO(111).

3.2 Fabrication recipes

This section covers the fabrication recipes for creating 2-port nanowire samples that can be used for spin Hall oscillators and other spintronic devices. The pattern file outlines used for creating the leads is shown in Fig. 3.2(a) and (b) while the nanowire is shown in (c). These patterns can be adjusted to use for any width of nanowire or active region size within reason, however, if the wire width becomes too large, make sure to increase the width of the leads near the wire. If more ports are needed, the fabrication recipes that follow can be still used with the modified lead design.

Photolithography can also be done on the wafer to create large leads and identifer numbers for each sample as shown in Fig. 3.3. These leads need to have a hard mask

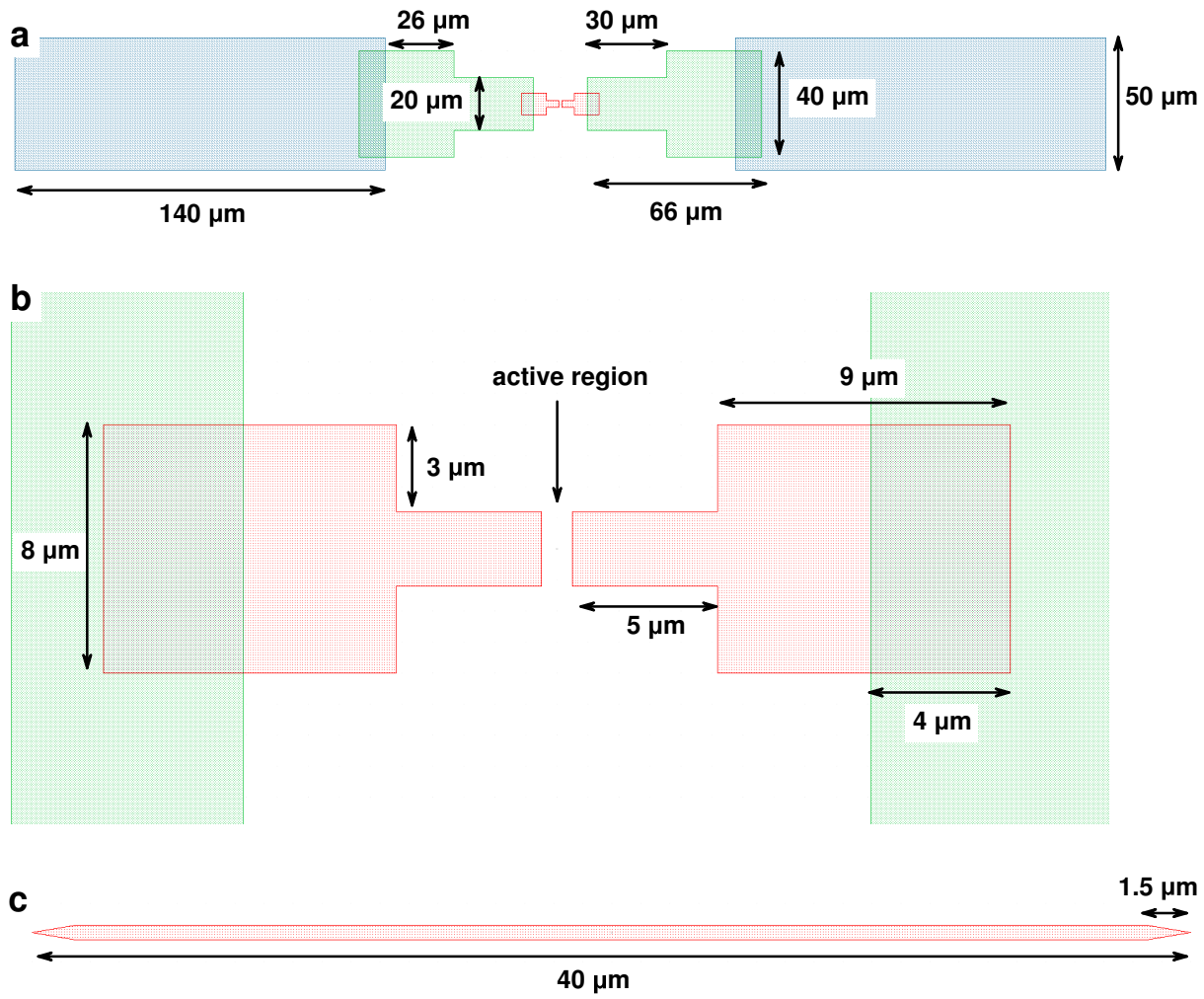

Figure 3.2: **EBL pattern outlines.** **(a)** 2-port lead design used for spin Hall oscillators where the 3 different colors represent a different layer allowing for variable beam current and dosage values and the active region can be adjusted by shifting all of the layers left and right. **(b)** Zoom in of the lead design. **(c)** Nanowire design where the width can be adjusted according to wanted wire dimensions and tapering at end serves as spin wave absorber.

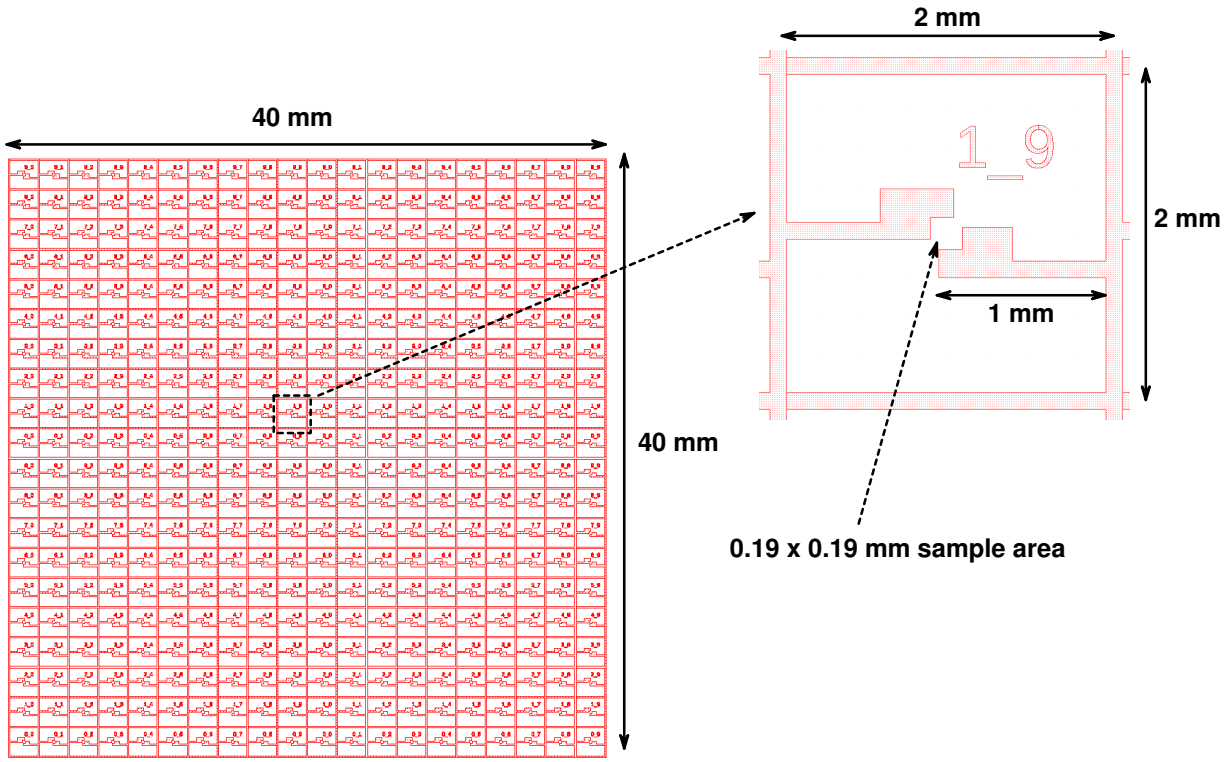

Figure 3.3: **Photolithography lead outline.** Outline for the photolithography leads that should be done on a 2" wafer. Each sample is labeled with a column and row number ranging from 0-9 and is repeated 4 times over the full range of the pattern. A zoom in of a single sample area is shown on the right. A square area is left open between the two leads which is where the sample can be created. EBL leads connect the sample to the photolithography leads.

that can survive the etching process therefore adding a hard mask to the leads that will be etched away completely after the first etching step is needed. An example lead stack would be Ti(10)/Au(50)/Ta(3) which can be done with a combination of e-beam evaporation and sputter deposition. Since these leads are done beforehand, the thin film below will be shielded therefore magnetic material will exist below. This will not impact performance of the device though because the current density in the leads is small and this magnetic material will be far away from the device. Additionally, both ports for all of the samples are connected to one another in order to prevent static discharge during fabrication and shipping. Once a sample needs to be measured, the stripes connecting each device to each other needs to be carefully scratched away typically by a diamond scribe.

3.2.1 Mill defined Pt/Py nanowire

This section contains the fabrication recipe, shown in Fig. 3.4, for creating Pt/Py 2-port nanowire samples, however, the Py layer can easily be replaced with any other ferromagnetic layer and only result in minor changes to the etching time and hard mask thickness. Additionally, this fabrication allows for optical access to the ferromagnetic layer. If optical access is not needed, the final product can be coated in HSQ and vacuum dried to protect the sample from aging. Additionally, if the nanowire width needs to be thinner than the capabilities of PMMA, HSQ can then be used.

1. An Al_2O_3/Pt(6)/Py(5)/Al(2)Ox chip is needed for the fabrication of the device. If no wafers are left, make a wafer following Sec 3.1 using 5 nm for the intial seed layer and then depositing Pt(2)/Py(5)/Al(2).

2. Dice off a chip following Sec. 3.3.3 resulting in Fig. 3.4(a).

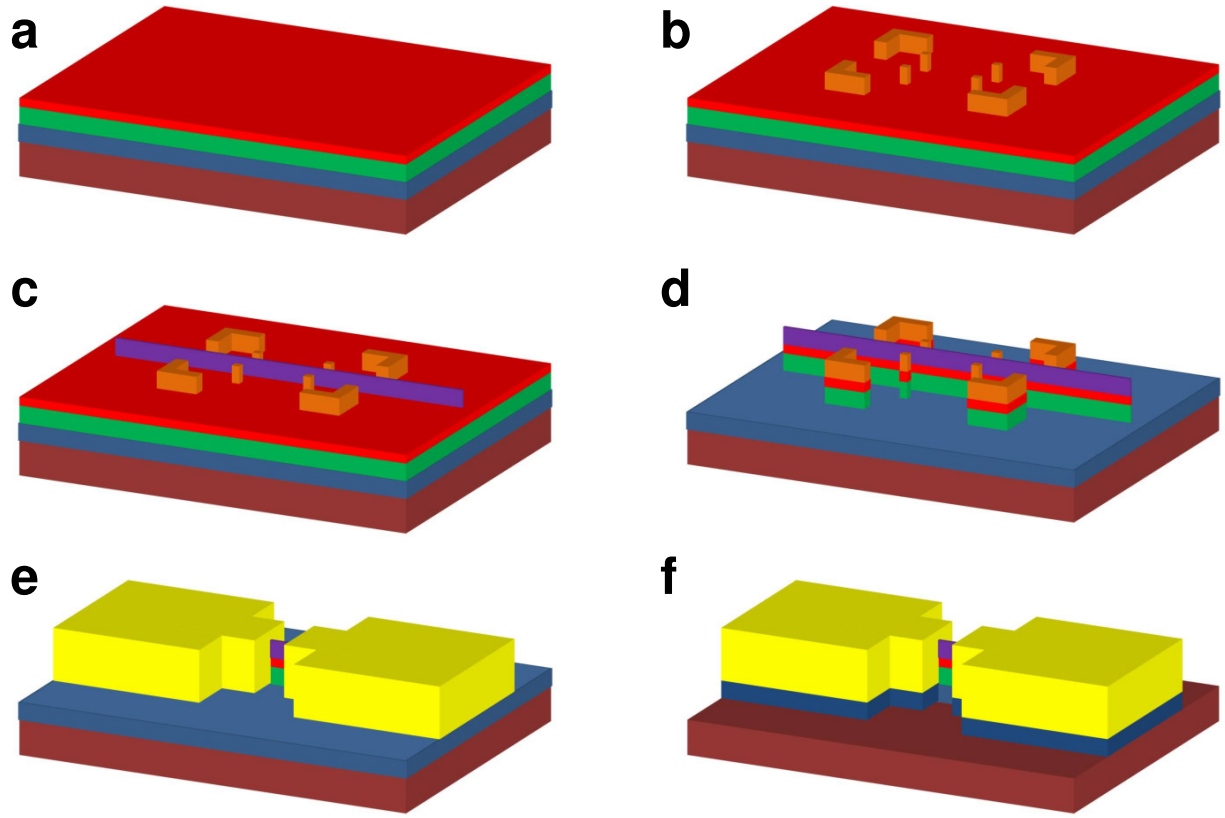

Figure 3.4: **Mill defined sample with Pt on bottom.** Fabrication outline for 2-port, Pt/Py nanowire samples that are ion mill defined with Pt on a sapphire(0001) substrate. **(a)** Starting stack consisting of Pt(6)/Py(5)/Al(2) followed by **(b)** alignment mark definition using MMA/PMMA and e-beam evaporation of Ti/Au. **(c)** Nanowire definition is then done using PMMA and e-beam evaporation of Al_2O_3 followed by textbf(d) ion milling down to Pt. **(e)** Lead definition follows using MMA/PMMA and e-beam evaporation of Ti/Au and is finished up by **(f)** ion milling clean up etch removing rest of Pt.

3. Following Sec. 3.3.1, spin coat MMA/PMMA and write the 3 global and 25 sample alignments using EBL with a dosage of 350 $\mu C/cm^2$ and a beam current of 50 pA following Sec. 3.3.3.

4. Develop the sample following Sec. 3.3.1 and then oxygen plasma cleaning the sample and e-beam evaporate Ti(10)/Au(30). If the e-beam evaporator is broken or busy, sputtering Ta(30)/Pt(5) works also. Lift off the material resulting in Fig. 3.4(b).

5. Spin coat 100 nm of PMMA by following Sec. 3.3.1 and write the nanowire devices, shown in Fig. 3.2(c), using EBL following Sec. 3.3.3 using a beam current of 13, "Center-to-Center" and "Line Spacing" distance of 1.4 nm, Magnification of 1500, and an area dosage fitting for the pattern using the dosage chart in Sec. 3.3. For really small devices, use HSQ instead of PMMA and follow Sec. 3.3.2.

6. Following Sec. 3.3.1, develop the sample and then oxygen plasma clean the sample and e-beam evaporate Al_2O_3(10). Lift-off the material resulting in Fig. 3.4(c). If HSQ was used, just develop the sample following Sec. 3.3.2.

7. Image a representative device for each device type using SEM. Do not image every device as this can damage the devices.

8. Etch the sample down to 1 nm into the Pt using ion milling following Sec. 3.4 with a beam voltage of 400 V, beam current of 30 mA, accelerating voltage of 80 V, emission current of 35 mA, stage angle of 45^o, active etch time of 95 seconds, and cycle time of 15/15 seconds. This results in Fig. 3.4(d).

9. Again image a representative device for each device type using SEM.

10. Following Sec. 3.3.1, spin coat MMA/PMMA and write leads to the device following Sec. 3.3.3 and using the pattern shown in Fig. 3.2(a). For the closest layer (red), use a beam current of 50 pA, "Center-to-Center" and "Line Spacing" distance of 10 nm,

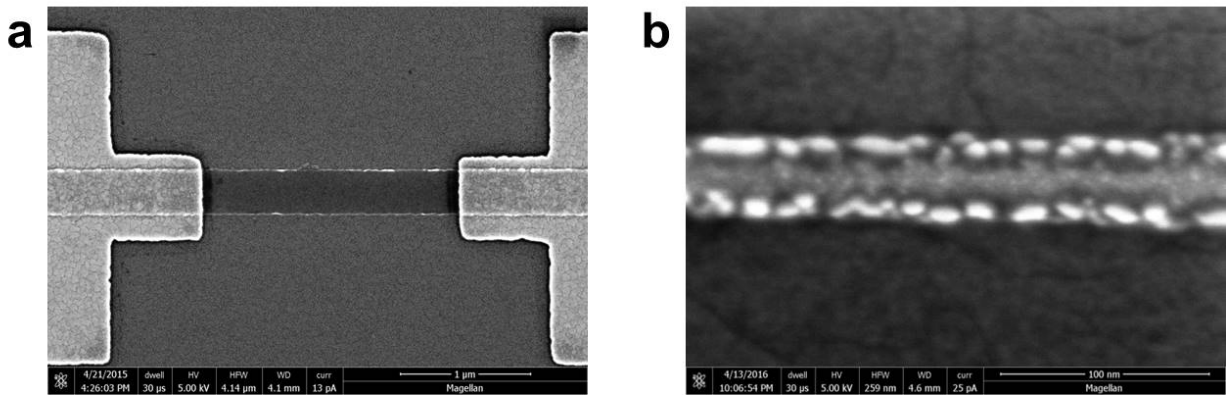

Figure 3.5: **SEM images of mill defined samples. (a)** SEM image of 340 nm wide Pt/Py nanowire using mill defined recipe and PMMA e-beam resist for nanowire definition. **(b)** SEM image of 51 nm wide Pt/Co/Ni nanowire using mill defined recipe and HSQ e-beam resist.

magnification of 850, and dosage of 325 $\mu m/cm^2$. For the next layer (green), use 400 pA, 30 nm, 850, and 300 $\mu m/cm^2$. For the largest layer (blue), use 6400 pA, 43 nm, 300, and 275 $\mu m/cm^2$.

11. Following Sec. 3.3.1, develop the sample and then oxygen plasma clean the sample and e-beam evaporate Ti(10)/Au(50). Lift-off the material resulting in Fig. 3.4(e). If e-beam evaporation isn't possible, the lead material can be sputtered however care should be taken to not include spin Hall metals.

12. Image a representative device for each device type using SEM.

13. Etch the remaining Pt down into the substrate using ion milling following Sec. 3.4 with a beam voltage of 400 V, beam current of 30 mA, accelerating voltage of 80 V, emission current of 35 mA, stage angle of 45^o, active etch time of 35 seconds, and cycle time of 15/15 seconds. This results in Fig. 3.4(f).

14. The samples are now ready to be diced into 2×2 mm chips and placed into a gel pack. If no identifier marks are present for each sample, be careful not to mix up devices by only dicing a single chip at a time and place it into the gel pack.

3.2.2 Lift-off defined Pt/Py nanowire

This section contains the fabrication recipe, shown in Fig. 3.6, for creating Pt/Py 2-port nanowire samples, however, the Py layer can easily be replaced with any other ferromagnetic layer and only result in minor changes. Additionally, this fabrication allows for optical access to the ferromagnetic layer. If optical access is not needed, the final product can be coated in HSQ and vacuum dried to protect the sample from aging. The downside of this fabrication recipe is that magnetic sidewalls are left behind which can influence the operation of the device.

1. An Al_2O_3/Pt(5) chip is needed for the fabrication of the device. If no wafers are left, make a wafer following Sec 3.1.

2. Dice off a chip following Sec. 3.3.3 resulting in Fig. 3.6(a).

3. Following Sec. 3.3.1, spin coat MMA/PMMA and write the 3 global and 25 sample alignments using EBL with a dosage of 350 $\mu C/cm^2$ and a beam current of 50 pA following Sec. 3.3.3.

4. Develop the sample following Sec. 3.3.1 and then oxygen plasma cleaning the sample and e-beam evaporate Ti(10)/Au(30)/Ti(5). If the e-beam evaporator is broken or busy, sputtering Ta(30) works also. Lift off the material resulting in Fig. 3.6(b).

5. Spin coat 100 nm of PMMA by following Sec. 3.3.1 and write the nanowire devices, shown in Fig. 3.2(c), using EBL following Sec. 3.3.3 using a beam current of 13, "Center-to-Center" and "Line Spacing" distance of 1.4 nm, Magnification of 1500, and an area dosage fitting for the pattern using the dosage chart in Sec. 3.3.

6. Following Sec. 3.3.1, develop the sample and then argon plasma clean the sample at 40 % power for 1 minute in the sputter system followed by sputtering Pt(2)/Py(5)/Al(2). Additional protection is needed from etching therefore either e-beam evaporate Al_2O_3(6)

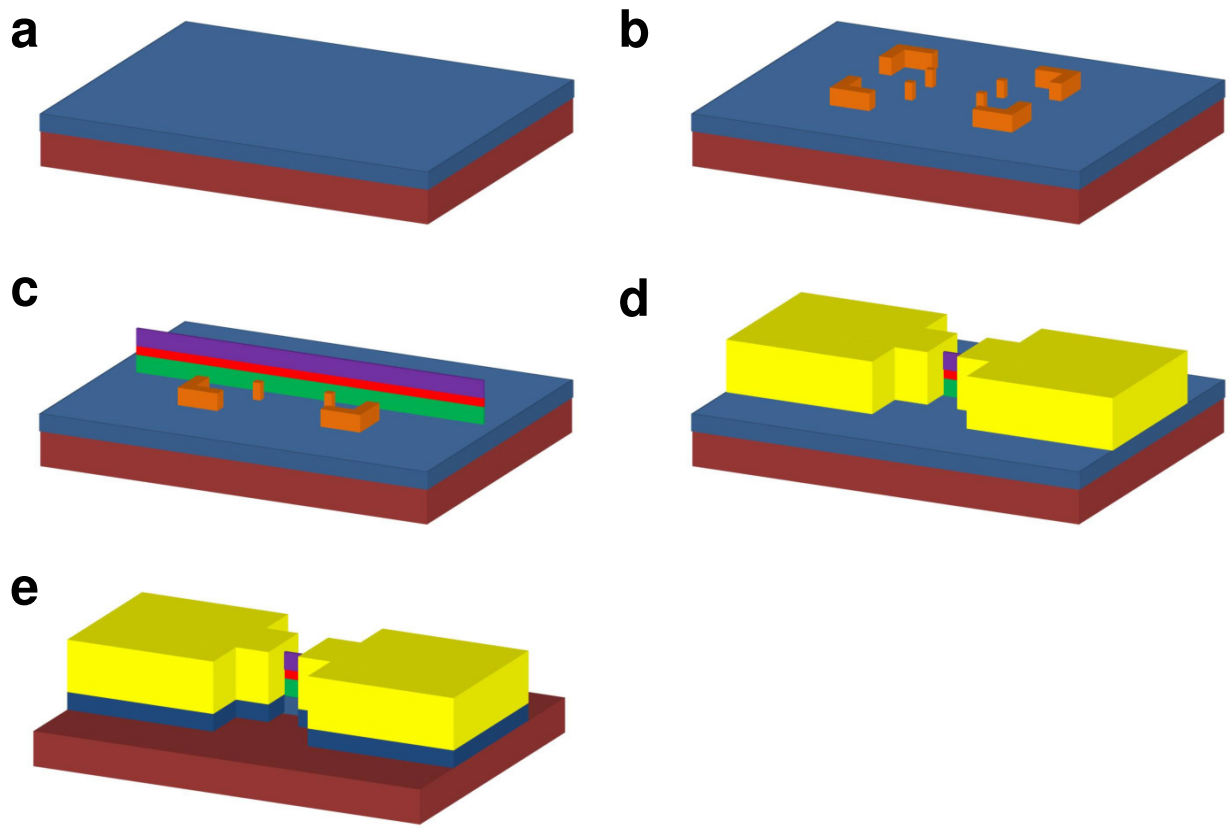

Figure 3.6: **Lift-off defined sample.** Fabrication outline for 2-port, Pt/Py nanowire samples that are lift-off defined with Pt on a sapphire(0001) substrate. **(a)** Starting stack consisting of Pt(5) followed by **(b)** alignment mark definition using MMA/PMMA and e-beam evaporation of Ti/Au. **(c)** Nanowire definition is then done using PMMA and sputter deposition of Pt(2)/Py(5)/Al(2). **(d)** Lead definition follows using MMA/PMMA and e-beam evaporation of Ti/Au and is finished up by **(e)** ion milling clean up etch removing rest of Pt.

ontop of the sputtered layers or expose the sample to air and sputter Al(2) 3 times thus creating ∼6 nm of AlOx. Lift-off the material resulting in Fig. 3.6(c).

7. Image a representative device for each device type using SEM. Do not image every device as this can damage the devices.

8. Following Sec. 3.3.1, spin coat MMA/PMMA and write leads to the device following Sec. 3.3.3 and using the pattern shown in Fig. 3.2(a). For the closest layer (red), use a beam current of 50 pA, "Center-to-Center" and "Line Spacing" distance of 10 nm, magnification of 850, and dosage of 325 $\mu m/cm^2$. For the next layer (green), use 400 pA, 30 nm, 850, and 300 $\mu m/cm^2$. For the largest layer (blue), use 6400 pA, 43 nm, 300, and 275 $\mu m/cm^2$.

9. Following Sec. 3.3.1, develop the sample and then oxygen plasma clean the sample and e-beam evaporate Ti(10)/Au(50). Lift-off the material resulting in Fig. 3.6(d). If e-beam evaporation isn't possible, the lead material can be sputtered however care should be taken to not include spin Hall metals.

10. Image a representative device for each device type using SEM.

11. Etch the exposed Pt down into the substrate using ion milling following Sec. 3.4 with a beam voltage of 400 V, beam current of 30 mA, accelerating voltage of 80 V, emission current of 35 mA, stage angle of 45^o, active etch time of 35 seconds, and cycle time of 15/15 seconds. This results in Fig. 3.6(e).

12. The samples are now ready to be diced into 2 × 2 mm chips and placed into a gel pack. If no identifier marks are present for each sample, be careful not to mix up devices by only dicing a single chip at a time and place it into the gel pack.

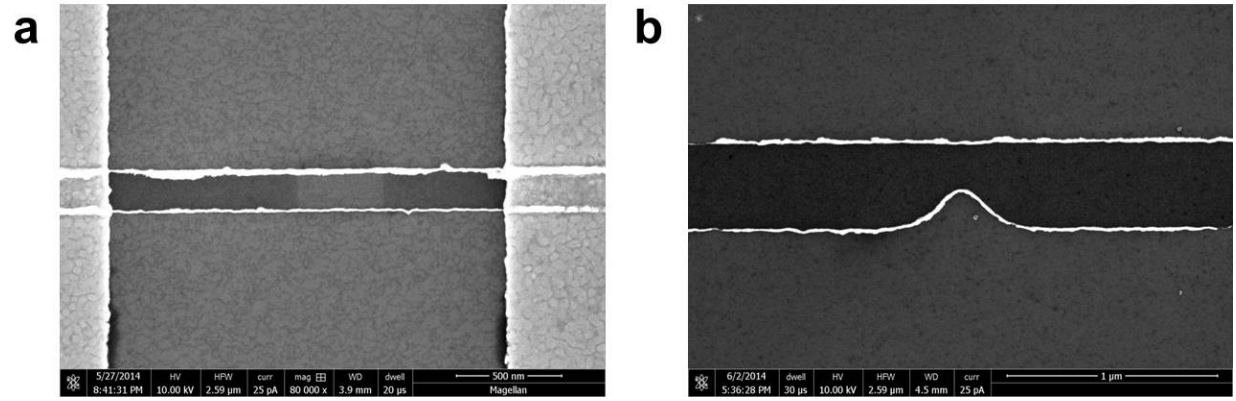

Figure 3.7: **SEM images of lift-off defined samples. (a)** SEM image of ≈200 nm wide Pt/Py nanowire using the lift-off defined recipe. **(b)** SEM image of ≈400 nm wide Pt/Py nanowire with ≈200 nm constriction using the lift-off defined recipe.

3.3 E-beam lithography

E-beam lithography is a commonly used tool for defining nanostructures. When a e-beam is dragged along a sample with e-beam resist on it, the spots where the e-beam touched will become exposed. If the e-beam resist is a positve resist, such as PMMA, then when the sample is developed, the exposed area will wash away. Material can then be deposited onto the sample and when the rest of the resist is washed away, the material will only remain where the resist was exposed. Alternatively, if the e-beam resist is a negative resist, such as HSQ, then when the sample is developed, the exposed area will remain while the rest of the resist will wash away. The following provides instructions on how the perform this procedure using the NPGS program on the Magellan SEM that is apart of LEXI.

Pattern	MMA/PMMA_MIBK(1):IPA(3)	HSQ(4%)_NaOH	HSQ(4%)_MF-319
150 μm box	275 $\mu C/cm^2$	2300 $\mu C/cm^2$	2000 $\mu C/cm^2$
alignment marks	350 $\mu C/cm^2$		
300x150 nm			1100 $\mu C/cm^2$
75x25 nm		7000 $\mu C/cm^2$	
30 nm nanowire	not possible	0.45 nC/cm	
150 nm nanowire	420 $\mu C/cm^2$		0.04 nC/cm
300 nm nanowire	380 $\mu C/cm^2$		0.03 nC/cm
2000 nm nanowire	360 $\mu C/cm^2$		0.02 nC/cm

Table 3.1: Approximate dosage values for various patterns, resists, and developer combinations. Dosage testing should be done for all patterns prior to making official samples due to variance in e-beam and resist conditions.

3.3.1 MMA/PMMA resist

General Notes

1. MMA and PMMA are both positive resists that can be removed with acetone but remains with IPA.

2. The same dosage will result in a larger MMA device than PMMA.

3. MMA and PMMA are UV sensitive therefore keep samples in the dark if the resist has not been developed yet.

4. If the sample charges too much for writing, sputter 2 nm of Pt at 30% power on top of the resist.

5. If only a single layer of resist is wanted, use PMMA by itself.

6. Multiple layers of either resist can be spun coat to increase the thickness with baking inbetween each coating.

7. Both resists are stable over long periods of time.

8. Don't develop the resist until right before the metal deposition in order to prevent dust particles from ruining the pattern.

9. Common e-beam evaporated hard masks are Al_2O_3, Cr, and Ti while a sputtered one is Ta.

10. To aid in lift-off, soak the sample in 70^o C acetone bath.

11. If the resist gets too hot, the resist can bake onto the sample making it tough to lift-off.

Spin Coating Instructions

1. Clean sample in developer being used and rinse with IPA.

2. Pre-bake the sample on the hotplate at 180^o C for 1 min.

3. Place the sample in the spin coater, secure it in place with vacuum, and select program 6 (4000 RPM for 45 seconds) to get $\sim$ 70 nm each layer or program 8 (1800 RPM for 45 seconds) to get $\sim$ 100 nm each layer.

4. Clean a plastic disposable dropper with nitrogen gas.

5. Carefully open the MMA bottle, press down on the dropper head, insert the tip into the MMA, draw a couple drops worth without spraying air into it, spray the resist onto the sample through the opening of the spin coater lid, press start, and close the MMA bottle.

6. Throw away the dropper.

7. Immediately after the spin coater stops, bake the sample at 180^o C for 1 minutes 30 seconds.

8. Repeat steps 3-7 but with PMMA this time.

Developing

1. Put on latex gloves, grab a small beaker (sample) and a medium beaker (waste), and clean the carbon fiber tweezers.

2. If the MIBK:IPA developer is empty, rinse out the used bottle with IPA and dry with nitrogen gas. Mix 3 parts IPA and 1 part MIBK and label the bottle with the date, your name, and the contents.

3. Clean the small beaker with acetone and IPA and then dry with nitrogen gas. Rinse with MIBK:IPA developer solution and then fill up 1/3 the way with it.

4. Place the sample in the developer for 70 seconds and gently swirl throughout.

5. Rinse the sample with IPA for 45 seconds to stop development. Dry with nitrogen gas and place the sample in it's box.

6. Inspect the patterns under the optical microscope to see if the writing process was successful. If the patterns are below 500 nm, they might not be easily visable.

7. Dispose of the used developer.

Depositing Materials and Liftoff

1. If the material is being sputtered, argon plasma clean the sample at 40% power for 60 seconds right right before deposting. If the material is being e-beam evaporated, oxygen plasma clean the sample for 1 minute and 30 seconds using the Harrick plasma cleaner in BION right before the evaporation.

2. To lift of the material, put on latex gloves, grab a small beaker (sample) and a medium beaker (waste), and clean the carbon fiber tweezers.

3. Clean the small beaker with acetone and IPA and then fill up 2/3 full with acetone.

4. Place the sample in the beaker and gently swirl until the material starts to crinkle.

5. Sonicate for 20 seconds. If material is still left behind, gently swirl and let soak for longer and then try sonicating again.

6. While spraying IPA where the sample will exit the acetone, remove the sample from the acetone beaker and bring over to the waste beaker. Continue spraying IPA for 45 seconds. Dry with nitrogen gas.

7. Inspect the patterns under the optical microscope to see if the writing process was successful. If the patterns are below 500 nm, they might not be easily visable. If the liftoff needs improvement, continue soaking the sample in fresh acetone and sonicate more.

8. Dispose of the acetone and IPA.

3.3.2 HSQ resist

General Notes

1. HSQ is a negaive e-beam resist and the only way to remove it after development is by etching. It can be removed immediately after spin coating with acetone.

2. Keep the resist bottle in the refrigerator at 10^oC whenever not in use.

3. If resist needs to be transfered to another bottle, only use HDPE plastic container. Otherwise, keep in original bottle if possible.

4. Solvent for HSQ evaporates rapidly therefore limit air exposure before spin coating.

5. After spin coating, resists only lasts for $\sim$ 2 hours before degrading.

6. Two different developers are available, salty NaOH (finer resolution and stronger structures) and MF319 (general use).

7. NaOH developer stripes AlOx capping layers therefore use MF319.

8. 4% HSQ is the optimal concentration that will result in $\sim$ 80 nm of resist.

9. The etching rate of HSQ developed by salty NaOH is similar to SiOx while developed by MF319 is slightly faster.

Spin Coating Instructions

1. Clean sample in developer being used and rinse with HPLC water.

2. Pre-bake the sample on the hotplate at 105^{o}C for 1 min.

3. Place the sample in the spin coater, secure it in place with vacuum, and select program 6 (4000 RPM for 45 seconds).

4. Clean a plastic disposable dropper with nitrogen gas.

5. Without setting the dropper down or letting the tip touch anything, retrieve the HSQ bottle from the fridge and bring it to the spin coater.

6. Quickly but carefully open the HSQ bottle, press down on the dropper head, insert the tip into the HSQ, draw a couple drops worth without spraying air into it, spray the resist onto the sample through the opening of the spin coater lid, press start, and close the HSQ bottle.

7. Throw away the dropper.

8. Immediately after the spin coater stops, bake the sample at 105^{o}C for 3 minutes 20 seconds.

9. After writing, post bake the sample at 80^{o}C for 1 minute.

Salty NaOH developing

1. Put on latex gloves, grab a small HDPE plastic beaker (sample) and a medium HDPE plastic beaker (waste), and clean the carbon fiber tweezers.

2. If no developer is left, mix 22.5 mL of 5M NaOH, 61.5 mL of 5M NaCl, and 366 mL of HPLC grade water in a 500 mL HDPE plastic container using a plastic graduated cylinder.

3. Clean the small HDPE plastic beaker with acetone and IPA. Rinse with HPLC grade water and then dry with nitrogen gas. Rinse with the developer and then fill up half way with it.

4. Place the sample in the developer for 2 minutes and gently swirl throughout.

5. Rinse the sample with HPLC grade water for 45 seconds to stop development. Dry with nitrogen gas and place the sample in it's box.

6. Inspect the patterns under the optical microscope to see if the writing process was successful. If the patterns are below 500 nm, they might not be easily visable.

7. Dispose of the used developer.

MF-319 developing

1. Put on latex gloves, grab a small HDPE plastic beaker (sample) and a medium HDPE plastic beaker (waste), and clean the carbon fiber tweezers.

2. Clean the small HDPE plastic beaker with acetone and IPA. Rinse with HPLC grade water and then dry with nitrogen gas. Rinse with the developer and then fill up half way with it.

3. Place the sample in the developer for 70 seconds and gently swirl throughout.

4. Rinse the sample with HPLC grade water for 45 seconds to stop development. Dry with nitrogen gas and place the sample in it's box.

5. Inspect the patterns under the optical microscope to see if the writing process was successful. If the patterns are below 500 nm, they might not be easily visable.

6. Dispose of the used developer.

3.3.3 E-beam lithography standard operating procedure

Beam Current (pA)	Spot Size (Configuration Parameter)
1.6	-9
3.2	-8
6.4	-7
13	-6
25	-5
50	-4
100	-3
200	-2
400	-1
800	0
1600	1
3200	2
6400	3

Table 3.2: Beam current to Spot Size (Configuration Parameter) conversion used for NPGS program to automate switching of the currents during writing.

Preparing Sample

1. Put on latex gloves, eyewear and labcoat.

2. Turn on the hotplate in the fume hood to the baking temperature of the resist.

3. Take 2 small glass beaker (sample) and 1 medium glass beaker (waste) from the clean rack.

4. Clean both small glass beakers with acetone and Kimwipe and rinse with IPA pouring waste into medium glass beaker. Fill 1 small glass beaker with acetone and the other with IPA.

5. Clean carbon fiber tipped tweezers and metal tipped tweezers if baking temperature exceeds 150^o C. Handle the samples with carbon fiber tipped tweezers whenever possible as it prevents unwanted scratching.

6. If sample isn't diced yet, clean 2 glass slides and a sample box with acetone and Kimwipe and rinse with IPA over waste beaker. Dry with nitrogen gas over clean room wipe. Dice off a 10 mm x 15 mm chip from the needed wafer by scoring the needed wafer with a diamond scribe a single time using a glass slide as a guide. Break chip away from wafer by sandwiching the larger side between the glass slides and apply pressure with tweezers on the far edge of the side sticking out. Orientate the chip such that the long axis is horizontal. Using a diamond scribe, softly score the bottom corners vertically and the top corners horizontally for 1 mm. This will be used for sample orientation and creates dust particles for e-beam alignment.

7. Transfer sample to acetone beaker and sonicate the sample for 5 mins.

8. While spraying with IPA, transfer the sample to the IPA beaker and sonicate for 5 mins.

9. Dry with nitrogen gas over clean room wipe and transfer to sample box.

10. Set the nitrogen gas to 60 PSI.

11. Follow wanted resists SOP.

12. Inspect the resist layer to make sure a uniform layer was deposited and place the sample back in sample box.

13. Set the nitrogen gas back to 30 PSI.

Getting SEM Started

1. Log into the reservation system, logbook, and SEM user interface (GUI).

2. If the NPGS program on EBL computer is open, make sure the SEM is on SEM mode and not NPGS mode. A green light on the SEM should be on with the yellow light off. If the yellow light is on, then the SEM is in NPGS mode and word external should be on the SEM computer windows. To switch back to SEM mode, click the SEM button. Close the NPGS program.

3. Restart the EBL computer. Do not log into the NPGS computer after restart yet!

4. Make sure the e-beam is off and then exit the SEM GUI. Once the GUI is stopped, stop the SEM server. Wait until the server is completely stopped (takes a couple mins and the buttons should be gray) and then close out of SEM program. Restart the SEM computer.

5. Log into the SEM computer under supervisor user name (password: supervisor) and start the SEM program. Start the SEM server and wait till it is completely started (takes a couple mins and the buttons should be green) and then start the GUI. Log into the SEM.

6. Log into the EBL computer under supervisor user name (password: supervisor). An auto DAC calibration should start. Make sure you don't do anything on the SEM computer or EBL computer during this time. Once completed, it should request a second calibration, press enter on the EBL computer to start it. After this is completed, open up the NPGS program and the initial start up should be completed. If the auto DAC calibration didn't initiate, open the NPGS program and that should start the calibration.

Loading the Sample

1. Put on latex gloves. Mount the sample on the medium SEM stub with 2 copper clips. Make sure the copper clips are in contact with a conducting part of the sample to ground the sample.

2. Press the "V" button on the quick loader to vent the side chamber and open the lid. Release the quick loader holder from the quick loader arm by moving the handle from position 2 to position 1.

3. Load the sample onto the quick loader holder and secure it using the set screw. Then load it onto the quick loader arm by sliding the holder onto the arm and moving the handle from position 1 to position 2, close the lid, and press the "P" button on the quick loader to pump the side chamber. If the stage isn't in the loading position, it will then move to it when "P" is pressed.

4. Open the load lock by turning its handle downward and then to the left. While holding it open and looking at the stage camera, move the quick loader arm to position 3-5 and then back to 2 in order to transfer the sample to the SEM stage. Close the load lock by pushing its handle right and then back up to its original position. Remove the latex gloves but don't throw them away.

5. Go to the "End" position under the SEM stage position control such that the stage is now centered.

6. Go the the "Stage" drop down menu and select "Take NavCam photo" to take a CCD picture of your sample to aid in positioning the sample.

Sample and Beam Alignment

1. Move the beam to the edge below the bottom left vertical scratch if sample is right side up or above right vertical scratch if sample is upside down.

2. Set the beam voltage to 30 kV and the beam current to the smallest writing current that will be used (typically around 25 pA) and turn on the beam and focus the beam on the edge of the sample.

3. Click "Link Z-Height" making the z now describe the distance between the lens and the sample surface. Set the height (z) to 7 mm.

4. Refocus on the sample edge. Go to the "Stage" drop down menu and select "XT Align Feature". Draw a line going from right to left if sample is upside down or left to right if sample is right side up along the edge of the sample to orientate the sample. Repeat this step once.

5. Select "Take NavCam photo" to retake the CCD picture.

6. Locate a dust particle near the closest scratch.

7. Refocus the beam on the particle. Click "Link Z-Height" and then set to 7mm. Repeat 3 times.

8. Test the communication between the NPGS and SEM computers by clicking the "NPGS" button. The SEM windows should now say "External". Using the NPGS computer, image the dust particle through the NPGS software by using a 150um test window pattern and run file. Open up the run file and make sure the spot size (Configuration Parameter) and current match the lowest current you are using. Run the test window and only allow a single scan by pressing "S" once the scan starts. After the scan finishes, press "a" to autoscale the image and the dust particle should be visable. If not, redo the "Getting SEM Started" steps. If the particle is visable, exit the test window program and click "SEM" to return local control to the SEM.

9. Click "Direct Adjustments" to open up the window to make beam adjustments. Click "Crossover" and center the beam for each current that will be used for writing. Return back to the lowest current that will be used.

10. Refocus the beam and fix the stigmation, lens modulator, and both stigmator modulators.

11. Click "Unlink Z-Height" to return back to absolute z height.

12. Click "Set WD = 7 mm" on NPGS computer.

13. Refocus the particle by moving the stage up and down to 10 microns of sensitivity. Finish focusing normally. Save the stage position.

14. In the NPGS program, select "Direct Stage Control" to start the tilt correction program. Press "Enter" twice on the NPGS keyboard to start collecting a new data set. Press the space bar to acquire first data point. Move to the other 3 corners and focus on a dust particle to set the other points pressing the space bar each time. Exit out of the protocol by pressing "Enter" twice and then "Esc".

15. Return back to the original position and refocus on the particle.

16. Go to the top of the nearest scratch (bottom left) and save this position. Press the "NPGS" button in the NPGS software to return back to "External" control of the SEM.

17. If starting a new chip, proceed to the "Writing Alignment Marks" section. Otherwise, proceed to the "Writing Patterns using Alignment Marks" section.

Writing Alignment Marks

1. Open up the "150um_box" run file and make sure "Layer" is set to "Continuous", "Origin Offset" is set to "0,0", "Center-to-Center Distance" and "Line Spacing" values are set to "40", "Measured Beam Current" and "Spot Size (Configuration Parameter)" is set to "6400" and "3" respectfully, "Multiple Pass Mode" is set to "Disable", and the dosage is set to "Area" and the value needed for that resist and developer. Set

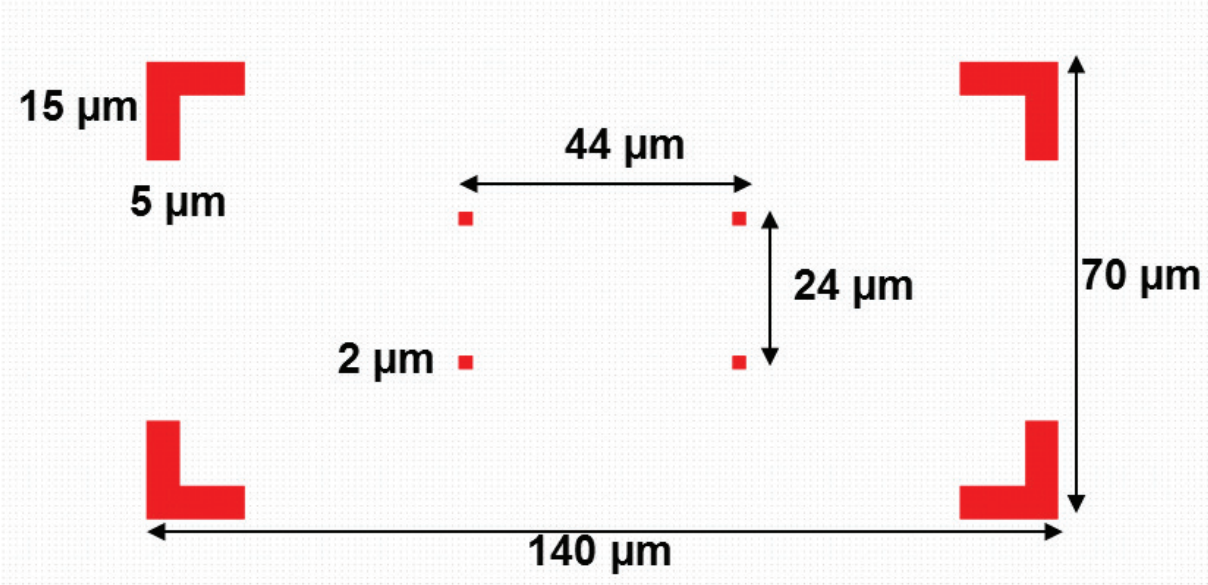

	x_b	21	22	23	24	25	
		20	19	18	17	16	
		11	12	13	14	15	
		10	9	8	7	6	
	x_a	1	2	3	4	5	x_c

Figure 3.8: **Sample alignment marks.** (Top) Layout of the sample alignment marks. (Bottom) Chip outline with 25 devices seperated by 2 mm and 3 global alignment marks that are 1 mm away from the nearest device. Global alignment mark, x_a, is 0.5 mm away from the top of the bottom left scratch.

"Disable Digital SEM Control" to "No" so that the current can be controlled by the NPGS computer. Make sure "Entity Type" is set to "Pattern", "Pattern Name" is set to "150um_box", "Number of Repeats" is set to "0", "XY Move to Pattern Center" is set to "0,0".

2. Move 0.5 mm to the right of the scratch and write the first global alignment mark by running the "150um_box" run file by right clicking the file and select run.

3. Move 8 mm up and write the next global alignment mark.

4. Move 8 mm down and 10 mm to right and write the last global alignment mark.

5. Move left 5 mm and up 4 mm to go to the center of the global alignment marks.

6. Open up the "align_write" run file and make sure "Layer" is set to "Continuous", "Origin Offset" is set to "0,0", "Center-to-Center Distance" and "Line Spacing" values are set to "11", "Measured Beam Current" and "Spot Size (Configuration Parameter)" is set to "50" and "-4" respectfully, "Multiple Pass Mode" is set to "Disable", and the dosage is set to "Area" and the appropiate dosage value for that resist and developer. Set "Disable Digital SEM Control" to "No" so that the current can be controlled by the NPGS computer. Make sure "Entity Type" is set to "Array", "Pattern Name" is set to "align_write", "# of Rows in Pattern Array" and "# of Columns in Pattern Array" is set to "5", "Exposure Steps for Array" is set to "No", "Initial XY Move to Pattern Center" is set to "0,0", and "Array Spacing (Col,Row)" is set to "2000,2000".

7. Save and Close the run file and then run it. The 25 alignment marks should write non-stop. Make sure the first alignment mark is written 1 mm to the right of the first global alignment mark. When writting is finished, proceed to the "Ending the Writing Session" section.

Writing Patterns using Alignment Marks

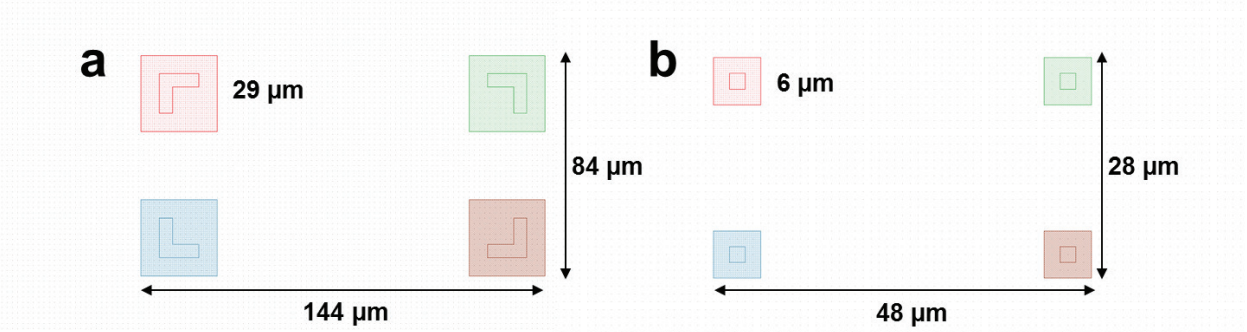

Figure 3.9: **Alignment outlines.** Outiline of the (a) largest_align and (b) medium_align steps. The squares are filled polygons (dashed line) which defines a viewing window. The "L" shapes in (a) and the small boxes in (b) are un-filled (solid line) that match up with the physical objects on the wafer that were written previously. The color of the un-filled and filled shapes are paired such that they belong to the same layer.

1. Move to the first sample location.

2. Open up the wanted run file. If no run file is present for the pattern needed, right click on the pattern file and create a run file. Make sure there are 3 Entity Types and set the first and second ones to "Aligment", "Alignment Mode" to "Manual", "Number of times to repeat" to "1", and "XY Move to Pattern Center" to "0,0". For the first alignment, set "Pattern Name" to "largest_align". For the second alignment, set "Pattern Name" to "medium_align". Set the third to "Pattern", "Pattern Name" to the pattern file that is going to be written, "Number of Repeats" to "0", "XY Move to Pattern Center" to "0,0".

3. Highlight the "Number of entities to process" and then set "Disable Digital SEM Control" to "No" so that the current can be controlled by the NPGS computer.

4. With the third entity selected, make sure "Layer" is set to "Continuous", "Origin Offset" is set to "0,0" and "Multiple Pass Mode" is set to "Disable". Also, set "Center-to-Center Distance", "Line Spacing", "Measured Beam Current", "Spot Size (Configuration Parameter)", dosage type and value to their necessary values for that recipe.

5. Highlight the "largest_align" entity and set "center-to-Center Distance" and "Line Spacing" to "300" and "Measured Beam Current" and "Spot Size (Configuration Parameter)" to the writing parameters being used.

6. Highlight the "medium_align" entity and set "center-to-Center Distance" and "Line Spacing" to "50" and "Measured Beam Current" and "Spot Size (Configuration Parameter)" to the writing parameters being used.

7. Save the run file and exit it.

8. Run the file. Follow instructions on screen to start the large alignment step. Once scan starts, press "S" to perform single scan over the window. Once scan is finished, press "a" to auto-scale the color wheel. Click on the top left window and line up the mask with the scanned imaged using the arrow keys. Repeat over each window and then press "Enter" and then "n" to proceed to the next alignment step. Do it again, but now for the medium alignment step. If alignment was successful, write the pattern, otherwise exit out of the writing process.

9. Move to next sample location and repeat the previous step to completion. Once finished, move on to "Ending the Writing Session" section.

Ending the Writing Session

1. Move the stage to a scratch location and then click the "SEM" button to return back to local control.

2. On the SEM computer, pause the scan, turn off the e-beam, and then move to the "End" position.

3. Put the latex gloves back on and Press the "P" button on the quickloader to move the stage to the unloading position. Open up the load lock value following the same

procedure used in the "Loading the Sample" section. Take the sample out of the main chamber by moving the quick loader from position 2 to 5-3 and then back to 2 again while watching using the video feed. Close the load lock value.

4. Press "V" to vent the load lock chamber. Open the lid and then move the quick loader from position 2 to 1 which will release the quick loader holder. Loosen the set screw and remove the sample holder. Loosen the clips holding down the sample and return the sample back to its holder.

5. Return the quick loader holder back to the load lock and close the lid. Press the "P" button to pump down the side chamber.

6. Log out of the SEM GUI, logbook, and reservation system and throw away the latex gloves.

7. Return to lab and develop the sample according to the recipe being used.

Random Notes

1. Once in a while, the NPGS computer gets stuck on a window. To switch to the correct window, press the "Windows" key and then select the flashing tab.

2. By default, "Spot Size (Configuration Parameter)" doesn't do anything. To enable it, make sure the scope driver (under options/system files/PG-CMND.sys line #9) is set to "scope2.bat".

3. If the current doesn't need to be changed inbetween writing steps, the "Spot Size (Configuration Parameter)" can be set to 99 such that the beam current will remain unchanged. This helps speed up the writing step as it avoids the couple second delay.

4. To create a new pattern file on an outside computer, use Layout Editor to draw the wanted pattern with filled polygons (dashed lines) for areas to be written and a different

layer for each unique writing parameter wanted. Transfer the file to webfiles. Download the file on the SEM support computer and transfer it to the shareddata folder so that it is accessible on the NPGS computer. Switch over the monitor to the NPGS computer and transfer the file from the shareddata folder to the wanted project folder in NPGS. Open up the NPGS program and right click on the gds file and convert it to dc2 using the default options. Open up the now dc2 file in autocad by right clicking on it. Under the NPGS pull down menu in autocad, select "SetDump". Click on a spot that is out of the way of the sample but still near it such that if the beam blanker fails, the sample is not ruined. Press "Enter" 3 times to set the dump point. Save the pattern file by selecting "NPGS:Save" (DO NOT select "File:Save" otherwise file won't work). Follow the instructions from the prompt window and exit the program.

5. If the sample alignment marks are difficult to find when trying to find the first sample location, run the test_window run file in order to locate the alignment marks under a bigger viewing window. Make sure to only do a single scan (press "S") in order to prevent overexposing the sample. Align the mask to the center of the aligment mark pattern. On the bottom of the screen, the distance the mask had to travel is recorded in microns. Move the stage that distance which should then center the beam on the alignment pattern. Try running the wanted pattern now.

6. The maximum distance the NPGS alignment program can handle horizontally (x-direction) is $\sim$ 5 microns. If a mask needs to move more than that, the alignment matrix will error. To overcome this, move the stage the necessary distance and rerun the alignment step.

7. The actual beam current is different than the listed values on the SEM which can affect the dosage required for a device. Measure the actual beam current using a faraday cup (our own) and the nanoammeter (next to SEM monitor) after beam source maintenance or at least once a year.

3.4 Ion milling standard operation procedure

Ion milling using argon plasma is one of the most ubiquitous etching steps in nanofabrication. Argon is used because it is an inert element therefore it limits doping of the material that is wanted to be etched. Additionally, it is heavy enough such that bombardment of electrically neutral argon atoms is enough to knock away almost any type of atom on the surface. This means that argon can be used to etch almost any material, however, at different speeds. For ion milling, the argon plasma is collimated by electric fields thus resulting in an anisotropic etch. This means the etching rate for a material will depend on the angle between the argon plasma and the surface of the sample. This can additionally lead to shadowing, where the argon plasma is blocked by the structure being etched, therefore the sample should aways be rotated when being etched. The following provides instructions on how to use the Intlvac Nanoquest 1 ion mill.

Preparation

1. Make sure the nitrogen isnt empty, the compressed air line is at 60 psi, and the system water cooling pressure is ∼80 psi.

2. Use clean powder free gloves when operating the mill and only use the clean tweezers and screw driver provided.

3. The default state is with the chamber pumped down, the turbo at full speed, the stage chiller turned off manually, and the nitrogen tank closed.

4. The software used to run the Ion mill is called NanoCon Interface and is ran by LabView[44].

5. The logbook is located on the Desktop and is called Ion Mill Logbook.odt with the date that it was started.

Figure 3.10: **Chamber tab for the Ion mill program.** Taken from Intlvac Nanoquest 1 User Manual.

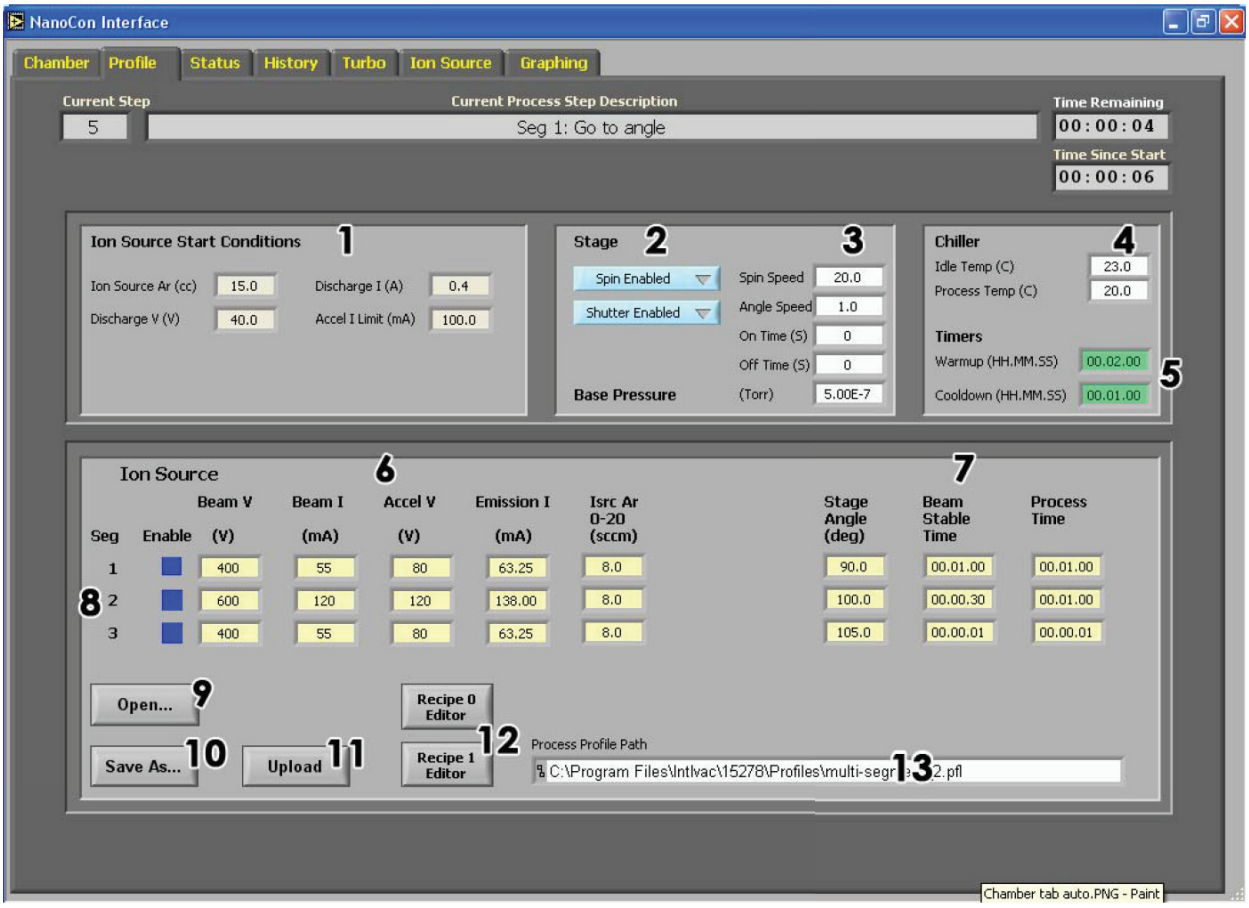

Figure 3.11: **Profile tab for the Ion mill program.** Taken from Intlvac Nanoquest 1 User Manual.

6. The "Abort Process" button (Fig. 3.10 #21) is safe to use when you are unsure if something is wrong.

Preparation

1. Login to the ion mill computer by either using the touch screen or mouse (username=user, password=123) and verify no errors are present on the **Chamber** tab of the NanoCon Interface program. If the stage chiller is turned off, turn it back on by using the switch on the front of the Neslab chiller. If the nitrogen tank is closed, open it slowly. Make sure the stage is at 0 degrees (facing upwards) (Fig. 3.10 #9 and 11). If it is not, contact a super user and dont try to open the chamber door.

2. If the mill is pumped down, start the vent process by pressing and holding the "Vent Chamber" button (Fig. 3.10 #24) until the progress bar is completed (just pressing it will not do anything). This will stop all other processes and will start spinning down the turbo pump. After 15 mins, the system will be vented.

3. Open the chamber door slowly until the stage is accessible. Load in your sample following the relevant loading procedure in the "Sample Loading" section as 3"-4" wafers are loaded differently than individual chips. Inspect the neutralizer filament to make sure it is not broken.

4. Close the chamber door slowly. Making sure not pinch your skin in the door, hold the door close and press and hold the "Pump Chamber" button (Fig. 3.10 #25) until the progress bar is completed. Once you hear the door seal, stop pressing on the door and monitor the pump down process. Once the pressure (Fig. 3.10 #5) reaches 1 mTorr, the turbo pump should start spinning up. Once this state is achieved, it is okay to walk away.

5. Wait until the turbo pump reaches full speed which will take roughly 10 mins. When the turbo reaches speed, the indicator (Fig. 3.10 #19) will turn from "Accelerating" to "At Speed".

6. Load in the profile needed for the etch in the Profile tab by pressing the Open button (Fig. 3.11 #9) which will cause a dialog box to appear. Double click on the profile you want to use which will load in the profile. The only parameter you can change is the active etch time which is called "Process Time". This must be entered in hh:mm:ss format and ignore the duty cycle as the program will calculate the total time need to achieve the etch time you enter. For example, if the duty cycle is set to 15 seconds on and 45 seconds off, while you enter in 00:01:00 for the "Process Time", then the total time will be 3 minutes 15 seconds for the etch step.

7. Inspect the profile to make sure everything is set the way you want it. If there is no recipe available for your need, contact a super user to help create a new one. If everything is okay, press the "Upload" button (Fig. 3.11 #11). Wait for the progress bar to finish before doing anything else as this is writing all of the parameters to memory.

8. Fill out the logbook with all the information you currently have available (the green columns). The information for the blue columns will have to be filled in once the etch has started.

9. Return to the **Chamber** tab and press the "Start Profile" button (Fig. 3.10 #22) when ready to start the etch. Etching wont start until the chiller temperature and the base pressure reach their set points. At this point the stage will rotate to the etch angle, start spinning and the ion source will begin beam warm-up. Inspect the neutralizer current making sure it is nonzero. If it is 0, press the "Abort Process" button (Fig. 3.10 #21) as the neutralizer filament is broken and contact a super user. Dont use the values from this step for the logbook.

10. After beam warm-up, the ion mill will go to the beam stabilization step. During this, the stage will rotate to the angle of the etch and the beam parameters go to the wanted etch parameters. The shutter should be closed during this time. Near the end of this process, record the values needed in the blue columns of the log book. Verify the red column ("Accelerator Current Check (<5%)") is returning "good". If it is not, press the "Abort Process" button (Fig. 3.10 #21) and contact a super user.

11. After beam stabilization, the ion mill will go to the etch process. Make sure the shutter is opening when it is supposed to. When the etch is finished, it will enter a cooldown process. Once this process has ended, the chamber can be vented.

12. Vent the chamber in the same manner as step 2. Unload your sample following step 3 and pump down the chamber again following step 4.

13. Turn off the chiller by pressing the front power button on the chiller. It will enter a 20 second shutdown process. **Do not** turn off the chiller from the button on the back without first doing the shutdown process as this will reduce the life of the chiller. Close the nitrogen tank and then log off.

Sample Loading

Chips

1. Loading individual chips requires the aluminum tapped plate. Tungsten clips provide the mounting force and if more is needed, contact a super user. If the aluminum plate is already attached skip to step 4. If nothing is attached, skip to step 3.

2. Remove 4" wafer holder by loosening the screws holding the titanium ring down. Turn the ring and lift up to remove the ring. Remove the screws and the thermo pad.

3. Place the aluminum plate onto the stage and screw it in place.

4. Clip the samples down by positioning the chip near the clips and carefully lifting up on the clips near the contact point while making sure not to completely remove the clip from the hole and place it onto the chip in the corner. Optimal etching speed is achieved 1" from the center.

3"-4" Wafers

1. Loading wafers requires the use of the thermo pad, titanium ring, vacuum and nitrogen gas. If titanium plate and thermo pad are already attached, skip to step 4. If nothing is attached, skip to step 3.

2. Remove the aluminum plate by removing the screws and then lifting up the plate.

3. Place the thermo pad on the stage. Make sure the pad is clean and centered and on the stage. Insert the screws but only screw in half way.

4. Place the wafer onto the pad and attach the stage line to the stage inlet. If the line cant reach the inlet, jog the stage by pressing the "Jog Stage" button in the chamber tab.

5. Open up the roughing pump vacuum line to the stage (Fig. 3.10 #14) and wait 5 minutes. Close the vacuum line and remove the stage line.

6. Place the titanium ring over the top of the wafer such that the flat part of the ring matches up with the flat part of the wafer and rotate into position. Tighten the screws such that the titanium ring is snug but dont over tighten.

7. To remove, loosen the screws, turn the ring and lift up. Attach the stage line to the stage inlet and open up the nitrogen gas to the stage (Fig. 3.10 #13). Remove the wafer from the pad while being careful not to drop the pad on the ground as it will want to stick to the wafer. Turn off the nitrogen gas to the stage. Realign the pad on the stage and place the titanium ring back on the stage.

3.5 OOMMF Simulations

The following section provides examples of how to write a .mif file for OOMMF in order to perform a spin Hall oscillator simulation where the Oersted field and current density vector where calculated in COMSOL and converted into .ovf files for use. The simulation is also set up such that the current is increased for each stage of the simulation. Additionally, this simulation uses a homebrew class that can include 2 sources of spin torque, one for the current running through the Permalloy and the other through the platinum. For more information on the different classes available in OOMMF, see the OOMMF userguide and look under child classes. Additionally, all units used in OOMMF are in SI. If you want to work in terms of current instead of current density, the spin polarization "P" can be used to convert to current by dividing "P" by the cross-sectional area of the device. If the on state for a input for any class is "1", then the off state is "0". At a minimum for any simulation, a geometry (atlas), mesh, driver, and evolver must be defined.

1. Define any variables that you want to use later using "set" or "Parameter" if the variable needs to be changed during batch processing. If math needs to be done, use "[expr {}]". Examples of how to use these commands is shown in Fig. 3.12(a).

2. Define the sample geometry using "Specify" and then the wanted atlas class. In order for variables to be used inside class, use "[subst {}]", while for use inside a "proc", used for creating scripts, use "global". Fig. 3.12(b) shows an example of how to use the Oxs_ScriptAtlas class which calls a script in the .mif file and assigns names to certain regions in space based on inputs given. The proc returns either 1,2, or 3 based on cell position where 1,2, and 3 correspond to the names in the regions list. Additionally, the name after "Oxs_ScriptAtlas:" defines the name of the whole volume. These regions can later be referenced by these names.

a

```
set zlim   135e-9
set ywire_lim   6000e-9
set ystnorange 1800e-9
set overlap 2100e-9
set ystnocenter [expr {$overlap+$ystnorange/2}]
```

b

```
Specify Oxs_ScriptAtlas:atlas [subst {
    xrange {0 $xlim}
    yrange {$ymin $ymax}
    zrange {0 $zlim}
    regions {taper wire space}
    script_args {rawpt}
    script {taperedwire}
}]
```

Reference name of the whole volume.

```
proc taperedwire {x y z} {
    global ytaper zlim ywire_lim
    if {$y<0 && $z<=[expr {($zlim/(2*$ytaper))*$y+$zlim}] && $z>=[expr {($zlim/(-2*$ytap\
er))*$y}] } {return 1
    } elseif {$y>=0 && $y<=$ywire_lim} {return 2
    } elseif {$y>$ywire_lim && $z<=[expr {$zlim*((-$y/(2*$ytaper))+($ywire_lim/(2*$ytape\
r))+1)}] && $z>=[expr {($zlim/(2*$ytaper))*($y-$ywire_lim)}]} {return 3
    } else {return 3}
}
```

Figure 3.12: **Defining constants and geometry.** **(a)** Example of how to use set, expr, and $. **(b)** Defines the geometry using Oxs_ScriptAtlas and the scipt, taperedwire, that takes in the x, y, and z coordinates.

a

```
#Creates the mesh.
Specify Oxs_RectangularMesh:mesh [subst {
  cellsize {$cellx $celly $cellz}
  atlas :atlas
}]
```

References volume created earlier

b

```
Specify Oxs_Exchange6Ngbr:Py [subst {
  atlas :atlas
  default_A 0
  A {
      taper taper $AvalFree
      taper wire $AvalFree
      wire wire $AvalFree
}
}]
```

References regions created earlier

Figure 3.13: **Defining mesh and exchange field.** **(a)** Defines the mesh by breaking the volume into a regular grid with length in each direction given in cellsize. **(b)** Defines the exchange field.

a

```
Specify Oxs_StageZeeman:Happ [subst {
        script fieldcontrol
        stage_count $total_stages
}]
```

b

```
proc fieldset {Happ x y z} {
global Happ_angle_out Happ_angle_in
       return [list [expr {$Happ*sin($Happ_angle_out)}] [expr {$Happ*sin($Happ_angle_in\
)*cos($Happ_angle_out)}] [expr {$Happ*cos($Happ_angle_in)*cos($Happ_angle_out)}] ]
}
```

c

```
proc fieldcontrol { stage } {
global total_stages Happ_start Happ_step
    set Happ [expr {$Happ_start+$Happ_step*$stage}]
        set spec Oxs_ScriptVectorField
        lappend spec [subst {
        atlas :atlas
        script {fieldset $Happ}
        } ]
        return $spec
}
```

Figure 3.14: **Defining applied field.** **(a)** Defines the applied field for each cell and stage utilizing scripts. **(b)** Sets the field vector based on the angles defined earlier and needs an input to set the strength. **(c)** Sets the field stength based on the stage number.

a

```
#Demag field
Specify Oxs_Demag {}
```

b

```
Specify Oxs_FileVectorField:py_file [subst {
    atlas :atlas
    file  $P_py_filename
    multiplier $pin
}]

Specify Oxs_FileVectorField:pt_file [subst {
    atlas :atlas
    file  $P_pt_filename
    multiplier $gamma_SH
}]
```

Figure 3.15: **Defining demagnetization field and loading vector files.** **(a)** Defines the demagnetization field which is calculated based on the geometry of the device. **(b)** Loads in the polarization files needed for the evolver which makes them available to be referenced.

```
Specify Oxs_StageZeeman:Oersted [subst {
        script OerstedField
        stage_count $total_stages
}]
```

```
proc OerstedField { stage } {
        global start_current step_current zlim oerstedfile cellx
        set current_oersted [expr {-1*($start_current+$step_current*$stage)}]
        set spec Oxs_FileVectorField
        lappend spec [subst {
                atlas :atlas
        file $oerstedfile
                multiplier [expr {$current_oersted}]
                } ]
        return $spec
}
```

Figure 3.16: **Defining Oersted field.** Defines the Oersted field by similar means to the applied field however utilizing a file to define the spatial profile.

3. Define the mesh using "Oxs_RectangularMesh" as seen in Fig. 3.13(a) which splits up the volume into cells. The cell size should be smaller than the exchange length of the material however, if the length along an axis is 2 exchange lengths or less, the cell can be extended to the whole length to save computation time at the cost of some accuracy. Additionally, if the object has curves, smaller cell sizes allow for more accurate simulations due to the reduction of staircasing errors, however, it should be ≥ 5 $\mathring{A}$ to prevent numerical errors.

4. Define the exchange energy using "Oxs_Exchange6Ngbr" as seen in Fig. 3.13(b) where the exchange constant needs to be defined for each region and from one region to another. This specific class is the standard for exchange definition.

5. Define the applied magnetic field that is changed at each stage of the simulation by using "Oxs_StageZeeman" as shown in Fig. 3.14(a). 2 scripts are used in order to control both spatial (Fig. 3.14(b)) and temporal (Fig. 3.14(c)) properties of the field. The stage number is passed to "fieldcontrol" which sets the applied field strength and passes that to "fieldset". Then "fieldset" passes the applied field vector to the "Oxs_StageZeeman" class which applies the field to each cell.

6. Define the demagnetization field using "Oxs_Demag" as shown in Fig. 3.15(a). This is the standard demagnetization class and doesn't include periodic boundary conditions by default.

7. Load in the polarization files for the platinum and permalloy layer using "Oxs_FileVectorField" as shown in Fig. 3.15(b). These polarization files allow for the current density "J" to actually represent the current entering the sample since they convert the current to the spin current density at each cell which was numerically calculated in COMSOL at 1 A and multiplied by the spin polarization of the material. Since this simulation consists of 2 different sources of spin torque, two files are needed.

8. Define the Oersted field, shown in Fig. 3.16, similarily to applied field. Instead of using a script to define the spatial profile, use the Oersted field file that was created externally using COMSOL and Python. This file needs to be loaded in beforehand similarly to how the polarization files were load in Fig. 3.15(b). If no file exists and an analytical solution is available, use a script instead. Since the oersted field arises from the electrical current, and is linearly dependent on current magnitude, the field strength for each cell is multiplied by the current being used in the simulation. Therefore, the Oersted field file or script should in units of field/current.

9. Define the evolver, shown in Fig. 3.17(a), which determines the equation being solved and the spin torque terms. For this simulation, the evolver class used is "Oxs_Test" which is a homebrew class that can take in 2 sources of spin torque. "J_profile" (time dependence of current magnetitude), "alpha" (damping), "mp" (spin polarization direction of first source), "lambda" (symmetry of spin torque), "J" (current magnetitude), "J_direction" (spin current direction of first source), and "P" (spin polarization of first source) are the standard variables used in the standard spin torque evolver, "Oxs_SpinXferEvolve". Additional parameters for this evolver include "propagate_mp" (when set to "1", sets the second spin source to derivative form), "both_currents" (set to "1" to activate second spin source), "fourpt_derivative" (set to "1" to use 4-point derivative if in derivative form), "J_in_direction" (spin current direction of second source), "mp_in" (spin polarization direction of second source if not in derivative form), and "P_in" (spin polarization of second source). The "CurrentProfile" script is shown in Fig. 3.17(b) which sets the time dependence of the current. It can be done using a combination of stage number (if want constant throughout the stage as in this case) or with time (allows time dependent currents needed for spin torque ferromagnetic resonance).

10. Define the driver, as shown in Fig. 3.18(a), which manages the evolver and determines the energy minimization algorithm. This is the standard driver which sets the base-name (the name used for saving the data), number of stages, time length of each stage, the initial magnetization, and the saturation magnetization. Additional outputs can be created here using "projection_outputs", here the magnetization in the area defined by the script is selected, along with setting the output data to either text or binary. If Ms is set to "0", the magnetization dynamics equation isn't calculated there.

11. Send the outputs to "mmArchive" so that they are saved as shown in Fig. 3.18(b). Define what and how often an output is saved using "Schedule".

12. Double check the file for errors and then the .mif file is ready to be used.

a

```
Specify Oxs_Test:evolve [subst {
alpha {Oxs_ScriptScalarField {
    atlas :atlas
    script_args {rawpt}
    script absorbing
}}
  start_dm .01
mp {Oxs_FileVectorField {
        atlas :atlas
        file $mpfile
  } }
P {Oxs_VecMagScalarField {
        field :pt_file
} }
propagate_mp 1
both_currents 1
fourpt_derivative 1
J_in_direction +y
mp_in {0 0 0}
P_in  {Oxs_VecMagScalarField {
        field :py_file
} }
  J_direction +x
  J 1
  J_profile CurrentProfile
  Lambda $Lambda
}]
```

b

```
proc CurrentProfile {stage stage_time total_time} {
    global start_current step_current cellx zlim gamma_SH
    set current [expr {$start_current+$step_current*$stage}]
    return $current
}
```

Figure 3.17: **Defining evolver.** **(a)** Defines the evolver which determines the magnetization dynamics equation being solved. **(b)** The script used to define the time dependence of the current.

a

```
Specify Oxs_TimeDriver [subst {

 basename $Basename
 evolver evolve
 stopping_time $time
 stage_count $total_stages
 mesh :mesh
vector_field_output_format {text %.7g}
 projection_outputs {
    "mx stno" { Oxs_ScriptVectorField {
        atlas :atlas
        script_args {rawpt}
        script {Isostno 1 0 0}
    }}
    "my stno" { Oxs_ScriptVectorField {
        atlas :atlas
        script_args {rawpt}
        script {Isostno 0 1 0}
    }}
    "mz stno" { Oxs_ScriptVectorField {
        atlas :atlas
        script_args {rawpt}
        script {Isostno 0 0 1}
    }}
    }
 projection_options {
    "mx stno" {units A/m}
    "my stno" {units A/m}
    "mz stno" {units A/m}
 }
 Ms  { Oxs_AtlasScalarField {
     atlas :atlas
     default_value 0
     values {
         wire $MsvalFree
         taper $MsvalFree
     }
 }}
m0 {Oxs_FileVectorField {
        atlas :atlas
        file $initmag
}}
}]
```

b

```
Destination output mmArchive
Schedule Oxs_TimeDriver::Magnetization output Stage 1
Schedule DataTable output Step 15
```

Figure 3.18: **Defining driver and outputs.** **(a)** Defines the driver to use which manages the evolver. **(b)** Defines what and when to output.

3.6 Measurement techniques

3.6.1 Electrostatic discharge

Electrostatic discharge is a common cause of nanoscale device failure. This occurs due to the small cross-sectional area of nanoscale devices which can create large current densities at low voltages leading to electromigration, dielectric breakdown, or the vaporization of the

actual device. To prevent this, a grounding strap should be worn at all times when working with nanoscale or other electrostatic sensitive devices. Additionally, a grounding box should be used to separate the device from any dc power components which can be used to switch between live (bare wire) or grounded (sample leads shorted together along with dc supply terminals) to prevent power surges from entering the device. When either voltage or current applied to the sample needs to be changed, it should be swept to the target value to decrease the likelihood of a device death. Lastly, if an amplifer is being used in the circuit, do not power down any equipment or flip any mechanical switches with the amplifer powered.

3.6.2 Standing waves

A common problem in microwave measurements is the pressence of standing waves in the circuit. This will manifest itself in oscillations in frequency of the power at the spectrum analyzer whose period is determined by the length of the circuit. Therefore, longer circuits will have a shorter period of standing waves however, the amplitude of the standing waves will be smaller than shorter circuits due to the increased attenuation in the circuit. This fact can be utilized when a background substraction isn't possible.

When performing a microwave measurement that measures the power delivered to a 50 Ω load, such as using a spectrum analyzer, in the absence of a signal, a standing wave pattern will be observed such as the orange spectrum shown in Fig. 3.19(a). This is caused by the thermal noise in the circuit which is frequency independent. When a signal is present, the signal is seen with the addition of the standing waves as seen in the blue spectrum. In order to remove the standing waves, the signal spectrum is subtracted by the background spectrum thus creating the processed spectrum as shown as the burgundy spectrum in Fig. 3.19(b). The background signal is obtained by either using the opposite current or field polarity that is used to generate the signal. This however, doesn't completely remove the

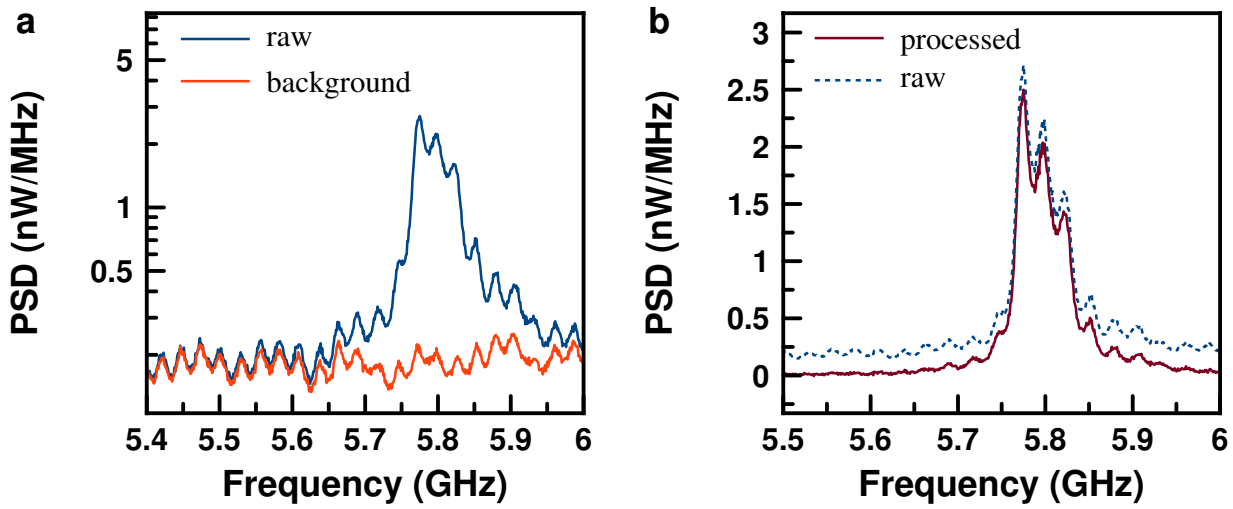

Figure 3.19: **Standing waves in microwave measurements. (a)** Example background spectrum (orange) and signal spectrum (blue) for a self-oscillatory measurement where standing waves are present. **(b)** Processed signal (burgundy) where signal spectrum (dashed blue line) is subtracted by the background spectrum to reduce standing waves.

standing waves as additionally standing waves are created from the voltage of the signal. Therefore, more work is needed to be done to improve signal processing.

3.6.3 Vector Network Analyzer standard operating procedures

Calibrating VNA

1. Navigate menus using the arrow keys and select the highlighted item by pressing **Enter**.
2. To enter a value for a selected menu item, use the number pad and the unit/magnitude keys in the upper right part of the panel.
3. The frequency range of the VNA is from 40 MHz to 40 GHz.
4. The source level and attentuation levels at the receiver circuit for each port can be adjusted in the "Test Signals" menu. The source level ranges from -20-0 dBm and the attenuation at port 1 can be set from 0-70 dB and port 2 can be set from 0-40 dB. The maximum input at each port is 0 dBm.

5. The source is phase locked to an internal 10 MHz crystal reference.
6. S_{xy} refers to the signal that is sourced at y and measured at x.
7. Make sure the cable adapters used are rated up to the frequency range used for the measurement (K-connector needed for 40 GHz operation).
8. If using K-connectors, make sure to use the stronger torque wrench (8 in-lbs, red handle).
9. Avoid spinning the standard 40 GHz cables attached to each port.
10. Make sure you are grounded whenever working with the VNA.

Calibrating VNA

1. Press **Begin Cal**.
2. Select "NEXT CAL STEP."
3. Select "FULL 12-TERM".
4. Select "EXCLUDE ISOLATION".
5. Select "NORMAL".
6. Set frequency range (the larger the frequency range, the larger the frequency step size). Set number of data points to 1601 (max value). Select "NEXT CAL STEP".
7. Make sure "PORT 1 CONN" and "PORT 2 CONN" is set to "K-CONN (M)", "LOAD TYPE" set to "BROADBAND", and "REFLECTION PAIRING" set to "MIXED". Select "TEST SIGNALS" and alter the source level ("POWER CONTROL") and the attenuaton at each port ("PORT 1 ATTN" and "PORT 2 ATTN) such that the signal at each end will be below 0 dBm (protect the input) but above -50 dBm (large enough signal to noise ratio for accurate measurements). Select "START CAL".

8. Follow instructions prompted while using **Enter** to advance. Broadband → 50 Ohm terminator

9. Press **Enter** when done and then **Hold** to stop the measurements in order to prolong the lifetime of the instrument.

Loading Calibration File

1. Press **Save/Recall Menu**

2. Select "RECALL".

3. Select "FRONT PANEL SETUP AND CAL DATA ON HARD DISK".

4. Wait for the hard drive to spin up and select "STANDARD CAL" or the wanted calibration file.

3.6.4 Self-oscillatory signal detection

This section describes how to perform measurements of self-oscillatory magnetization dynamics seen in spin torque oscillators (STO) while section 2.5.5 provides a detailed description of what a STO is. What is important for the measurement of STO is that a magnetoresistance is present in the sample where the electrical current is flowing such that microwave voltage can be generated when the magnetization oscillates. The general formula for the voltage produced is

$$V(t) = V_{dc} + V_{ac}(t) = I_{dc}R_o + I_{dc}\Delta R_{MR} f(\theta(t)) \tag{3.1}$$

where I_{dc} is the dc current supplied to the device, R_o is the base resistance of the device, ΔR_{MR} is the maximum resistance change from the magnetoresistance, $theta$ is the angle

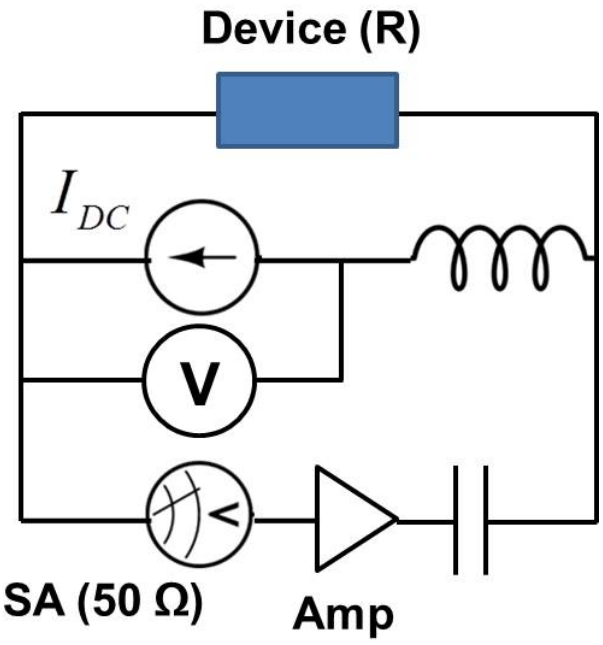

Figure 3.20: **Schematic of STO measurement.** The circuit design to measure magnetic oscillations in a device. The amplifier used should be chosen based on the signal frequency and the needed gain such that the signal is above the noise floor.

of the magnetization, and $f(\theta(t))$ is the function form of the magnetoresistance. The first term is the standard time invariant voltage while the second term is the microwave voltage of interest. Due to the sensitivity of microwave equipment to dc voltage, the dc component of the voltage must be removed, therefore a bias tee is utilized.

An example circuit is shown in Fig. 3.20, where a current source supplies the dc current to the device through the dc only port of the bias tee (inductive part) while the sample is connected to the ac + dc port (bare wire part). Additionally, the dc voltage should be measured such that the resistance of the device at each current is known which can then be used to determine the sample temperature. The ac voltage then passes through the ac port of the bias tee (capacitor part) and to a microwave amplifier and then onto the spectrum analyzer. Since the spectrum analyzer has 50 Ω impedance, the voltage delievered

the spectrum analyzer ignoring the gain from the amplifer is

$$V_{SA} = I_{dc}\Delta R_{MR} f(\theta(t)) \frac{50}{50 + R_o} \tag{3.2}$$

due to the device having finite resistance. This means, the power delievered to the spectrum analyzer in Watts taking into account the gain of the circuit is

$$P_{SA} = (I_{dc}\Delta R_{MR} f(\theta(t)))^2 \frac{50}{(50 + R_o)^2} * 10^{Gain/10} \tag{3.3}$$

where $Gain$ is the net gain in the circuit in dB, amplifier gain subtracted by the attenuation in the circuit. The amplifer used for the measurement is determined by the frequency range of the oscillations and the needed gain to push the power above the noise floor of the spectrum analyzer but not past the 1 dB compression point of the amplifier, the point when the output power becomes nonlinear and such unreliable, nor the maximum input of the spectrum analyzer. Additionally, the amplifier with the lowest noise figure, the amount the noise is amplified in addition to the signal gain, should be used that meets the previous conditions such that the signal to noise ratio is maximized.

3.6.5 Spin torque ferromagnetic resonance measurement

This section describes how to perform spin torque ferromagnetic resonace (ST-FMR) measurements in order to measure the spin wave eigenmodes of a nanostructure while Sec 2.5.4 provides a detailed description of what ST-FMR is. The circuit diagram for this measurement is shown in Fig. 3.21. A microwave generator is used to source the microwave current to the device from the ac port of the bias tee to ac + dc port. This microwave current excite magnetization oscillations at the frequency of the microwave drive which will generate a dc voltage. The magnitude of this voltage is proportional to the microwave current in the device and the differential resistance caused by the magnetoresistance in the sample and the

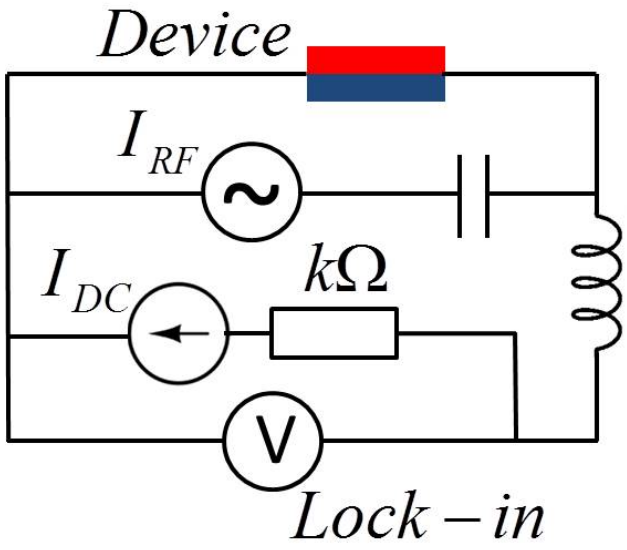

Figure 3.21: **Schematic of STFMR measurement.** The circuit design to measure the spin wave eigenmodes of a device.

magnetic oscillation amplitude. This voltage is then detected by a voltmeter through the dc port of the bias tee.

Additionally, a dc current can be applied to the device through the dc port of the bias tee in order to increase the signal, arises from the equilibrium magnetization change when the spin waves are excited, and to study the effects of spin torque on the spin waves excited. A consequence of adding a current source to the measurement is the reduction of the impedance of the measurement line. An ideal current source has infinite impedance however, this is not the case for the equipment in the lab. Therefore, a 1 $k\Omega$ resistor can be used in series with the current source in order to increase the impedance of the line which will increase the voltage measured by the voltmeter.

This type of measurement can be done in 3 different ways. The first and easiest way is to use a nanovoltmeter to measure the voltage which does not use any modulation techniques. This can only be used when the signal to noise ratio is large therefore it is not often used. The second way is to use amplitude modulation where the microwave current amplitude is controlled by a kilohertz clock whose frequency is a prime number. The voltage

is then measured by a lock-in whose reference signal is sourced by the microwave generator modulation clock. This will then result in only measuring the voltage that has the same periodicity as the reference thus lowering the noise of the measurement. The last way is to use field modulation where, instead of the current amplitude being controlled by a kilohertz clock, the magnet field is instead modified by an addition of a sine wave. This is done by using the internal oscillator of the lock-in and sending it to an audio amplifer such that 3-4 A of current is sourced through a copper wire near the device which generates the low frequency magnetic field. This will modify the spin wave spectrum which will cause the voltage to oscillate due to the oscillating resonance condtion which can then be measured by the lock-in. This will then result in measuring the field derivative of the signal, rather than the signal itself. The magnitude of the voltage depends not only on the usual parameters, but also on the sensitivity of the spin wave dispersion relation on the magnetic field where the larger the change in frequency per gauss, the larger the voltage.

Bibliography

[41] Zheng Duan et al. "Nanowire spin torque oscillator driven by spin orbit torques". In: *Nature Communications* 5 (2014), p. 5616. DOI: doi:10.1038/ncomms6616. URL: http://dx.doi.org/10.1038/ncomms6616.

[42] M.L. Hildner, T.J. Minvielle, and R.J. Wilson. "Epitaxial growth of ultrathin Pt films on basal-plane sapphire: the emergence of a continuous atomically flat film". In: *Surface Science* 396.1-3 (1998), pp. 16–23. DOI: 10.1016/s0039-6028(97)00655-9. URL: http://dx.doi.org/10.1016/S0039-6028(97)00655-9.

[43] Haydn Chen. "Observation of pendellsung fringes in reflection-section topographs of bent silicon crystals". In: *Materials Letters* 4.2 (1986), pp. 65–70. DOI: 10.1016/0167-577x(86)90051-0. URL: http://dx.doi.org/10.1016/0167-577X(86)90051-0.

[44] C ELLIOTT et al. "National Instruments LabVIEW: A Programming Environment for Laboratory Automation and Measurement". In: *Journal of the Association for Laboratory Automation* 12.1 (2007), pp. 17–24. DOI: 10.1016/j.jala.2006.07.012. URL: http://dx.doi.org/10.1016/j.jala.2006.07.012.

Chapter 4

Nanowire spin torque oscillator driven by spin orbit torques

When spin torque from a spin current is applied to a nanoscale region of a ferromagnet, it can act as negative magnetic damping resulting in the excitation of self-oscillations of the magnetization resulting in a 0D spin torque oscillator (STO). In contrast, if the spin torque is uniformly applied to an extended ferromagnet (2D), then the self-oscillatory state is not excited, but rather leads to a reduction of the saturation magnetization. This chapter reports the studies on the effect of spin torque in a nanowire which is an intermediate dimensionality (1D)[41]. Coherent self-oscillations of magnetization are observed in a ferromagnetic nanowire which serves as the active area of a STO driven by spin orbit torques. This work demonstrates that STOs can be excited in 1D systems and can exceed sizes beyond the nanometer length scale.

4.1 Introduction

A current of spin angular momentum incident on a ferromagnet exerts torque on its magnetization and drives it out of equilibrium[12,13]. Owing to its non-conservative nature, this spin torque (ST) can act as effective negative magnetic damping and thereby excite magnetization self-oscillations[38,45]. Spin torque oscillators (STO) have been realized in nanoscale spin valves[8,38,46,47], point contacts to magnetic multilayers[48–50] and nanoscale magnetic tunnel junctions[51–55]. Recently, a new type of STO based on current-induced spin orbit torques in a Permalloy(Py)/platinum(Pt) bilayer was demonstrated[40,56,57]. Spin orbit torques[58–60] in this system can arise from the spin Hall effect in Pt[16,17,22,61–64] and the Rashba effect at the Pt/Py interface[65–68].

In all STOs studied previously, the active region where the negative ST damping exceeds the positive Gilbert damping of the ferromagnet was restricted to nanoscale dimensions. A recent study[39] of spatially uniform ST applied to an extended ferromagnetic film revealed that coherent self-oscillations of magnetization cannot be excited in this two-dimensional (2D) magnetic system. Instead, spin torque was shown to significantly reduce the saturation magnetization of the film[39]. The absence of ST-driven self-oscillations in a 2D ferromagnet was attributed to amplitude-dependent damping arising from nonlinear magnon scattering that prevents any of the multiple interacting spin wave modes of the system from reaching the state of large amplitude self-oscillations. As a result, the energy and angular momentum pumped by ST into the film is redistributed among a large number of spin wave modes leading to reduction of the saturation magnetization of the film. This study raises an important question on the role of the magnetic system dimensionality in ST-induced magnetization dynamics.

In this chapter, it is demonstrated that spatially uniform ST can excite self-oscillations of magnetization in a one-dimensional (1D) magnetic system – a ferromagnetic

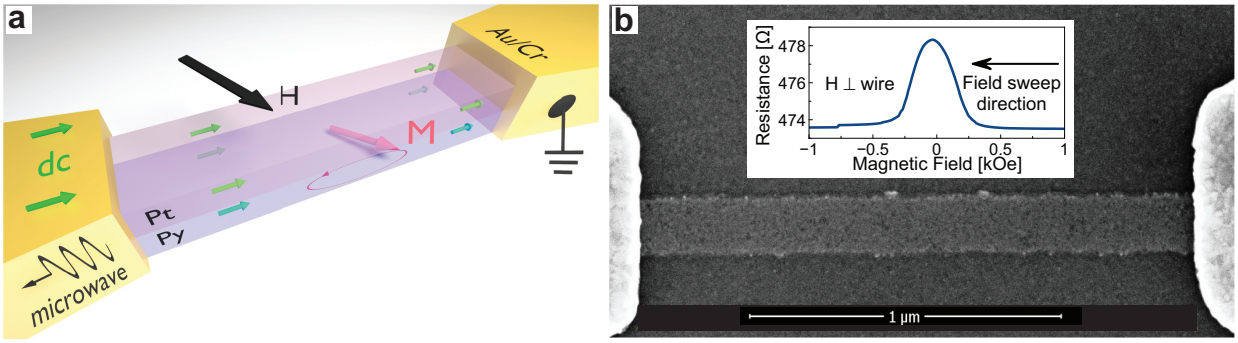

Figure 4.1: **Sample structure.** **(a)** Schematic of a Pt/Py nanowire STO device. **(b)** Scanning electron micrograph of the Pt/Py nanowire STO. The inset shows resistance versus in-plane magnetic field applied perpendicular to the nanowire measured at $T_b = 4.2$ K and a bias current of 0.5 mA.

nanowire. Studies of ST-driven dynamics in a Pt/Py bilayer nanowire are covered, in which SO torques excite self-oscillations of magnetization over a 1.8 μm long active region. This nanowire STO exhibits two types of self-oscillatory modes that directly arise from the edge and bulk spin wave eigenmodes of the Py nanowire. This chapter suggests that geometric confinement of the spin wave spectrum in the 1D nanowire geometry limits the phase space for nonlinear magnon scattering compared to the 2D film geometry and thereby enables STOs with a spatially extended active region.

4.2 Results

4.2.1 Sample description

The nanowire STO devices studied in this work are patterned from Pt(5 nm)/Py≡$Ni_{80}Fe_{20}$(5 nm)/AlO_x(4 nm)/(GaAs substrate) multilayers deposited by magnetron sputtering. Multilayer nanowires that are 6 μm long and 190 nm wide are defined via e-beam lithography and Ar plasma etching. Two Au(35 nm)/Cr(7 nm) leads are attached to each nanowire with a 1.8 μm gap between the leads, which defines the active region of the device as shown in Fig.

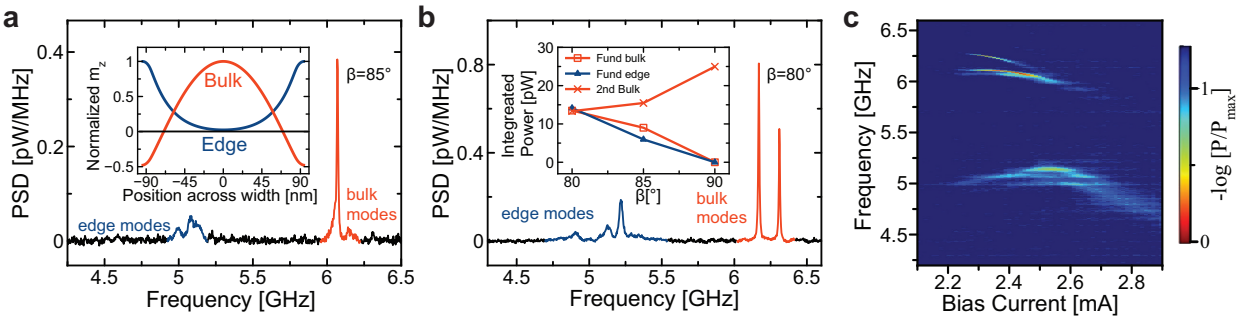

Figure 4.2: **Microwave emission spectra.** Power spectral density (PSD) of the microwave signal emitted by the nanowire at direct current bias $I_{dc} = 2.45$ mA, bath temperature $T_b = 4.2$ K and magnetic field $H = 890$ Oe applied in the plane of the sample at an angle **(a)** $\beta = 85°$ and **(b)** $\beta = 80°$ with respect to the nanowire axis. **(c)** Dependence of the emission spectrum on I_{dc} for $H = 890$ Oe and $\beta = 85°$. The inset in **(a)** shows the spatial profiles of the edge and bulk spin wave modes across the nanowire width given by micromagnetic simulations. The inset in **(b)** shows angular (β) dependence of the integrated power in the fundamental and the second harmonic of the bulk and edge groups of spectral peaks measured at $I_{dc} = 2.4125$ mA and $H = 890$ Oe.

4.1. The resistance of the device measured at bath temperature $T_b = 4.2$ K versus magnetic field applied in the sample plane perpendicular to the nanowire is shown in the inset of Fig. 4.1. This plot reveals that the anisotropic magnetoresistance (AMR) of the Pt/Py bilayer is 1 %.

4.2.2 Electrical measurements

To study self-oscillatory magnetic dynamics excited by SO torques, a saturating magnetic field ($H > 0.5$ kOe) is applied in the plane of the sample in a direction nearly perpendicular to the nanowire axis. In this configuration, SO torques applied to the Py magnetization act as effective magnetic damping[62]. Direct current bias I_{dc} is applied to the nanowire and the microwave signal emitted by the device is measured using a spectrum analyzer[38]. The microwave signal $V_{ac} \sim I_{dc}\delta R_{ac}$ is generated by the AMR resistance oscillations δR_{ac} arising from the magnetization self-oscillations[57]. Microwave signal emission, shown in Fig. 4.2, is only observed above a critical current I_c with the current polarity corresponding to SO

torques acting as negative damping[62]. The microwave emission is measured for five nominally identical devices and similar results for all these samples is found.

For all samples, the microwave emission spectra for $I_{dc} > I_c$ exhibit two groups of closely spaced peaks with a frequency gap between the groups of $\sim$1 GHz. Each group consists of 1 to 4 distinct emission peaks separated from each other by tens of MHz. The high and low frequency groups of peaks appear at similar critical currents. Both groups of peaks are observed in the entire range of magnetic fields (H = 0.5 – 1.5 kOe) employed in this study. For the high frequency group of peaks, microwave emission is observed not only at the fundamental frequency shown in Fig. 4.2, but also at the second harmonic. As illustrated in the inset of Fig. 4.2(b), the emitted power at the fundamental frequency is zero for magnetic field applied at an angle $\beta = 90^\circ$ with respect to the nanowire axis and increases with decreasing β. In contrast, the emitted power in the second harmonic has a maximum at $\beta = 90^\circ$ and decreases with decreasing β. Such angular dependence of the emitted power in the fundamental and second harmonic is expected for a microwave signal arising from AMR. For the low frequency group of peaks, no emission is seen at the second harmonic, which can be explained by the smaller amplitude of magnetization precession reached by these modes and an equilibrium magnetization direction within the mode excitation area being closer to the nanowire axis. Fig. 4.2(c) illustrates the dependence of the emission spectra on I_{dc} for $H = 890$ Oe and $\beta = 85^\circ$.

In order to determine the origin of the microwave emission signals, measurements of the spectrum of spin wave eigenmodes of the nanowire using spin torque ferromagnetic resonance (ST-FMR) is performed[36,37,69]. In this technique, a microwave current I_{ac} applied to the nanowire excites magnetization dynamics in Py by the combined action of current-induced SO torques and the Oersted field from the current in Pt, and thereby generates AMR resistance oscillations at the frequency of the microwave drive[69]. Mixing of the current and resistance oscillations as well as variation of the time-averaged sample resistance in response

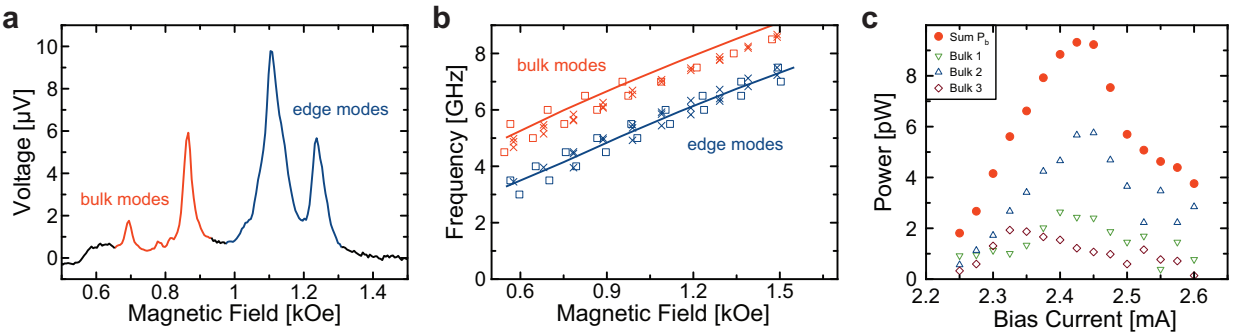

Figure 4.3: **Spin wave modes of the STO. (a)** ST-FMR spectrum of the nanowire device measured at the microwave drive frequency of 6 GHz, $\beta = 85°$ and $I_{dc} = 2.0$ mA $< I_c$. **(b)** Frequency versus magnetic field applied at $\beta = 85°$: (squares) spin wave eigenmodes measured by ST-FMR, (crosses) self-oscillatory modes at I_c and (lines) bulk and edge spin wave eigenmodes given by micromagnetic simulations for an ideal nanowire. **(c)** Bias current dependence of the integrated emitted power in individual peaks of the bulk group of self-oscillatory modes (open symbols) as well as the sum of integrated powers of all bulk modes P_b (crosses).

to the microwave drive[70,71] give rise to a direct voltage V_{dc} that is measured as a function of magnetic field H applied to the sample. Peaks in $V_{dc}(H)$ arise from resonant excitation of spin wave eigenmodes of the nanowire. An ST-FMR spectrum of spin wave eigenmodes measured at $\beta = 85°$, drive frequency of 6 GHz and $I_{dc} = 2.0$ mA $< I_c$ is shown in Fig. 4.3(a).

Similar to the microwave emission spectra, two groups of modes in the ST-FMR spectra are observed. In Fig. 4.3(b), the field dependence of the eigenmode frequencies measured by ST-FMR at $I_{dc} < I_c$ to the frequencies of self-oscillatory modes measured at I_c is compared. This figure demonstrates that the frequencies of all self-oscillatory modes at I_c coincide with the frequencies of spin wave eigenmodes of the system measured by ST-FMR. Therefore, all self-oscillatory modes of the system arise directly from spin wave eigenmodes of the nanowire. This type of eigenmode self-oscillation is qualitatively different from the spin wave bullet mode excited by SO torques in a planar point contact to an extended ferromagnetic film[40]. The bullet mode is a nonlinear type of oscillation, self-localized to a

region with dimensions below 100 nm and with frequency below the spectrum of spin wave eigenmodes of the film[72].

It is well known that spin wave eigenmodes of a transversely magnetized thin-film ferromagnetic nanowire can be classified as bulk and edge eigenmodes[73–75]. These eigenmodes have spatially inhomogeneous profiles along the wire width with reduced (enhanced) amplitude near the wire edges for the bulk (edge) eigenmodes. The frequencies of the edge spin wave modes lie below those of the bulk modes due to reduced internal magnetic field near the wire edges[73]. The frequencies of all eigenmodes are sensitive to the values of magnetic parameters of the Py film, which are different from their bulk values due to the influence of proximate nonmagnetic layers. In addition, the frequencies of the edge modes depend on the edge roughness and spatial variation of the film magnetic properties (magnetic dilution) at the nanowire edges induced by etching[75].

The future section 4.2.4 describes how micromagnetic[34] fitting of three sets of experimental data: (i) wire resistance versus in-plane magnetic field, (ii) wire resistance versus out-of-plane magnetic field and (iii) quasi-uniform spin wave mode frequency versus magnetic field applied parallel to the wire axis can be used to determine the values of saturation magnetization M_s= 608 emu/cm^3, surface magnetic anisotropy $K_s = 0.237$ erg/cm^2 and edge dilution depth $D = 10$ nm, where D is defined as the distance from the wire edge over which magnetization linearly increases from zero to the full film value[75]. These values of M_s, K_s and D are consistent with previous studies of thin Py nanomagnets[76–78]. Using these values of the nanowire magnetic parameters and assuming translational invariance along the nanowire axis, micromagnetic simulations are performed to find the spectrum of spin wave eigenmodes for magnetic field applied in the sample plane at $\beta = 85^\circ$ discussed in section 4.2.4. This shows that the two lowest frequency spin wave modes are the edge and bulk modes, whose spatial profiles (defined as normalized out-of-plane amplitude of dynamic magnetization m_z)

across the wire width are shown in the inset of Fig. 4.2(a). The frequencies of these two modes versus in-plane magnetic field are shown in Fig. 4.3(b).

It is clear from Fig. 4.3(b) that the frequencies of the calculated edge (bulk) modes are similar to the low (high) frequency groups of eigenmodes measured by ST-FMR and observed in STO measurements. This shows that the high (low) frequency groups of experimentally observed eigenmodes are closely related to the bulk (edge) eigenmodes of an ideal nanowire with translational invariance along the nanowire axis. Quantization along the wire results in splitting of the ideal nanowire eigenmode peaks, consistent with the experimentally observed fine frequency splitting within the high- and low-frequency groups of eigenmodes. The validity of this interpretation of the origin of the fine mode splitting, as opposed to e.g. symmetry breaking due to structural disorder of the wire edges, is demonstrated by the spatially resolved BLS data shown in Fig. 4.5(b) in section 4.2.3. Fig. 4.3(c) shows the dependence of the integrated microwave power emitted by the STO device on direct bias current I_{dc} for the three spectral peaks comprising the bulk group. The sum of the integrated powers in the three peaks versus I_{dc} is shown as well. Although the power in each individual peak exhibits irregularities as a function of I_{dc}, the sum of integrated powers of the entire group of bulk peaks is a smooth function of I_{dc}. This further suggests that the finely spaced peaks within the group arise from the splitting of a single peak by longitudinal quantization. The same trend is found for the edge group of peaks.

The precession cone angle θ_b achieved by the bulk mode in the self-oscillatory regime is estimated by assuming that the oscillation profile is approximately uniform along the wire length and define θ_b as the maximum angle of deviation of the magnetization from its equilibrium direction. θ_b is calculated by equating the experimentally measured integrated power in the bulk group of peaks P_b to the integrated power generated by the bulk mode of amplitude θ_b in an ideal nanowire as shown in section 4.2.5. This analysis shows that the maximum precession cone angle $\theta_b \approx 19^\circ$ is achieved at I_{dc} =2.425 mA. Although this value

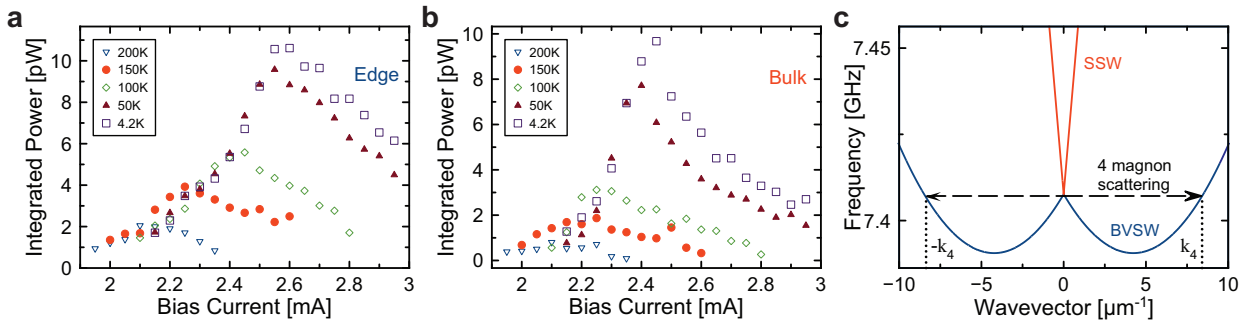

Figure 4.4: **Temperature dependence of the emission spectra.** Bias current dependence of the integrated microwave power emitted by the bulk **(a)** and edge **(b)** spin wave modes measured at $\beta = 85°$, $H = 890$ Oe and several values of the bath temperature T_b. **(c)** Spin wave dispersion relation for BVSW and SSW modes of a 5 nm thick Py film at $H = 890$ Oe[79]. Arrows indicate energy- and momentum-conserving four-magnon scattering of two uniform mode magnons into two BVSW magnons with wave vectors k_4 and $-k_4$.

of θ_b is only an approximate estimate, it clearly shows that large precession cone angles are achieved in the auto-oscillatory regime. The maximum precession cone angle of the edge mode is estimated to be $\theta_e \approx 14°$. The large values of the integrated power emitted by the nanowire exclude the possibility that the observed microwave emission originates from magnetization oscillations localized within a small fraction of the nanowire's active region. This further corroborates the conclusion that SO torques excite spin wave eigenmodes of the system that occupy the entire length of the nanowire STO active region.

Measurements of the microwave signal emission as a function of temperature are also performed. Figs. 4.4a and 4.4b show the the dependence of the total integrated power in the bulk and edge groups of peaks measured at several values of the bath temperature T_b. The integrated power decreases with increasing T_b and vanishes at $T_b \approx 250$ K. The actual temperature of the nanowire is significantly higher than T_b due to Ohmic heating. The nanowire temperature can be estimated from measurements of the nanowire resistance as functions of T_b and I_{dc}[57] which is discussed in section 4.2.6. For $T_b = 4.2$ K, the actual nanowire temperature at I_c is approximately 150 K.

4.2.3 BLS measurements

In order to better understand the nature of the self-oscillatory dynamics induced by SO torques in the Pt/Py nanowire system and to directly confirm that the self-oscillatory modes occupy the entire active region of the nanowire, micro-focus Brillouin light scattering (BLS) measurements[80] of the current-driven magnetization dynamics in this system are performed. Since a 5 nm thick layer of Pt is not sufficiently transparent for BLS studies, a separate batch of samples was made for BLS measurements with the reverse order of deposition of the AlO_x, Py and Pt layers. These AlO_x(2 nm)Py(5 nm)/Pt(5-7 nm)/(sapphire substrate) nanowire samples are prepared by e-beam lithography and liftoff technique as described in section 4.4.1. The microwave signal emission from these samples is similar to that of the previous samples, with two notable differences: (i) the amplitude of self-oscillations of the edge mode is significantly higher than that of the bulk mode and (ii) the microwave emission from the edge mode persist up to room temperature. These differences are likely to originate from the different sample fabrication procedures: the lift-off fabrication process creates less nanowire edge damage than the Ar plasma etching process.

The main results of the BLS measurements are presented in Fig. 4.5. Fig. 4.5(a) shows a representative BLS spectrum measured by placing the probing laser spot at the center of the nanowire. In agreement with the results of electronic measurements of samples with Pt on top, the BLS spectrum exhibits a series of auto-oscillation peaks with the typical frequency separation of several hundred megahertz, which belong to the group of edge modes. By using the high spatial resolution of the BLS measurements, individual auto-oscillation peaks within the group are identified. For this the BLS detection frequency is fixed at the frequency of one of the peaks and spatial profiles of the dynamic magnetization are recorded by moving the probing laser spot along the nanowire axis with the spatial step size of 50 nm. As seen in Fig. 4.5(b), the spatial profiles corresponding to the two peaks are fundamentally different. While the profile for the first edge mode exhibits a slightly

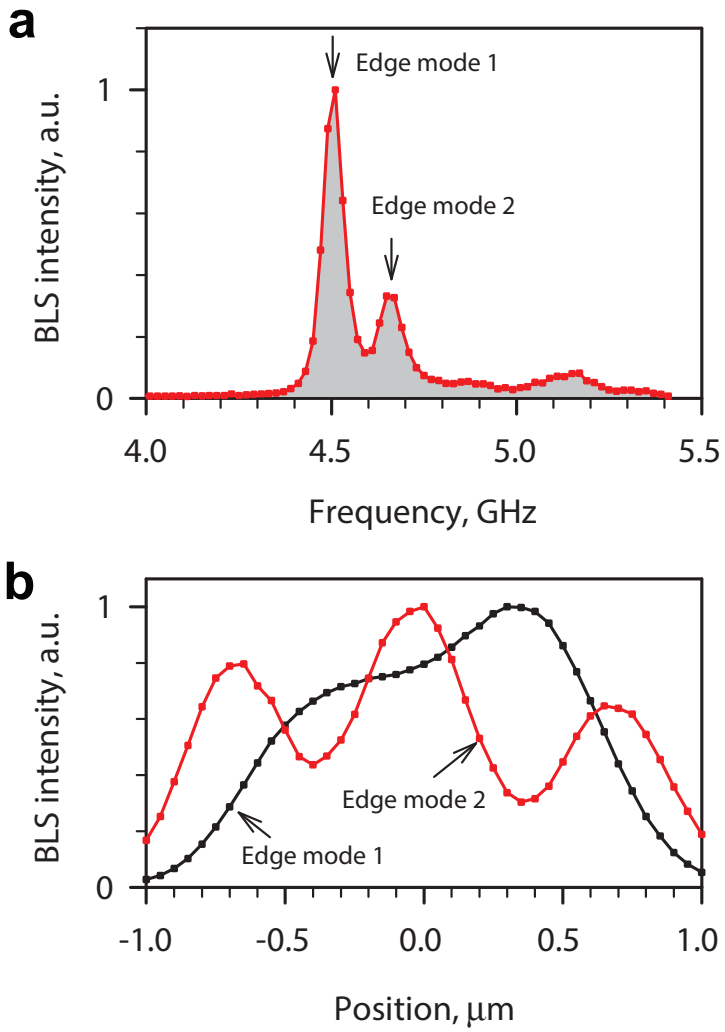

Figure 4.5: **BLS characterization of the auto-oscillating modes.** **(a)** BLS spectrum acquired by placing the probing laser spot at the center of the nanowire. BLS intensity is proportional to the intensity of the dynamic magnetization. **(b)** Spatial profiles of the intensity of the dynamic magnetization in the section parallel to the nanowire axis. The data were obtained at H=550 Oe and the bias current of 2.4 mA.

distorted bell-like shape, the profile for the second peak possesses three maxima. Based on the obtained data it is concluded that the individual auto-oscillation peaks within the groups correspond to the standing-wave modes quantized in the direction parallel to the nanowire axis[81]. The first peak corresponds to the combination of the fundamental mode having no nodes and the antisymmetric mode possessing one nodal line at the center. These two modes are indistinguishable in the spectrum, likely due to their small frequency separation. The second peak apparently corresponds to the mode possessing two nodal lines at the positions of the minima of the measured profile. It is important to note that since the BLS technique is sensitive to the intensity of the dynamic magnetization, the measured profile does not show a change of the sign across the positions of the nodal lines.

4.2.4 Material parameters of the Permalloy nanowire

Magnetic properties of the Py film in the Pt(5 nm)/Py(5 nm)/AlO_x(4 nm)/(GaAs substrate) nanowire samples are expected to differ from those of bulk Py. Previous studies of thin Py films interfaced with non-magnetic metallic layers and alumina have shown reduction of the saturation magnetization M_s[76] and presence of perpendicular surface anisotropy K_s[77,82]. In addition, patterning of the film into nanowires by Ar plasma etching creates material intermixing at the nanowire edges and results in magnetic edge dilution[75,78]. Therefore, in order to be able to predict the spectrum of spin wave eigenmodes of the nanowire, relevant magnetic parameters of the Py layer need to be extracted from experiment. This section expains how micromagnetic[34] fitting of three sets of experimental data: (i) wire resistance versus in-plane magnetic field, (ii) wire resistance versus out-of-plane magnetic field and (iii) quasi-uniform spin wave mode frequency versus magnetic field applied parallel to the wire axis is used to determine approximate values of saturation magnetization M_s, surface magnetic anisotropy K_s and the edge dilution depth D.

The value of the exchange stiffness of bulk Py $A \approx 10^{-6}$ erg/cm is known only approximately[83,84] due to the lack of reliable direct methods for measuring this quantity. It is also known that the value of A is usually reduced in thin films and nanomagnets compared to its bulk value[85]. In order to estimate the value of A for the Py layer in the nanowire device, the scaling relation $A \sim M_s^2$ and the value of saturation magnetization $M_s = 608$ emu/cm^3 extracted from the micromagnetic fit described below is used. This scaling predicts the exchange stiffness to be approximately half of the bulk value, and thus $A = 5 \times 10^{-7}$ erg/cm is adopted throughout all micromagnetic simulations in this chapter. Also, a thin-film value of the spectroscopic g-factor (g = 2.03) measured for a 5 nm thick Py film is employed[86]. For quantification of the magnetic edge dilution, the model developed in Ref. [75] is adopted, in which the saturation magnetization varies linearly from zero at the wire edge to the full film value M_s over the edge dilution depth D.

The micromagnetic fitting procedure begins by fitting the data of the normalized wire magnetoresistance $\hat{R}$ as a function of magnetic field H_{ip} applied in the plane of the sample perpendicular to the wire axis (Fig. 4.6 (a)). This is a convenient starting point because $\hat{R}(H_{ip})$ is independent of K_s, which directly establishes a relation between M_s and D through micromagnetic fitting to the $\hat{R}(H_{ip})$ data in Fig. 4.6 (a). The 190 nm wide, 5 nm thick Py nanowire is divided into 2 nm $\times$ 1 nm $\times$ 5 nm micromagnetic cells and the equilibrium configuration of magnetization for a given value of H_{ip} is found. Then the wire resistance R is calculated by dividing the wire onto $N = 190$ Py(5 nm)/Pt (5 nm) bilayer strips (each strip is 1 nm wide) along its length and use the equation for resistors connected in parallel to calculate the wire resistance $R = \left(\sum_{i=1}^{N} R_i^{-1}\right)^{-1}$. The resistance of each strip R_i ($i = 1..N$) is calculated according to the AMR formula: $R_i = \tilde{R}_0 + \Delta\tilde{R}_i \cos^2(\theta_i)$, where $\tilde{R}_0 = NR_0$ is the resistance of the Py(5 nm)/Pt (5 nm) bilayer strip magnetized perpendicular to the strip axis, $\Delta\tilde{R}_i$ is the full AMR of the i-th strip, R_0 is the resistance of the nanowire magnetized perpendicular to the nanowire axis $\Delta R = \left(\sum_{i=1}^{N} \left(NR_0 + \Delta\tilde{R}_i\right)^{-1}\right)^{-1} - R_0$ is the full AMR of the nanowire and θ_i is the angle between magnetization in the i-th strip and

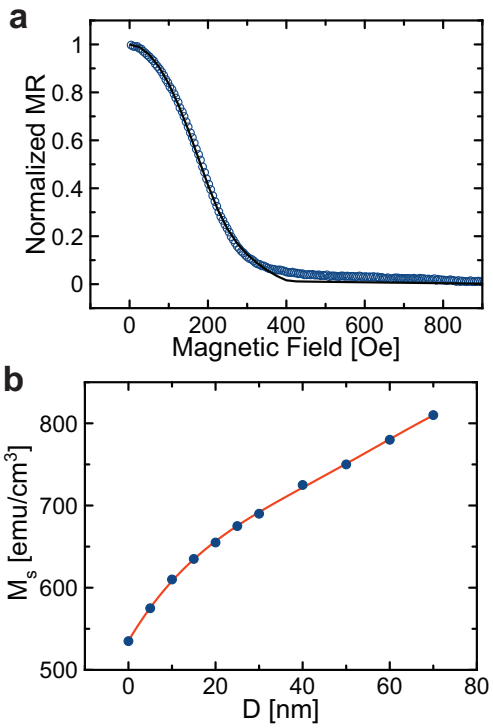

Figure 4.6: **Saturation magnetization and edge dilution depth.** **(a)** Normalized magnetoresistance of a 190-nm wide Pt(5 nm)/Py(5 nm) nanowire measured as a function of magnetic field applied in the plane of the sample perpendicular to the nanowire axis (circles). The solid line shows a micromagnetic fit to the data for the edge dilution depth $D = 10$ nm, which gives the value of $M_s = 608$ emu/cm^3. **(b)** Circles show the dependence of M_s on D given by the micromagnetic fit to the data in **(a)**. The line is a fourth order polynomial fit to the data.

the nanowire axis. This equation for calculating the wire resistance is a good approximation because $\Delta R \ll R_0$ and the resistivities of Py and Pt are similar to each other. The simplifying assumption that $\Delta\tilde{R}_i$ in the i-th strip is proportional to the value of M_s in this strip[26] is made so that AMR is reduced at the nanowire edges due to the magnetic dilution.

Several values of the edge dilution depth D is chosen between 0 and 70 nm, and for each value of D a set of micromagnetic simulations is performed to determine the value of M_s that gives the best fit to the $\hat{R}(H_{ip})$ data. The resulting dependence of M_s on D is shown by circles in Fig. 4.6 (b). A fourth order polynomial fit to the data is performed and shown in Fig. 4.6 (b) which thereby establishes the functional dependence $M_s(D)$ that is used throughout the rest of the micromagnetic simulations.

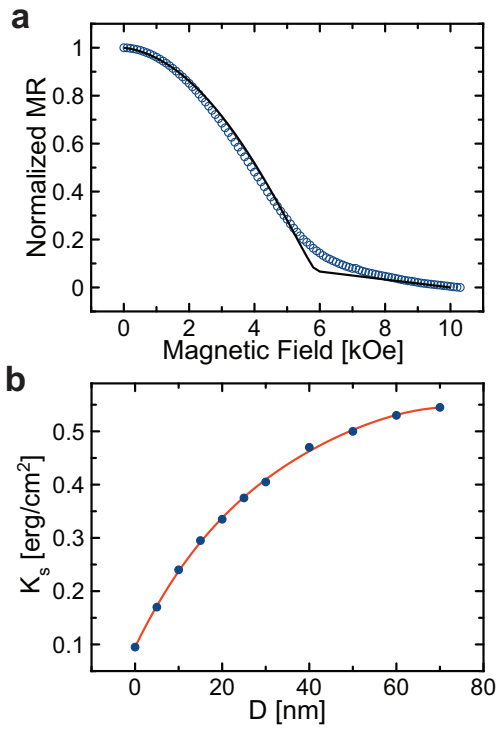

Figure 4.7: **Magnetic anisotropy and edge dilution depth. (a)** Normalized magnetoresistance of a 190-nm wide Pt(5 nm)/Py(5 nm) nanowire measured as a function of the magnetic field applied normal to the sample plane (circles). The line shows the micromagnetic fit to the data for the edge dilution depth $D = 10$ nm, which gives the value of $K_s = 0.237$ erg/cm^2. **(b)** Circles show the dependence of K_s on D given by the micromagnetic fitting to the data in **(a)**. The line is a fourth order polynomial fit to the data.

The fit of the normalized nanowire magnetoresistance data measured as a function of magnetic field H_{op} applied perpendicular to the sample plane is shown in Fig. 4.7(a). A set of micromagnetic simulations is performed for several values of the edge dilution depth D between 0 and 70 nm, and for each value of D, the value of K_s is found that gave the best micromagnetic fit to the $\hat{R}(H_{op})$ data in Fig. 4.7(a). In these simulations, the function $M_s(D)$ established in the $\hat{R}(H_{ip})$ fitting is used. The resulting dependence of K_s on D is shown by circles in Fig. 4.7(b). Fitting a fourth order polynomial to the data in Fig. 4.7(b) gives the functional relation $K_s(D)$ that is used throughout the rest of the micromagnetic simulations.

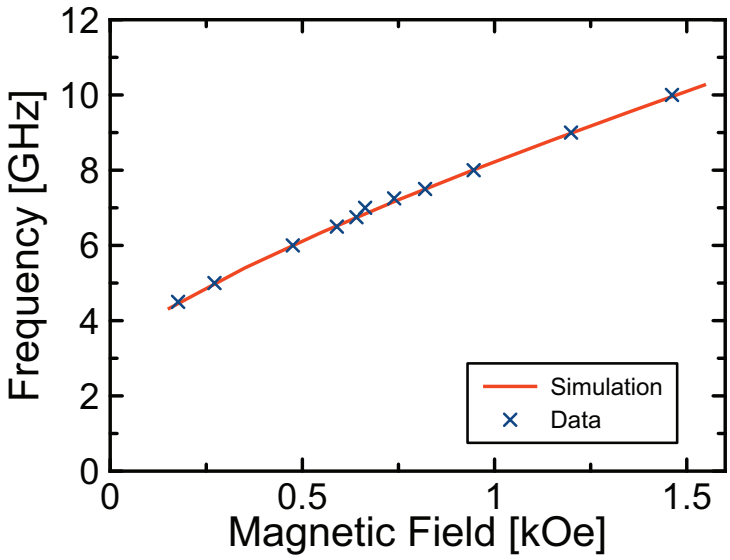

Figure 4.8: **Frequency verses field along easy axis.** Frequency f_q of the quasi-uniform spin wave mode of the nanowire as a function of magnetic field $H_{||}$ applied parallel to the nanowire axis. Crosses show the experimental data measured by ST-FMR, the line is the micromagnetic calculation result for the edge dilution depth $D = 10$ nm.

In order to determine the value of D that best describes the properties of the nanowire device, measurements of the quasi-uniform spin wave mode frequency f_q as a function of magnetic field $H_{||}$ applied parallel to the nanowire axis is used. These measurements are made by the spin torque ferromagnetic resonance (ST-FMR) technique[36,37] described in section 4.2.2. The measured dependence of f_q on $H_{||}$ is shown by crosses in Fig. 4.8. To find the theoretical dependence $f_q(H_{||})$, micromagnetic simulations is employed to calculate the spectrum of spin wave eigenmodes of the nanowire. For these simulations, a pulse of SO torque and a pulse of Oersted field is simultaneously applied to the nanowire magnetization. Both pulses are generated by a spatially uniform sinc-shaped current pulse applied to the nanowire[87]:

$$I(t) = I_0 \frac{\sin(2\pi f_c t)}{2\pi f_c t} \tag{4.1}$$

Such a current pulse excites all spin wave eigenmodes of the system that have amplitude profiles symmetric with respect to the nanowire center and have frequencies below the cutoff

frequency $f_c = 20$ GHz. The current pulse amplitude is chosen to be small enough that the magnetization dynamics remains in the linear regime. The magnetization of each micromagnetic cell is recorded as a function of time and then Fourier transformed. Peaks in the Fourier transform amplitude of the dynamic magnetization correspond to frequencies of spin wave eigenmodes of the nanowire. For a magnetic field $H_{||}$ applied along the length of the nanowire, the simulations show that the lowest frequency mode is the quasi-uniform spin wave mode without nodes along the wire width. The simulations show that the frequency of this mode depends on the edge dilution depth D and therefore can be used with the experimental data in Fig. 4.8 to determine the value of D appropriate for the nanowire device. Using the functions $M_s(D)$ and $K_s(D)$ established by the magnetoresistance data fitting, a single parameter (D) fit of the data in Fig. 4.8 is performed and the best agreement with the data for $D = 10$ nm is found. The solid line in Fig. 4.8 shows the best fit to the data for $D = 10$ nm.

The micromagnetic fitting described above gives the set of magnetic parameters accurately describing the magnetic properties of the nanowire device: $D = 10$ nm, $M_s(10\text{ nm}) = 608$ emu/cm^3 and $K_s(10\text{ nm}) = 0.237$ erg/cm^2. Using these parameters, micromagnetic simulations are performed to determine the spectrum of the nanowire spin wave eigenmodes for magnetic field applied in the plane of the sample at the angle $\beta = 85°$ with respect to the nanowire axis. As in the easy-axis field case described above, a pulse of SO torque and Oersted field generated by a spatially uniform sinc-shaped current pulse is applied and the spin wave eigenmode frequencies is determined from the positions of spectral peaks in the Fourier transform of the time-dependent dynamic magnetization. The lowest frequency mode is found to be the edge eigenmode, whose amplitude is maximum at the wire edge. Its spatial profile across the wire width is shown in the inset of Fig. 4.2. The next lowest frequency mode has bulk character and exhibits maximum amplitude in the center of the wire as shown in the inset of Fig. 4.2. Solid lines in Fig. 4.3 show the calculated dependence of frequencies of these two modes on the applied magnetic field.

4.2.5 Precession Cone Angle Estimate

In this section, the precession cone angle θ_b achieved by the bulk mode in the self-oscillatory regime is estimated based on comparison of the measured integrated power P_b in the bulk group of microwave emission peaks to the integrated power predicted to arise from self-oscillations of the bulk mode with the amplitude θ_b in an ideal nanowire. The bulk mode profile across the nanowire width for an ideal nanowire is calculated micromagnetically as described in the previous section and is shown in the inset of Fig. 4.2(a).

The measured integrated power at the fundamental frequency emitted by the bulk group of modes P_b (corrected for frequency-dependent attenuation and amplification in the measurement circuit) is plotted as a function of direct bias current I_{dc} inFig. 4.3(c). This power is directly related to the amplitude of the nanowire resistance oscillations δR_{ac1} at the fundamental frequency of magnetization self-oscillations. The microwave voltage generated by the nanowire STO device at the fundamental frequency of the bulk mode $I_{dc}\delta R_{ac1}$ is detected by a 50 Ohm microwave spectrum analyzer as microwave power P_b[38]:

$$P_b = \frac{1}{2R_{50}} \left(I_{dc}\delta R_{ac1} \frac{R_{50}}{R + R_{50}} \right)^2 \tag{4.2}$$

where $R_{50} \equiv 50$ Ohm is the spectrum analyzer impedance and R is the nanowire resistance. From this equation, the amplitude of resistance oscillations at the fundamental frequency as a function of the emitted power is expressed as:

$$\delta R_{ac1} = \frac{R + R_{50}}{I_{dc}\sqrt{R_{50}}} \sqrt{2P_b} \tag{4.3}$$

On the other hand, δR_{ac} for a given value of θ_b can be calculated from the micromagnetic bulk mode profile shown in the inset of Fig. 4.2(a). For this calculation, the wire is divided into $N = 190$ strips along its length and an approximate time dependence of the in-plane

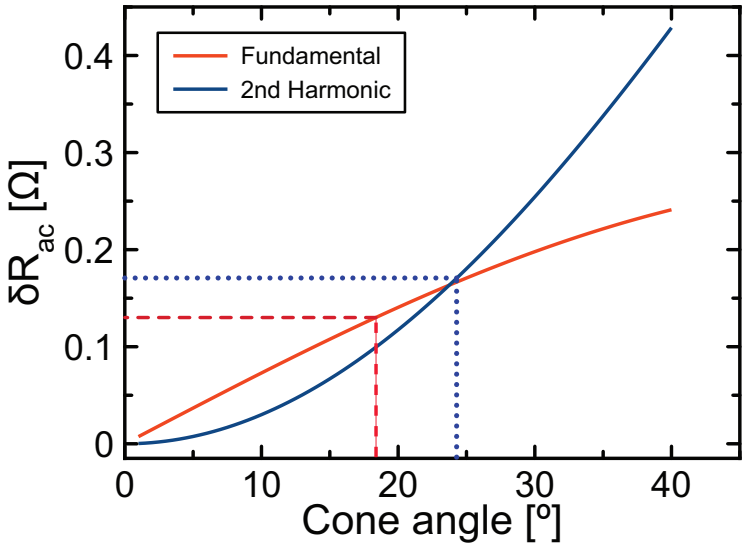

Figure 4.9: **Differential resistance verses cone angle.** Dependence of the amplitude of resistance oscillations at the fundamental frequency δR_{ac1} and the second harmonic δR_{ac2} of the bulk mode on the precession cone angle θ_b. The solid lines are theoretical curves based on micromagnetic simulations of the bulk mode profile. The horizontal dashed and dotted lines mark the amplitude of resistance oscillations at the fundamental frequency and the second harmonic determined from the measured values (at $I_{dc} = 2.4125$ mA) of the integrated power in the fundamental ($P_b = 9.0$ pW) and second harmonic ($P_{b2} = 15.5$ pW) of the bulk group of peaks.

angle $\theta_i(t)$ of magnetization is calculated with respect to the nanowire axis in the i-th strip according to the following equation:

$$\theta_i(t) = \theta_{i0} + a_i \theta_b \sin(\omega t + \varphi_i) \tag{4.4}$$

In this expression, θ_{i0} is the equilibrium direction of magnetization in the i-th strip, a_i is the normalized bulk mode profile shown in the inset of Fig. 4.2(a) ($a_i = 1$ in the wire center), ω is the bulk mode angular eigenfrequency, φ_i is the phase of the bulk mode in the i-th strip and θ_b is the precession cone angle of the bulk mode (defined as the precession cone angle in the center of the nanowire).

Next, the AMR formula is employed to calculate the time dependence of resistance $R_i(t)$ of the i-th strip:

$$R_i(t, \theta_b) = \tilde{R}_0 + \Delta\tilde{R}_i \cos^2(\theta_i(t)) \tag{4.5}$$

Finally, the time dependent resistance of the nanowire is calculated as:

$$R(t, \theta_b) = \left(\sum_{i=1}^{N} \frac{1}{R_i(t, \theta_b)} \right)^{-1} \tag{4.6}$$

This expression is then expanded into a Fourier series to find the amplitudes of resistance oscillations at the fundamental frequency δR_{ac1} and the second harmonic δR_{ac2}. Fig. 4.9 shows the calculated δR_{ac1} and δR_{ac2} as functions of the precession cone angle θ_b. The horizontal dashed line in this figure marks the the value of δR_{ac1} determined via Eq. 4.3 from the experimentally measured integrated power $P_b = 9.0$ pW at $I_{dc} = 2.4125$ mA and $H = 890$ Oe applied at angle $\beta = 85°$ with respect to the nanowire axis. The intersection of this line with the theoretical curve $\delta R_{ac1}(\theta_b)$ gives an estimate of the precession cone angle $\theta_b \approx 18.4°$ at these current and field values. The horizontal dotted line in this figure is δR_{ac2} evaluated via Eq. 4.3 from the measured integrated power in the second harmonic $P_{b2} = 15.5$ pW for the same current and field bias values. The intersection of this line with the theoretically calculated $\delta R_{ac2}(\theta_b)$ gives an independent estimate of the precession cone angle $\theta_b = 24.3°$. The few degree difference between these two estimates of θ_b most probably arises from simplifications of the theoretical model assuming perfect nanowire with translational invariance along the wire axis. Nevertheless, these two independent estimates show that precession cone angles can reach values of tens of degrees in the regime of self-oscillations.

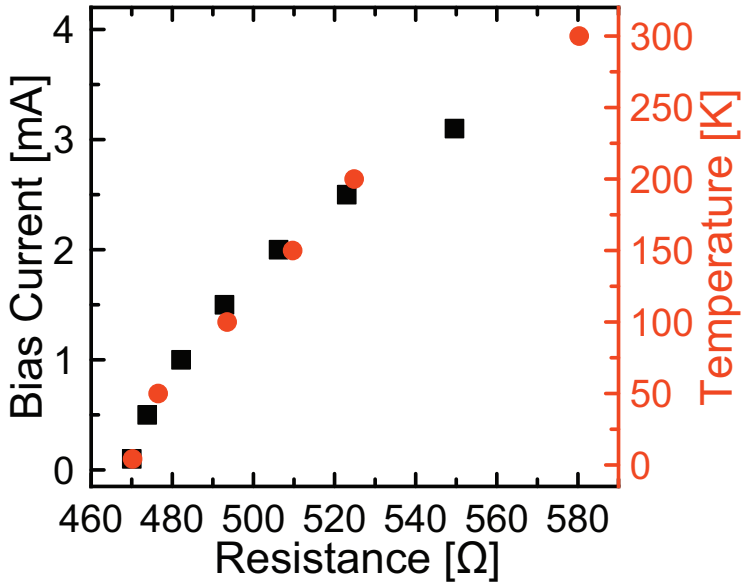

Figure 4.10: **Determining sample temperature.** Resistance of the nanowire measured as a function of temperature at direct bias current $I_{dc} = 0.1$ mA (circles) and as a function of I_{dc} at the bath temperature $T_b = 4.2$ K (squares).

4.2.6 Sample Temperature

Direct current bias I_{dc} can significantly increase the temperature of the nanowire due to Ohmic heating. In order to estimate the actual temperature of the nanowire at large I_{dc}, measurements of the wire resistance as a function of temperature at small $I_{dc} = 0.1$ mA to measurements of the wire resistance versus I_{dc} taken at the bath temperature $T_b = 4.2$ K is compared[57]. This data is plotted in Fig. 4.10, which shows that resistance of the nanowire is approximately quadratic in both T_b and I_{dc}. This allows for an estimate of the actual temperature of the nanowire directly from Fig. 4.10. For example, at $I_{dc} = 2.0$ mA, the actual temperature of the nanowire $T \approx 150$ K.

4.2.7 Critical Current Density Estimate

In this section, the expected critical current density for excitation of self-oscillations of magnetization in the Pt/Py bilayer nanowire is estimated and compared to the experimentally

measured critical current density. The critical spin current density injected from the Pt layer into the Py layer J_S (measured in units of charge current density) is given by[69]:

$$J_S = \frac{2e}{\hbar}\alpha\left(H_{eff} + 2\pi M_{eff}\right) M_s t \tag{4.7}$$

where $H_{eff} \approx 600$ Oe is the in-plane effective field approximately equal to the hard-axis applied field minus the in-plane hard-axis saturation field, $M_{eff} = M_s - K_s/(2\pi M_s t) = 484$ emu/cm^3, $t = 5$ nm is the Py layer thickness, and $\alpha = 0.023$ is the Gilbert damping constant appropriate for a 5 nm thick Py layer interfaced on one side with a Pt layer[88]. Eq. (4.7) gives the expected critical spin current density $J_S = 7.7 \times 10^6$ A/cm^2. This value should be compared to the measured critical spin current density in the Pt/Py bilayer nanowire system. Using the thin-film resistivity values of Pt and Py layers (ρ_{Pt} =20 $\mu\Omega$ cm and ρ_{Py} =45 $\mu\Omega$ cm[69]) and taking into account that the critical charge current for excitation of magnetization self oscillations in the bilayer nanowire is approximately 2.2 mA, the critical charge current density in the Pt layer is calculated to be $J_C = 1.6 \times 10^8$ A/cm^2. The corresponding transverse critical spin current density can be estimated as $J_S \approx \theta_{SH} J_C$[69], where θ_{SH} is the spin Hall angle in Pt. Assuming $\theta_{SH} = 0.056$[69], the estimated critical spin current density is $J_S = 9.0 \times 10^6$ A/cm^2, which is similar to the value expected for this system.

It is also instructive to compare the estimated critical spin current density in the Pt/Py bilayer system to that measured in Py(5.5 nm)/Cu(20 nm)/Py(20 nm) spin valve nanopillars[89]. The critical charge current density measured in these nanopillar devices is $J_C = 1.75 \times 10^7$ A/cm^2. Assuming spin current polarization $P = 0.3$, the measured critical spin current density is $J_S = P \cdot J_C = 5.2 \times 10^6$ A/cm^2. This value is nearly one half of the critical spin current density measured for the Pt/Py nanowire system, which is consistent with the damping of the Py free layer in the nanopillar ($\alpha = 0.01$[89]) being approximately half of that in the Pt/Py system.

4.3 Discussion

Recent experiments[39] demonstrated that application of spatially uniform SO torques to an extended ferromagnetic film does not result in excitation of magnetic self-oscillations because the amplitudes of all spin wave modes of the film are limited by nonlinear magnon scattering processes. Therefore, this observation of self-oscillatory dynamics excited by SO torques in the entire 1.8 μm long active region of a ferromagnetic nanowire is surprising. Thi suggests that the quantization of the spin wave spectrum in the nanowire geometry reduces the number of available nonlinear magnon scattering channels and thereby enables excitation of self-oscillatory dynamics of the low-energy spin wave eigenmodes of the nanowire.

Fig. 4.4(c) shows the spin wave dispersion relation of a 5 nm thick Py film calculated for spin wave propagating parallel (backward volume spin waves, BVSW) and perpendicular (surface spin waves, SSW) to the in-plane magnetization vector[79]. Energy- and momentum-conserving four-magnon scattering processes from the uniform ($\mathbf{k} = 0$) mode into spin wave modes with a finite wave vector $\mathbf{k}_4$ are allowed for the BVSW but not for the SSW modes as schematically illustrated in Fig. 4.4(c). This nonlinear scattering channel is always present in the 2D film geometry and it contributes to the nonlinear damping of the uniform mode. When such a film is patterned into a nanowire aligned perpendicular to the magnetization direction, the BVSW mode spectrum becomes quantized and the energy-conserving four-magnon scattering channel becomes suppressed for a wire of width $w < \pi k_4^{-1}$. This example illustrates how a nonlinear scattering channel present in the 2D film geometry becomes suppressed in the 1D nanowire geometry. A number of other higher-order nonlinear scattering channels allowed by symmetry in the film are also suppressed in the nanowire due to breaking of translational invariance in the direction perpendicular to the nanowire axis.

Since multiple nonlinear magnon scattering processes responsible for limiting the amplitude of low-frequency spin wave modes are eliminated in the nanowire, ST excitation

of large-amplitude self-oscillatory spin wave modes may become possible above the critical current. At higher currents, SO torques increase the occupation numbers for all magnon modes, which results in (i) enhanced scattering in the remaining nonlinear channels and the associated decrease of the amplitude of self-oscillations seen in Fig. 4.3(c) and (ii) reduction of the saturation magnetization and the associated decrease of the self-oscillatory mode frequency with current seen in Fig. 4.2(c). The data in Fig. 4.4 showing decreasing self-oscillation amplitude with increasing temperature suggest that magnon-phonon scattering might also play a role in suppression of the self-oscillatory dynamics. Development of a detailed theory accounting for all magnon scattering channels in the nanowire in the presence of SO torques is required for quantitative explanation of the experimental data, and hopefully this work will stimulate the development of such a theory.

In conclusion, this chapter demonstrated that spatially uniform spin torques can excite self-oscillations of magnetization in a 1D ferromagnetic system – a Pt/Py bilayer nanowire. The self-oscillatory modes induced by spin torque in this system directly arise from the bulk and edge spin wave eigenmodes of the nanowire. The 1D nanowire geometry offers unique advantages for studies of magnetization dynamics driven by spin torques over the 2D extended thin film system, in which spatially uniform spin torque does not excite magnetization self-oscillations. This result suggests that the self-oscillatory dynamics in the nanowire geometry is enabled by geometric confinement of magnons that suppresses a number of nonlinear magnon scattering channels. This chapter demonstrates the feasibility of spin torque oscillators with the active region dimensions extended beyond the nanometer length scale.

4.4 Methods

4.4.1 Sample fabrication

All layers of the Pt(5 nm)/Py(5 nm)/AlO_x(4 nm)/(GaAs substrate) samples are deposited by magnetron sputtering at room temperature. The 6 μm long nanowires are defined via e-beam lithography and Ar plasma etching using e-beam evaporated Cr mask. The Au(35 nm)/Cr(7 nm) leads with a 1.8 μm gap between them defining the active region of the nanowire STO are made via e-beam lithography and e-beam evaporation of the Au/Cr bilayer followed lift-off. The fabrication process of the AlOx(2 nm)Py(5 nm)/Pt(5-7 nm)/(sapphire substrate) samples for the micro-BLS measurements starts with deposition of a 5 nm thick Pt layer onto a sapphire substrate at 550 °C, which results in growth of a continuous Pt film as verified by high resolution SEM and atomic force microscopy imaging. Then the nanowire is defined on top of the Pt film via e-beam lithography, brief Ar plasma cleaning immediately followed by *in situ* room temperature sputter deposition of a AlOx(3 nm)/Py(5 nm)/Pt(2 nm) trilayer, and lift-off. The Au(40 nm)/Cr(7 nm) leads are defined via e-beam lithography and e-beam evaporation of the Au/Cr bilayer followed by lift-off. As the final fabrication step, Ar plasma etching is used to remove the 5 nm thick bottom Pt layer everywhere but under the Py nanowire and the Au/Cr leads.

4.4.2 BLS measurements.

Micro-focus BLS measurements were performed at room temperature by focusing light produced by a continuous-wave single-frequency laser operating at a wavelength of 532 nm into a diffraction-limited spot. The light scattered from magnetic oscillations was analyzed by a six-pass Fabry-Perot interferometer TFP-1 (JRS Scientific Instruments, Switzerland) to

obtain information about the BLS intensity proportional to the square of the amplitude of the dynamic magnetization at the location of the probing spot.

Bibliography

[8] P M Braganca et al. "Nanoscale magnetic field detection using a spin torque oscillator". In: *Nanotechnology* 21.23 (2010), p. 235202. DOI: 10.1088/0957-4484/21/23/235202. URL: http://dx.doi.org/10.1088/0957-4484/21/23/235202.

[12] J.C. Slonczewski. "Current-driven excitation of magnetic multilayers". In: *Journal of Magnetism and Magnetic Materials* 159.1-2 (1996), pp. L1–L7. DOI: doi:10.1016/0304-8853(96)00062-5. URL: http://dx.doi.org/10.1016/0304-8853(96)00062-5.

[13] L. Berger. "Emission of spin waves by a magnetic multilayer traversed by a current". In: *Phys. Rev. B* 54.13 (1996), pp. 9353–9358. DOI: http://dx.doi.org/10.1103/PhysRevB.54.9353. URL: http://dx.doi.org/10.1103/PhysRevB.54.9353.

[16] D'yakonov M.I. and Perel' V. I. "Possibility of Orienting Electron Spins with Current". In: *Sov. Phys. JETP Lett.* 13.11 (1971), p. 467. URL: http://www.jetpletters.ac.ru/ps/1587/article_24366.pdf.

[17] J. E. Hirsch. "Spin Hall Effect". In: *Phys. Rev. Lett.* 83.9 (1999), pp. 1834–1837. DOI: http://dx.doi.org/10.1103/PhysRevLett.83.1834. URL: http://dx.doi.org/10.1103/PhysRevLett.83.1834.

[22] Axel Hoffmann. "Spin Hall Effects in Metals". In: *IEEE Trans. Magn.* 49.10 (2013), pp. 5172–5193. DOI: 10.1109/TMAG.2013.2262947. URL: http://dx.doi.org/10.1109/TMAG.2013.2262947.

[26] T. McGuire and R. Potter. "Anisotropic magnetoresistance in ferromagnetic 3d alloys". In: *IEEE Trans. Magn.* 11.4 (1975), pp. 1018–1038. DOI: 10.1109/TMAG.1975.1058782. URL: http://dx.doi.org/10.1109/TMAG.1975.1058782.

[34] M.J. Donahue and D.G. Porter. *OOMMF User's Guide, Version 1.0*. Interagency Report NISTIR 6376. Gaithersburg, MD: National Institute of Standards and Technology, 1999.

[36] A. A. Tulapurkar et al. "Spin-torque diode effect in magnetic tunnel junctions". In: *Nature* 438.7066 (2005), pp. 339–342. DOI: 10.1038/nature04207. URL: http://dx.doi.org/10.1038/nature04207.

[37] J. C. Sankey et al. "Spin-Transfer-Driven Ferromagnetic Resonance of Individual Nanomagnets". In: *Phys. Rev. Lett.* 96.22 (2006). DOI: http://dx.doi.org/10.1103/PhysRevLett.96.227601. URL: http://dx.doi.org/10.1103/PhysRevLett.96.227601.

[38] S. I. Kiselev et al. "Microwave oscillations of a nanomagnet driven by a spin-polarized current". In: *Nature* 425.6956 (2003), pp. 380–383. DOI: 10.1038/nature01967. URL: http://dx.doi.org/10.1038/nature01967.

[39] V. E. Demidov et al. "Control of Magnetic Fluctuations by Spin Current". In: *Phys. Rev. Lett.* 107.10 (2011). DOI: http://dx.doi.org/10.1103/PhysRevLett.107.107204. URL: http://dx.doi.org/10.1103/PhysRevLett.107.107204.

[40] Vladislav E. Demidov et al. "Magnetic nano-oscillator driven by pure spin current". In: *Nature Materials* (2012). DOI: 10.1038/nmat3459. URL: http://dx.doi.org/10.1038/nmat3459.

[41] Zheng Duan et al. "Nanowire spin torque oscillator driven by spin orbit torques". In: *Nature Communications* 5 (2014), p. 5616. DOI: doi:10.1038/ncomms6616. URL: http://dx.doi.org/10.1038/ncomms6616.

[45] A. Slavin and V. Tiberkevich. "Nonlinear Auto-Oscillator Theory of Microwave Generation by Spin-Polarized Current". In: *IEEE Trans. Magn.* 45.4 (2009), pp. 1875–1918. DOI: 10.1109/TMAG.2008.2009935. URL: http://dx.doi.org/10.1109/TMAG.2008.2009935.

[46] B. zyilmaz et al. "Current-Induced Excitations in Single Cobalt Ferromagnetic Layer Nanopillars". In: *Phys. Rev. Lett.* 93.17 (2004). DOI: http://dx.doi.org/10.1103/PhysRevLett.93.176604. URL: http://dx.doi.org/10.1103/PhysRevLett.93.176604.

[47] Q. Mistral et al. "Current-driven microwave oscillations in current perpendicular-to-plane spin-valve nanopillars". In: *Appl. Phys. Lett.* 88.19 (2006), p. 192507. DOI: http://dx.doi.org/10.1063/1.2201897. URL: http://dx.doi.org/10.1063/1.2201897.

[48] W. Rippard et al. "Direct-Current Induced Dynamics in C o 90 F e 10 / N i 80 F e 20 Point Contacts". In: *Phys. Rev. Lett.* 92.2 (2004). DOI: 10.1103/PhysRevLett.92.027201. URL: http://dx.doi.org/10.1103/PhysRevLett.92.027201.

[49] A. Ruotolo et al. "Phase-locking of magnetic vortices mediated by antivortices". In: *Nature Nanotech* 4.8 (2009), pp. 528–532. DOI: 10.1038/nnano.2009.143. URL: http://dx.doi.org/10.1038/nnano.2009.143.

[50] S. M. Mohseni et al. "Spin Torque-Generated Magnetic Droplet Solitons". In: *Science* 339.6125 (2013), pp. 1295–1298. DOI: 10.1126/science.1230155. URL: http://dx.doi.org/10.1126/science.1230155.

[51] Alexey V. Nazarov et al. "Spin transfer stimulated microwave emission in MgO magnetic tunnel junctions". In: *Appl. Phys. Lett.* 88.16 (2006), p. 162504. DOI: http://dx.doi.org/10.1063/1.2196232. URL: http://dx.doi.org/10.1063/1.2196232.

[52] Alina M. Deac et al. "Bias-driven high-power microwave emission from MgO-based tunnel magnetoresistance devices". In: *Nat Phys* 4.10 (2008), pp. 803–809. DOI: 10.1038/nphys1036. URL: http://dx.doi.org/10.1038/nphys1036.

[53] D. Houssameddine et al. "Spin transfer induced coherent microwave emission with large power from nanoscale MgO tunnel junctions". In: *Appl. Phys. Lett.* 93.2 (2008), p. 022505. DOI: http://dx.doi.org/10.1063/1.2956418. URL: http://dx.doi.org/10.1063/1.2956418.

[54] B. Georges et al. "Origin of the spectral linewidth in nonlinear spin-transfer oscillators based on MgO tunnel junctions". In: *Phys. Rev. B* 80.6 (2009). DOI: http://dx.doi.org/10.1103/PhysRevB.80.060404. URL: http://dx.doi.org/10.1103/PhysRevB.80.060404.

[55] Graham E. Rowlands et al. "Time Domain Mapping of Spin Torque Oscillator Effective Energy". In: *Phys. Rev. Lett.* 111.8 (2013). DOI: http://dx.doi.org/10.1103/PhysRevLett.111.087206. URL: http://dx.doi.org/10.1103/PhysRevLett.111.087206.

[56] Luqiao Liu et al. "Magnetic Oscillations Driven by the Spin Hall Effect in 3-Terminal Magnetic Tunnel Junction Devices". In: *Phys. Rev. Lett.* 109.18 (2012). DOI: http://dx.doi.org/10.1103/PhysRevLett.109.186602. URL: http://dx.doi.org/10.1103/PhysRevLett.109.186602.

[57] R. H. Liu, W. L. Lim, and S. Urazhdin. "Spectral Characteristics of the Microwave Emission by the Spin Hall Nano-Oscillator". In: *Phys. Rev. Lett.* 110.14 (2013). DOI: http://dx.doi.org/10.1103/PhysRevLett.110.147601. URL: http://dx.doi.org/10.1103/PhysRevLett.110.147601.

[58] Paul M. Haney et al. "Current induced torques and interfacial spin-orbit coupling: Semiclassical modeling". In: *Phys. Rev. B* 87.17 (2013). DOI: http://dx.doi.org/10.1103/PhysRevB.87.174411. URL: http://dx.doi.org/10.1103/PhysRevB.87.174411.

[59] Junyeon Kim et al. "Layer thickness dependence of the current-induced effective field vector in Ta|CoFeB|MgO". In: *Nature Materials* 12.3 (2012), pp. 240–245. DOI: 10.1038/nmat3522. URL: http://dx.doi.org/10.1038/nmat3522.

[60] Eduardo Martinez, Satoru Emori, and Geoffrey S. D. Beach. "Current-driven domain wall motion along high perpendicular anisotropy multilayers: The role of the Rashba field, the spin Hall effect, and the Dzyaloshinskii-Moriya interaction". In: *Appl. Phys. Lett.* 103.7 (2013), p. 072406. DOI: http://dx.doi.org/10.1063/1.4818723. URL: http://dx.doi.org/10.1063/1.4818723.

[61] Shufeng Zhang. "Spin Hall Effect in the Presence of Spin Diffusion". In: *Phys. Rev. Lett.* 85.2 (2000), pp. 393–396. DOI: http://dx.doi.org/10.1103/PhysRevLett.85.393. URL: http://dx.doi.org/10.1103/PhysRevLett.85.393.

[62] K. Ando et al. "Electric Manipulation of Spin Relaxation Using the Spin Hall Effect". In: *Phys. Rev. Lett.* 101.3 (2008). DOI: http://dx.doi.org/10.1103/PhysRevLett.101.036601. URL: http://dx.doi.org/10.1103/PhysRevLett.101.036601.

[63] Xin Fan et al. “Observation of the nonlocal spin-orbital effective field”. In: *Nature Communications* 4 (2013), p. 1799. DOI: 10.1038/ncomms2709. URL: http://dx.doi.org/10.1038/ncomms2709.

[64] Lihui Bai et al. “Universal Method for Separating Spin Pumping from Spin Rectification Voltage of Ferromagnetic Resonance”. In: *Phys. Rev. Lett.* 111.21 (2013). DOI: http://dx.doi.org/10.1103/PhysRevLett.111.217602. URL: http://dx.doi.org/10.1103/PhysRevLett.111.217602.

[65] Rashba E. I. Bychkov Yu. A. “Properties of a 2D electron gas with lifted spectral degeneracy”. In: *JETP Lett.* 39 (1984), p. 66. URL: http://www.jetpletters.ac.ru/ps/1264/article_19121.shtml.

[66] Jairo Sinova et al. “Universal Intrinsic Spin Hall Effect”. In: *Phys. Rev. Lett.* 92.12 (2004). DOI: http://dx.doi.org/10.1103/PhysRevLett.92.126603. URL: http://dx.doi.org/10.1103/PhysRevLett.92.126603.

[67] Katsunori Obata and Gen Tatara. “Current-induced domain wall motion in Rashba spin-orbit system”. In: *Phys. Rev. B* 77.21 (2008). DOI: 10.1103/PhysRevB.77.214429. URL: http://dx.doi.org/10.1103/PhysRevB.77.214429.

[68] Ioan Mihai Miron et al. “Current-driven spin torque induced by the Rashba effect in a ferromagnetic metal layer”. In: *Nature Materials* (2010). DOI: 10.1038/nmat2613. URL: http://dx.doi.org/10.1038/nmat2613.

[69] Luqiao Liu et al. “Spin-Torque Ferromagnetic Resonance Induced by the Spin Hall Effect”. In: *Phys. Rev. Lett.* 106.3 (2011). DOI: http://dx.doi.org/10.1103/PhysRevLett.106.036601. URL: http://dx.doi.org/10.1103/PhysRevLett.106.036601.

[70] C. Wang et al. “Bias and angular dependence of spin-transfer torque in magnetic tunnel junctions”. In: *Phys. Rev. B* 79.22 (2009). DOI: http://dx.doi.org/10.1103/PhysRevB.79.224416. URL: http://dx.doi.org/10.1103/PhysRevB.79.224416.

[71] N. Mecking, Y. S. Gui, and C.-M. Hu. “Microwave photovoltage and photoresistance effects in ferromagnetic microstrips”. In: *Phys. Rev. B* 76.22 (2007). DOI: http://dx.doi.org/10.1103/PhysRevB.76.224430. URL: http://dx.doi.org/10.1103/PhysRevB.76.224430.

[72] Andrei Slavin and Vasil Tiberkevich. “Spin Wave Mode Excited by Spin-Polarized Current in a Magnetic Nanocontact is a Standing Self-Localized Wave Bullet”. In: *Phys. Rev. Lett.* 95.23 (2005). DOI: 10.1103/PhysRevLett.95.237201. URL: http://dx.doi.org/10.1103/PhysRevLett.95.237201.

[73] C. Bayer et al. “Spin-wave excitations in finite rectangular elements of Ni 80 Fe 20”. In: *Phys. Rev. B* 72.6 (2005). DOI: http://dx.doi.org/10.1103/PhysRevB.72.064427. URL: http://dx.doi.org/10.1103/PhysRevB.72.064427.

[74] J. P. Park et al. “Spatially Resolved Dynamics of Localized Spin-Wave Modes in Ferromagnetic Wires”. In: *Phys. Rev. Lett.* 89.27 (2002). DOI: 10.1103/PhysRevLett.89.277201. URL: http://dx.doi.org/10.1103/PhysRevLett.89.277201.

[75] R. D. McMichael and B. B. Maranville. "Edge saturation fields and dynamic edge modes in ideal and nonideal magnetic film edges". In: *Phys. Rev. B* 74.2 (2006). DOI: http://dx.doi.org/10.1103/PhysRevB.74.024424. URL: http://dx.doi.org/10.1103/PhysRevB.74.024424.

[76] I. N. Krivorotov et al. "Temperature Dependence of Spin-Transfer-Induced Switching of Nanomagnets". In: *Phys. Rev. Lett.* 93.16 (2004). DOI: http://dx.doi.org/10.1103/PhysRevLett.93.166603. URL: http://dx.doi.org/10.1103/PhysRevLett.93.166603.

[77] James O. Rantschler et al. "Surface anisotropy of permalloy in NMNiFeNM multilayers". In: *J. Appl. Phys.* 97.10 (2005), 10J113. DOI: http://dx.doi.org/10.1063/1.1853711. URL: http://dx.doi.org/10.1063/1.1853711.

[78] Hans T. Nembach et al. "Mode- and Size-Dependent Landau-Lifshitz Damping in Magnetic Nanostructures: Evidence for Nonlocal Damping". In: *Phys. Rev. Lett.* 110.11 (2013). DOI: http://dx.doi.org/10.1103/PhysRevLett.110.117201. URL: http://dx.doi.org/10.1103/PhysRevLett.110.117201.

[79] R. E. De Wames. "Dipole-Exchange Spin Waves in Ferromagnetic Films". In: *J. Appl. Phys.* 41.3 (1970), p. 987. DOI: http://dx.doi.org/10.1063/1.1659049. URL: http://dx.doi.org/10.1063/1.1659049.

[80] S.O. Demokritov and V.E. Demidov. "Micro-Brillouin Light Scattering Spectroscopy of Magnetic Nanostructures". In: *IEEE Trans. Magn.* 44.1 (2008), pp. 6–12. DOI: 10.1109/TMAG.2007.910227. URL: http://dx.doi.org/10.1109/TMAG.2007.910227.

[81] Henning Ulrichs et al. "Parametric excitation of eigenmodes in microscopic magnetic dots". In: *Phys. Rev. B* 84.9 (2011). DOI: http://dx.doi.org/10.1103/PhysRevB.84.094401. URL: http://dx.doi.org/10.1103/PhysRevB.84.094401.

[82] Philippe Djemia, François Ganot, and Philippe Moch. "Brillouin scattering in ultrathin permalloy films: monolayers and multilayers with alumina interfaces". In: *Journal of Magnetism and Magnetic Materials* 165.1-3 (1997), pp. 428–430. DOI: http://dx.doi.org/10.1016/S0304-8853(96)00577-X. URL: http://dx.doi.org/10.1016/S0304-8853(96)00577-X.

[83] A.Z. Maksymowicz et al. "Exchange constant and surface pinning in single permalloy films". In: *Thin Solid Films* 197.1-2 (1991), pp. 287–292. DOI: 10.1016/0040-6090(91)90239-T. URL: http://dx.doi.org/10.1016/0040-6090(91)90239-T.

[84] Neil Smith, David Markham, and David LaTourette. "Magnetoresistive measurement of the exchange constant in varied-thickness permalloy films". In: *J. Appl. Phys.* 65.11 (1989), p. 4362. DOI: http://dx.doi.org/10.1063/1.343273. URL: http://dx.doi.org/10.1063/1.343273.

[85] A. Helmer et al. "Quantized spin-wave modes in magnetic tunnel junction nanopillars". In: *Phys. Rev. B* 81.9 (2010). DOI: http://dx.doi.org/10.1103/PhysRevB.81.094416. URL: http://dx.doi.org/10.1103/PhysRevB.81.094416.

[86] J. P. Nibarger et al. “Variation of magnetization and the Lande g factor with thickness in Ni–Fe films”. In: *Appl. Phys. Lett.* 83.1 (2003), p. 93. DOI: http://dx.doi.org/10.1063/1.1588734. URL: http://dx.doi.org/10.1063/1.1588734.

[87] G. Venkat et al. “Proposal for a Standard Micromagnetic Problem: Spin Wave Dispersion in a Magnonic Waveguide”. In: *IEEE Trans. Magn.* 49.1 (2013), pp. 524–529. DOI: 10.1109/TMAG.2012.2206820. URL: http://dx.doi.org/10.1109/TMAG.2012.2206820.

[88] S Mizukami, Y Ando, and T Miyazaki. “Ferromagnetic resonance linewidth for NM/80NiFe/NM films (NM=Cu, Ta, Pd and Pt)”. In: *Journal of Magnetism and Magnetic Materials* 226-230 (2001), pp. 1640–1642. DOI: http://dx.doi.org/10.1016/S0304-8853(00)01097-0. URL: http://dx.doi.org/10.1016/S0304-8853(00)01097-0.

[89] G. D. Fuchs et al. “Spin-torque ferromagnetic resonance measurements of damping in nanomagnets”. In: *Appl. Phys. Lett.* 91.6 (2007), p. 062507. DOI: http://dx.doi.org/10.1063/1.2768000. URL: http://dx.doi.org/10.1063/1.2768000.

Chapter 5

Dimensional crossover of nanowire spin Hall oscillator

Auto-oscillations of magnetization driven by direct spin current have been experimentally realized in quasi-zero-dimensional (0D) systems such as nanomagnets and nanocontacts. Recently, it has been shown that spin current can excite coherent auto-oscillatory dynamics in quasi-one-dimensional (1D) ferromagnetic nanowires but not in quasi-two-dimensional (2D) ferromagnetic films. Here we study the 1D to 2D dimensional crossover of current-driven magnetization dynamics in wire-based NiFe/Pt spin Hall oscillators via varying the wire width. We observe that increasing the wire width results in an increase of the number of excited modes accompanied by a decrease of the amplitude and coherence of each of the modes. We also observe a crossover from a hard to a soft onset of the auto-oscillations with increasing the wire width. The amplitude of auto-oscillations rapidly decreases with increasing temperature suggesting that interactions of the auto-oscillatory modes with thermal magnons plays important role in suppression of the auto-oscillations. Our measurements set the upper limit on the dimensions of spin torque oscillators and elucidate the mechanisms leading to suppression of coherent auto-oscillations with increasing auto-oscillator size.

5.1 Introduction

Spin current injected into a ferromagnet applies spin torque (ST) to its magnetization that can act as effective negative magnetic damping[12,13]. At a critical spin current density, the effective negative damping from spin torque overcomes the positive natural magnetic damping of the ferromagnet, which can result in the excitation of persistent auto-oscillatory dynamics of magnetization in the GHz frequency range[38,45]. Devices based on such auto-oscillatory dynamics called spin torque oscillators (STOs) are under consideration as tunable sources of microwave radiation[38,48,90] and spin wave generators for nanomagnonic applications[91–96].

Most STOs studied up to date are effectively zero-dimensional (0D) with the active region where the self-oscillatory dynamics are excited being restricted to the nanometer length scale in all three spatial dimensions. Examples of such oscillators include (i) nanopillar spin valves[8,38,46,47] and magnetic tunnel junctions[51–55], (ii) point contact to magnetic multilayers[48–50] and planar point contact STOs[40,57]. It was recently demonstrated that effectively one-dimensional (1D) oscillators can be realized in ferromagnetic nanowires where several low frequency spin wave eigenmodes are simultaneously driven into large-amplitude auto-oscillations by pure spin Hall current[41]. In contrast to the 0D and 1D geometries, STOs with effectively two-dimensional (2D) active region cannot be realized[39]. It was shown that spatially uniform injection of spin current into a ferromagnetic film does not result in excitation of large-amplitude coherent auto-oscillations. It was proposed that such suppression of auto-oscillatory dynamics in the 2D case results from nonlinear coupling among the continuum of spin wave modes in the film geometry[39]. As a result of such coupling, an increase of the amplitude of any spin wave mode leads to enhanced scattering of this mode into other spin wave modes, which prevents any single mode from reaching large amplitude.

In this chapter, we experimentally investigate the crossover between the 1D and 2D STO geometries in order to elucidate the mechanisms responsible for suppression of co-

herent self-oscillatory dynamics in the 2D geometry. The current-driven dynamics is studied in STOs made from bilayers of platinum and Permalloy (Py = $Ni_{80}Fe_{20}$) where anti-damping spin Hall current generated in Pt is injected into the Py layer. The 1D to 2D crossover is realized via varying the wire width from the nanometer- to the micrometer-scale dimensions. Quite surprisingly, we find that there is an optimal wire width that maximizes the amplitude and coherence of the auto-oscillatory dynamics. Our measurements reveal that the number of auto-oscillatory modes increases with increasing the wire width beyond the optimal while their amplitude and coherence both decrease. We find that the transition between large-amplitude coherent auto-oscillatory dynamics in the 1D geometry and small-amplitude incoherent dynamics in the 2D geometry is a continuous crossover. We also report measurements of the auto-oscillatory dynamics as a function of temperature, and observe a rapid decrease of the amplitude of auto-oscillations with increasing temperature, which points to the important role of scattering of the auto-oscillatory modes on thermal magnons in limiting the amplitude and coherence of the auto-oscillatory modes.

5.2 Py/Pt wire fabrication and characterization

The Py/Pt wire samples are patterned using e-beam lithography and ion milling from a (c-plane sapphire substrate)/Pt(6 nm)/Py(5 nm)/Al_2O_3(2 nm) multilayer grown by magnetron sputtering. Py/Pt wire samples of five different widths: 0.17, 0.35, 0.53, 1.07 and 2.11 μm the and the length of 40 μm are studied. Two Ti(10 nm)/Au(40 nm) leads for application of electric current bias to the middle section of the wire between the leads are patterned atop the wire as shown in Fig. 5.1(a) and (b). The 1.9 μm long middle section of the Py/Pt wire between the leads defines the active region of the nanowire, where the electric current and the spin Hall current densities are much higher than those under the leads.

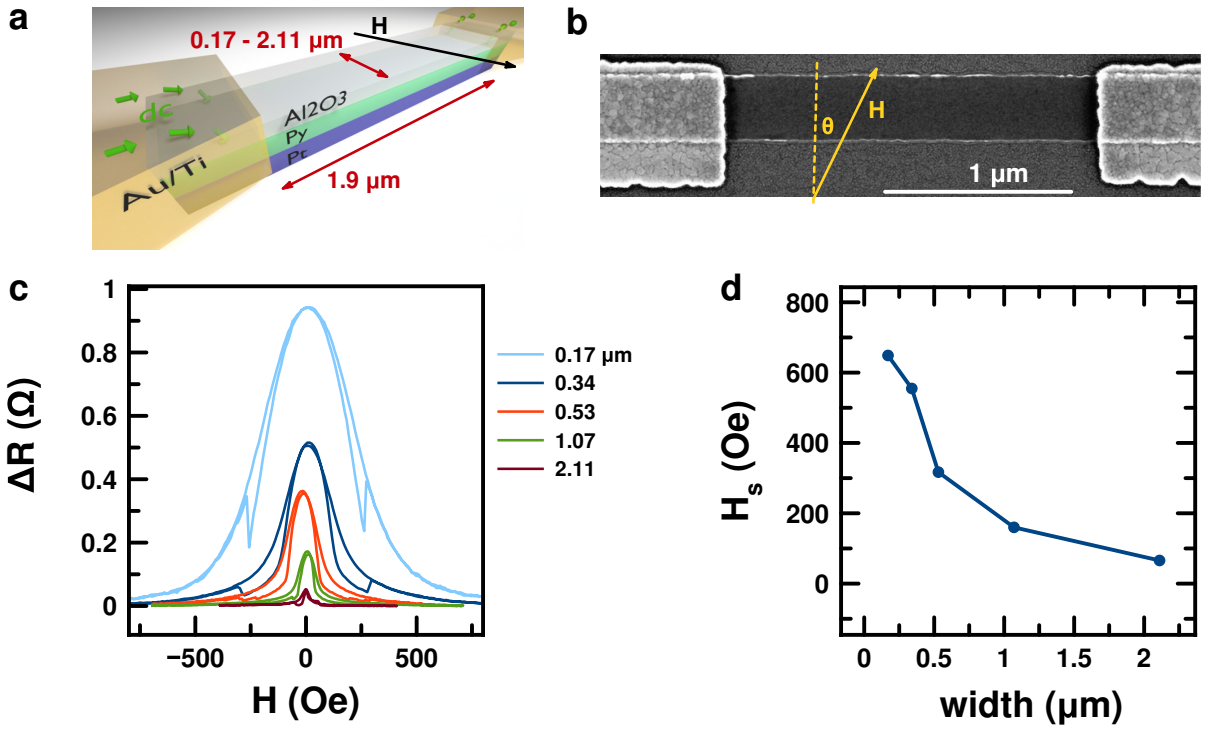

Figure 5.1: **Sample structure.** **(a)** Schematic of an Al_2O_3/Py/Pt nanowire STO device: width varies from 0.17 to 2.11 microns while active region is fixed at 1.9 microns with external magnetic field shown as black arrow and electric current as green arrows. **(b)** Scanning electron micrograph of an Al_2O_3/Py/Pt nanowire STO where the nanowire is the black stripe, bright areas are the Au/Ti leads, and yellow arrow is the external magnetic field direction. Scale bar, 1 micron. **(c)** Magneto-resistance verses in-plane magnetic field applied at $\theta = 5^o$ measured at the bath temperature $T_{bath} = 4.2$ K and low bias current densities for each different width of nanowire. **(d)** Saturation field, defined as when the magneto-resistance reaches 5% of its maxium value, as a function of the wire width.

When electric current bias is applied to the wire, the current flowing in the Pt layer generates pure spin Hall current that flows perpendicular to the sample plane and is injected into the Py layer as schematically shown in Fig. 5.1(a). The spin polarization of this spin current is perpendicular to the directions of both the spin current and the electrical current. When the wire is magnetized in the plane of the sample perpendicular to the wire axis ($\theta = 0^\circ$ as illustrated in Fig. 5.1(b)), ST from the pure spin current acts as effective negative magnetic damping that can excite auto-oscillatory dynamics of the Py magnetization.

Fig. 5.1(c) shows magneto-resistance (MR) of all five samples measured as small bias current at bath temperature $T = 4.2$ K as a function of magnetic field H applied in the sample plane nearly perpendicular to the wire direction ($\theta = 5^\circ$). The observed MR signal arises from anisotropic magneto-resistance (AMR) of Py, for which resistance R of the sample is at maximum R_{max} when magnetization is parallel to the electric current direction and is at minimum R_{min} when magnetization is perpendicular to the electric current. The magnitude of the AMR signal $\Delta R_{AMR} = R_{max} - R_{min}$ decreases with increasing width of the wire because of the decreasing wire resistance. By fitting the resistance of the device verses the width of the wire, the sheet resistivity of the nanowire is found to be $\rho_{wire} \approx 10\ \mu\Omega * cm$ while the lead resistance is 32 Ω for the 2 widest wires and 44 Ω for the 3 narrowest wires. The difference in the lead resistance is due to the 2 different lead patterns used. The saturation field of the Py wire H_s magnetization can be determined from the AMR data in Fig. 5.1(c). Fig. 5.1(d) shows the dependence of H_s defined as resistance value for which $R = R_{min} + 0.05\Delta R_{AMR}$ on the wire width w. The saturation field increases with decreasing wire width due to enhanced demagnetization field in narrower wires[97]. All measurements of the microwave signal generation by the Py/Pt samples described in this paper are made at a field that exceeds $H_s(w)$ shown in Fig. 5.1(d) by 100 Oe.

5.3 Microwave Emission Measurements

Fig. 5.2 shows spectral properties of the microwave signals generated by the Pt/Pt wire devices and measured with a microwave spectrum analyzer as a function of bias current density J_{dc} applied to the wire at the sample bath temperature of 4.2 K and $\theta = 5°$. Fig. 5.2(a) shows a typical spectrum measured for the 1.07 μm wide wire device at $J_{dc} = 2.0 \times 10^8$ A/cm^2, and $H = 470$ Oe. the spectra typically show multiple peaks, which demonstrates that several spin wave modes of the devices simultaneously enter the auto-oscillatory state. Note that quantitative analysis of the spectral linewidth and line shape of these peaks is complicated by the presence of standing waves in the microwave circuitry, which manifest themselves as oscillatory modulation of the spectral peak amplitude near 5.3 GHz.

Fig. 5.2(b-f) show the microwave emission of the five Py/Pt wire devices with different wire widths as a function of J_{dc}. For the 0.17 μm wire (Fig. 5.2(b)), a single low-frequency mode is observed. The frequency of this mode first increases and then decreases with current and the spectral linewidth of this mode is large. Previous studies of the Py/Pt nanowire STOs revealed that this low frequency mode is the edge mode (EM), which amplitude is maximum at the wire edge. The large spectral linewidth of this mode most likely stems from geometric roughness of the wire edge and magnetic material inhomogeneities caused by ion mill damage and oxidation of the edge.

For the 0.34 μm wire (Fig. 5.2(c)), the EM is present as well but it generates lower power than that in the 0.17 μm wire. This can be explained by the smaller volume fraction occupied by the edge mode in the 0.34 μm wire, and does not imply that the amplitude of the EM in the wider wire is less than that in the narrower wire. In addition to the EM, two high frequency auto-oscillatory modes are excited in the 0.34 μm wire. These high frequency modes with narrow spectral linewidths have been previously identified as bulk spin wave modes (BM), which amplitude is maximum near the center of the wire[41]. The splitting of

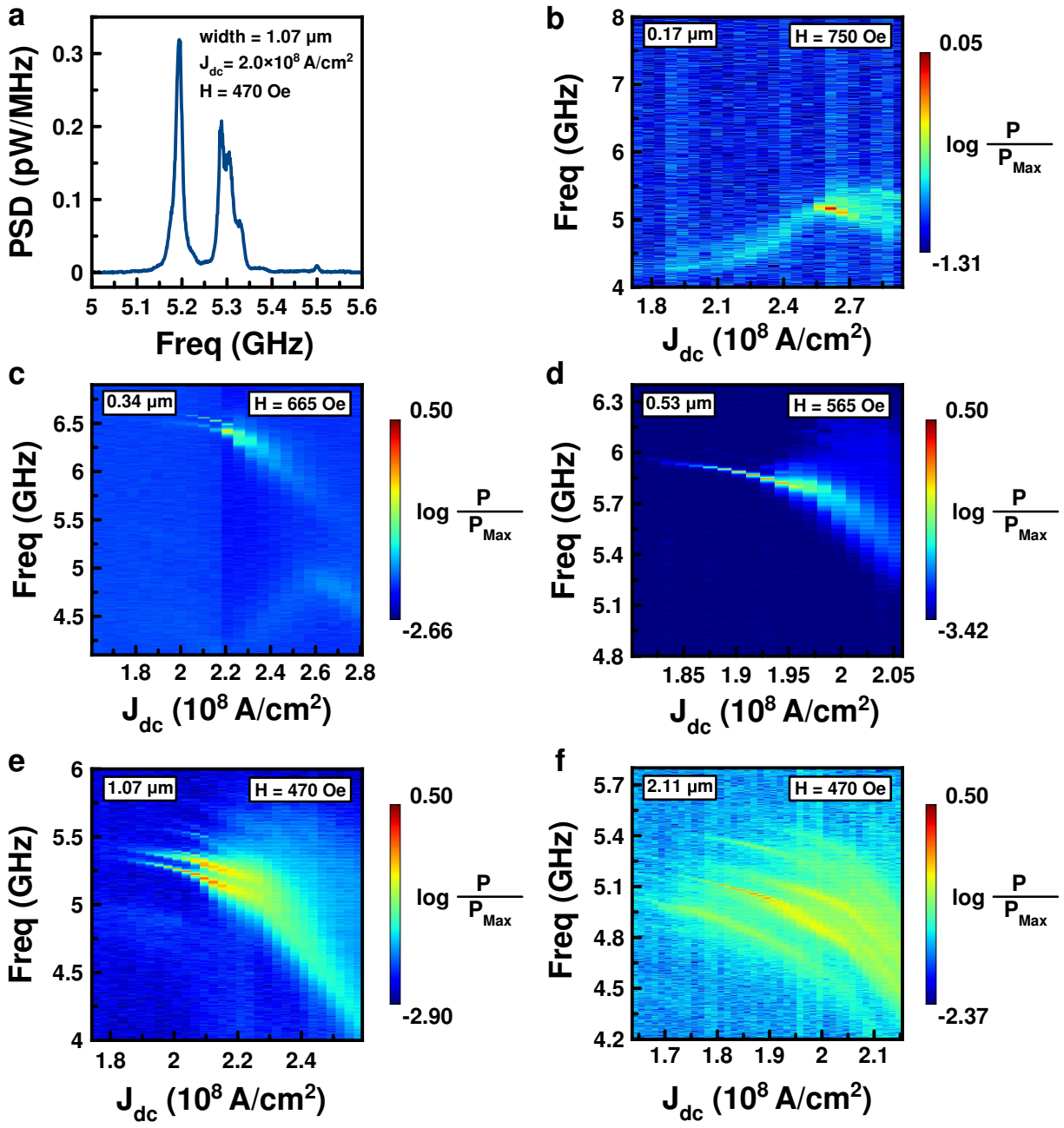

Figure 5.2: **Microwave emission spectra.** **(a)** Example power spectral density (PSD) of the microwave signal emitted by the 1.07 μm wide Al_2O_3/Py/Pt nanowire at bias current density $J_{dc} = 2.0 \times 10^8$ A/cm^2, bath temperature $T_{bath} = 4.2$ K and magnetic field H = 470 Oe applied at an angle of $\theta = 5^o$ where multiple spin wave eigenmodes modes are excited. The non-Lorentzian lineshape is due to standing waves in the microwave circuit. Dependence of the emission spectrum on J_{dc} for **(b)** width = 0.17 μm and H = 750 Oe, **(c)** width = 0.34 μm and H = 665 Oe, **(d)** width = 0.53 μm and H = 565 Oe, **(e)** width = 1.07 μm and H = 470 Oe and **(f)** width = 2.11 μm and H = 470 Oe. Edge spin wave eigen modes are detected for the 0.17 μm wire, edge and bulk-like modes for the 0.34 μm wire, and only bulk-like for the 0.53, 1.07 and 2.11 μm wires.

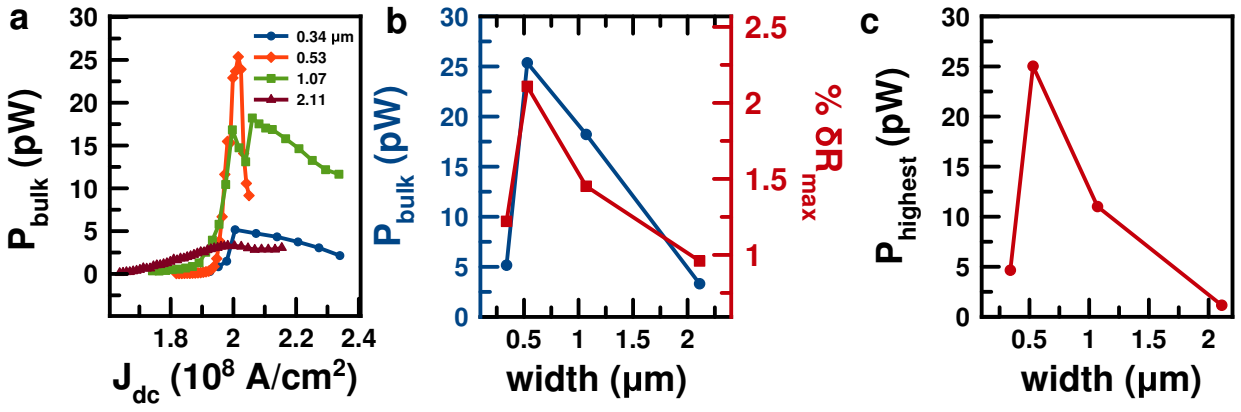

Figure 5.3: **Integrated power of microwave emission.** **(a)** Integrated power of the emission spectra of all of the bulk modes for each width of the wire as a function of bias current density J_{dc}. Maximum integrated power of the emission spectra for the **(b)**(blue circles) bulk modes and **(c)** single bulk mode as a function of the wire width. **(b)**(burgundy squares)The percentage of the maximum possible oscillatory resistance, defined as the oscillatory resistance calculated from the integrated power dividing by the AMR resistance, as a function of the wire width.

the bulk modes in two arises from geometric confinement of the modes to the 1.9 μm active region, which arises from the Oersted field due to electric current in the Pt layer and a step-wise change in effective magnetic damping at the boundaries between the active region and the electric leads.

For the 0.53 μm wire (Fig. 5.2(c)), the EM is no longer detected however this doesn't mean the EM is not excited, but could simply mean the volume ratio of the EM to the BM has decreased enough that the signal generated has decreased below the detection threshold. Multiple narrow bulk modes are detected again however, the lowest frequency bulk mode contains most of the power. Further increasing to 1.07 μm, additional BM are detected and the lowest frequency mode still still has the highest intensity. As the wire increases to 2.11 μm, even more BM are detected and interestingly, the highest intensity mode is no longer the lowest frequency.

The summation of the integrated power for all of the detected BM is shown in Fig. 5.3(a) as a function J_{dc} for each wire width except 0.17 μm. First, the onset of self-oscillations

becomes softer with increasing width. For the 0.34 μm wire, the increase of the integrated power from low power to its maximum occurs over 2×10^6 A/cm^2 while for the 0.53, 1.07, and 2.11 μm wires, the increases occurs over 7×10^6, 9×10^6, and 29×10^6 A/cm^2 respectfully. Second, after the integrated power reaches its maximum value, the power decreases gradually for all widths except the 0.53 μm wire. The maximum integrated power each wire reaches for all of the BM summed together and of the dominate BM is shown in Fig. 5.3(b) and (c) respectfully. The integrated power dramatically increases as the width increases from 0.34 to 0.53 μm but then steadily declines as the width increases. Additionally, as the width of the wire increases, the integrated power becomes more evenly shared between all detected modes.

The percentage of the maximum possible oscillatory resistance δR_{max}, defined as the oscillatory resistance calculated from the integrated power dividing by the AMR resistance for each wire, as a function of the wire width is shown in Fig. 5.3(b)(burgundy squares). The importance of this value is that it depends only on the amplitude of the magnetization oscillations, spatial profile of the excited modes, and the angle of the magnetic field (same for all wire widths) therefore it allows for a more direct comparison than integrated power. The same trend is found however, δR_{max} is found to be of similar magnitude for the 0.34 and 1.07 μm wires even though the integrated power is $\sim$4 times larger for the 1.07 μm wire. This can be explained by the fact that the BMs occupy a greater percentage of volume of the wire as the wire width increases thus resulting in an increase of δR_{max}. However, as the wire keeps increasing, the magnetization oscillation amplitude decreases due to increased magnon scattering and sharing of the angular momentum supplied by the spin torque thus resulting in a decrease of δR_{max}.

5.4 Micromagnetic Simulation

In order to identify the exact type of spin wave modes being excited, micromagnetic simulations of a 3 x 1.07 μm wire were carried out using MuMax3[98] with periodic boundary conditions along the length and at T_{bath}=0 K. The nanowire was split into 512 $\times$ 256 $\times$ 1 cells with a saturation magnetization of 620 emu/cm^3, exchange energy of 5×10^{-12} J/m^3, spin Hall angle of 7%, and damping constant of 0.006 which were determined previously[41]. An Oersted field of 112 Oe at 3.3×10^7 A/cm^2 is applied in the active region of the wire that scales linearily with J_{dc} which opposes the applied magnetic field (H=470 Oe, $\theta = 5^o$). This value for the Oersted field was estimated from the shift of the center of the AMR curve as seen in Fig. 5.1(c) for large positve and negative J_{dc} and scaled such that the Oersted field is the same at the critical bias current density J_c for both experiment and simulation.

The micromagnetically simulation emission spectra for the 1.07 μm wire at $J_{dc} = 3.5 \times 10^7$ A/cm^2 which is just above the simulated J_c is shown in Fig. 5.4(a). Here, m_x is the normalized magnetization component along the length of the wire (current direction). There are three main modes excited and their spatial profiles are shown in the top row of Fig. 5.4(c). Notably, all of the modes are only excited within the active region of the wire due to the presence of the Oersted field. If the Oersted field is removed in the micromagnetic simulation, the spin waves spill out of the active region which means that the spin wave well effect is the dominate cause of the localization of the spin waves rather than location of the source of the spin torque. Additionally, the asymmetry of the modes is due to the tilt of the applied magnetic field. Unsurprisingly, the lowest frequency mode is an EM, however, it is not the lowest order edge mode, but rather has a node along the length at the middle of the wire. The second mode excited is a BM that has 2 nodes along the width of the wire and no nodes along the length. Interestly, the highest frequency mode is no longer a linear combination of width and length modes, but rather a collection of anti-nodes along the perimeter of an oval.

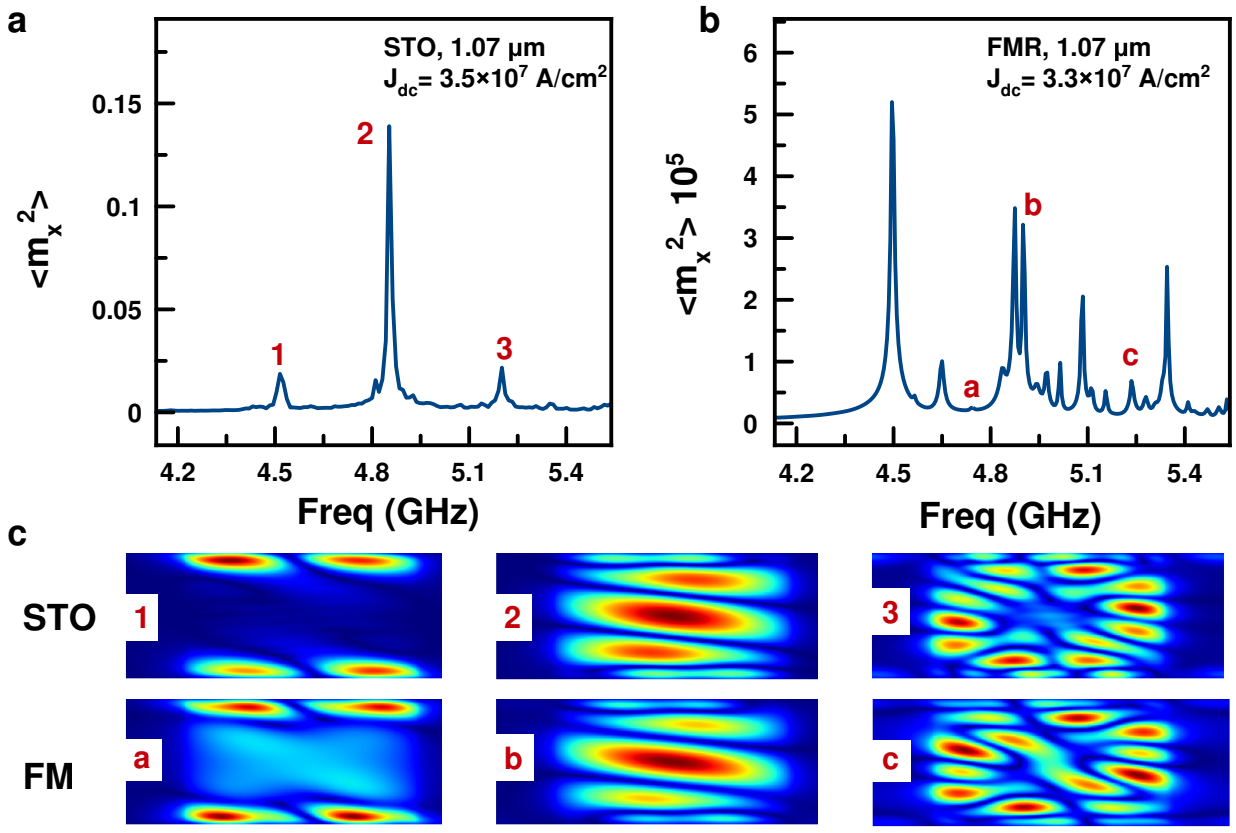

Figure 5.4: **Micromagnetic spin wave mode profiles for 1.07 μm wire.** **(a)** Micromagnetically calculated emission spectra of 1.07 μm wire at the critical bias current density $J_{dc} = 3.5 \times 10^7\ A/cm^2$, H = 470 Oe and $\theta = 5^o$. **(b)** Micromagnetically calculated spin torque ferromagnetic resonance spectra of 1.07μm wire at just below the critical bias current density $J_{dc} = 3.3 \times 10^7\ A/cm^2$, H = 470 Oe and $\theta = 5^o$. **(c)** Spatial profiles of the excited modes excited in **(a)** (top row) and those same modes in **(b)** (bottom row).

In order to confirm that the modes excited by dc spin torque are actually spin wave eigenmodes of the wire, a ferromagnetic resonance simulation was performed shown in Fig. 5.4(b) at the same conditions as the emission STO simulation, however, with $J_{dc} = 3.3 \times 10^7\ A/cm^2$, which is just below J_c. A rf Oersted field with a sinc profile and a cutoff frequency of 20 GHz was applied to the active region collinear with the dc Oersted field was used to excite the spin wave modes in the linear regime. The same modes excited in the STO spectra are again found in the FMR spectra and shown in the bottom row of Fig. 5.4(c). Interestingly, the largest mode in the FMR spectra (lowest order edge mode) is not found in the STO spectra which might be the result of weak coupling between the dc spin torque and this mode. Additionally, of the excited modes in the STO spectra, the 2nd mode is largest in both the STO and FMR spectras while mode 1 increases in relative amplitude the most with the increases dc spin torque. This collaborates the idea that the dc spin torque couples more strongly with the higher order EM rather than the lowest order.

5.5 Brilluoin Light Scattering

The inability to directly match the micromagnetically calculated STO spectra to the experimental spectra due to the inconsistent frequency separations between the detected modes, Brilluoin light scattering measurements of the 1.07 μm wire were performed at a room temperature, a field strength of H = 865 Oe and at $\theta = 3^o$. The intensity spectra for $J_{dc} = 9.35 \times 10^7\ A/cm^2$, where the signal is the strongest, is shown in Fig. 5.5(a). A spectra was taken every 100 nm in a 2.2 $\times$ 1.6 μm area that encompassed the active area of the wire and then averaged. A single broad mode is only detected with a spatial profile shown in Fig. 5.5(b). This mode is very similar to mode 1 shown in Fig. 5.4(c) and is at the same frequency. This suggests that at least one EM is in fact excited in all of the nanowire widths, however it is undetectable by electrical means. Whether the absence of the BMs in

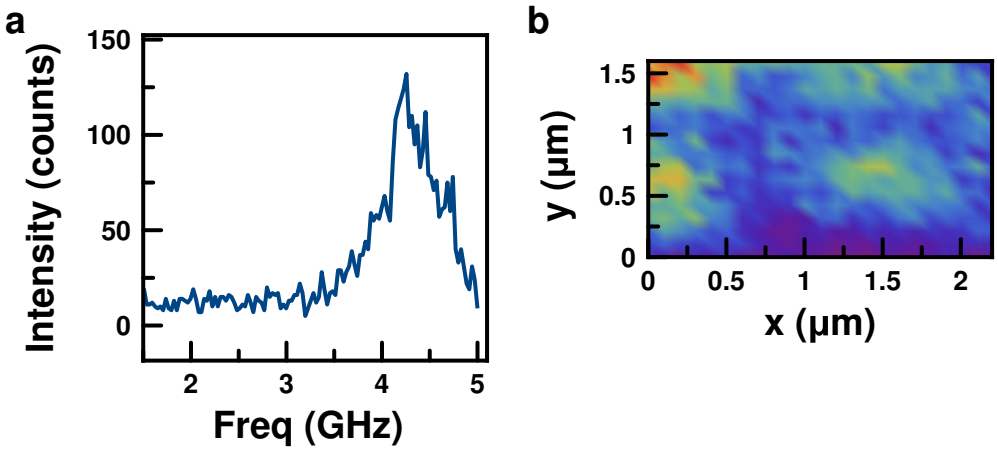

Figure 5.5: **BLS characterization of the auto-oscillating modes of the 1.07 μm wire. (a)** Averaged Brillouin light scattering signal over the active region of the 1.07 μm wire at $J_{dc} = 9.35 \times 10^7$ A/cm^2 and H=865 Oe applied at $\theta = 3^0$ and at a bath temperature T_{bath}= 293 K with a frequency step size of 30 MHz and an instrument resolution of 100 MHz. **(b)** Spatial profile of the magnetization intensity at the same conditions of **(a)** with the frequency fixed at f=3.43 GHz and a spatial step size of 100 nm.

the signal is due to them not being excited at room temperature or if they are only below the detection limits for the setup is unknown.

5.6 Discussion

Since the BMs are not detected at room temperature BLS measurements but are present at T_{bath}=4.2 K for the electrical measurements for the 1.07 μm suggests temperature might play an important role in the emission characteristics. To further explore this, J_c (blue circles) and the maximum integrated power (red squares) of all of the BM summed together is shown in Fig. 5.6(a) as a function of T_{bath} for H=750 Oe and $\theta = 5^o$ for the 0.53 μm wire. Both J_c and the integrated power decreases with increasing T_{bath} which is suggestive of thermal magnons increasing the population of the self-oscillatory states in the absence of spin torque. Therefore, the self-oscillatory states reach the threshold of auto-oscillations at a lower J_{dc}. Since thermal magnons also increase the population of the other spin wave states,

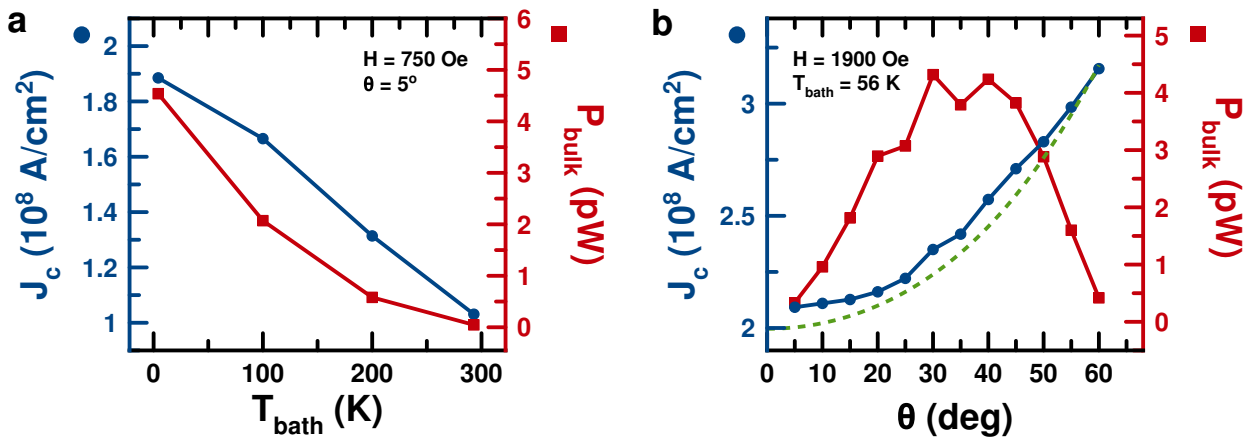

Figure 5.6: **Angular and temperature dependence of 0.53 μm wire.** **(a)** Critical bias current density (blue circles) and maximum integrated power (red squares) verse bath temperature with external magnetic field H = 750 Oe and at angle $\theta = 5^o$. **(b)** Critical bias current density (blue circles) and maximum integrated power (red squares) verse external magnetic field angle θ at bath temperature T_{bath} =56 K and magnetic field H = 1900 Oe for the 0.53 μm wire. The green dashed line is analytically calculated critical current density accounting for increased temperature of the sample due to Ohmic heating and angular dependence of the spin Hall effect.

the magnon scattering probability also increases. This then shifts energy out of the excited states to the sub-threshold states which results in reduced output power and higher effective damping. These factors result in the linear decrease of J_c and the exponential decrease of the integrated power.

In addition to T_{bath}, ohmic heating can also increase the temperature of the sample. Not only will this increase the number of thermal magnons, but it can also lead to an additional spin torque caused by the spin Seebeck effect (SSE) as seen in yttrium iron garnet (YIG)/Pt nanowires[99]. When dc current bias is applied to the sample, the Py will be hotter than the Pt which is in good thermal contact with the sapphire substate. This will then be an isotropic source of spin current that will always be anti-damping. In order to detect the presence of this effect, J_c (blue circles) is shown in Fig. 5.6(b) at T_{bath}=56 K and H=1900 Oe as a function of θ. Firstly, J_c is seen to have an angular dependence similar to 1/cos as expected for the spin Hall effect, however J_c is increasingly lower than expected at the larger angles. This can either be caused by the SSE or by other temperatures effects arising

from the increased ohmic heating for the higher J_c at higher angles. Therefore, an analytical calculation was performed taking into account the linear dependence of J_c on the sample temperature and the increased sample temperature due to ohmic heating which is shown as the green dashed line. Without including the SSE, the angular dependence is accurately predicited therefore it is unlikely the SEE is present in the sample.

The integrated power (red squares) of the bulk modes is also shown in Fig. 5.6(b) as a function of θ. Due to the cos^2 dependence on the angle between the magnetization and current direction for AMR, the maximum of integrated power is expected to occur at $\theta = 45^o$ and be minimum at 0 and 90^o. The integrated power does increase initially with increasing θ as expected, however, the integrated power saturates around $\theta = 30 - 40^o$ and then starts decreasing. Additionally, the integrated power at $\theta = 60^o$ approaches the same value at $\theta = 0^o$ instead of the expected 90^o. The likely distortion from the cos^2 dependence can again be attributed to the increased ohmic heating present at higher angles which decreases the integrated power.

5.7 Conclusions

This chapter has shown that the output power of a STO decreases as it approaches the 2-D case. With the addition that the output power decreases with increasing T_{bath}, this further supports the four magnon scattering theory. As either the number of spin wave modes increases (wider wires) or the population of all of the modes at zero dc bias current increases (higher sample temperatures), the probability of scattering magnons from the potentially excited states to sub-threshold states increases. Therefore, in order to have STO with high output powers over a large temperature range, modes other than the wanted excited mode need to be suppressed.

Bibliography

[8] P M Braganca et al. "Nanoscale magnetic field detection using a spin torque oscillator". In: *Nanotechnology* 21.23 (2010), p. 235202. DOI: 10.1088/0957-4484/21/23/235202. URL: http://dx.doi.org/10.1088/0957-4484/21/23/235202.

[12] J.C. Slonczewski. "Current-driven excitation of magnetic multilayers". In: *Journal of Magnetism and Magnetic Materials* 159.1-2 (1996), pp. L1–L7. DOI: doi:10.1016/0304-8853(96)00062-5. URL: http://dx.doi.org/10.1016/0304-8853(96)00062-5.

[13] L. Berger. "Emission of spin waves by a magnetic multilayer traversed by a current". In: *Phys. Rev. B* 54.13 (1996), pp. 9353–9358. DOI: http://dx.doi.org/10.1103/PhysRevB.54.9353. URL: http://dx.doi.org/10.1103/PhysRevB.54.9353.

[38] S. I. Kiselev et al. "Microwave oscillations of a nanomagnet driven by a spin-polarized current". In: *Nature* 425.6956 (2003), pp. 380–383. DOI: 10.1038/nature01967. URL: http://dx.doi.org/10.1038/nature01967.

[39] V. E. Demidov et al. "Control of Magnetic Fluctuations by Spin Current". In: *Phys. Rev. Lett.* 107.10 (2011). DOI: http://dx.doi.org/10.1103/PhysRevLett.107.107204. URL: http://dx.doi.org/10.1103/PhysRevLett.107.107204.

[40] Vladislav E. Demidov et al. "Magnetic nano-oscillator driven by pure spin current". In: *Nature Materials* (2012). DOI: 10.1038/nmat3459. URL: http://dx.doi.org/10.1038/nmat3459.

[41] Zheng Duan et al. "Nanowire spin torque oscillator driven by spin orbit torques". In: *Nature Communications* 5 (2014), p. 5616. DOI: doi:10.1038/ncomms6616. URL: http://dx.doi.org/10.1038/ncomms6616.

[45] A. Slavin and V. Tiberkevich. "Nonlinear Auto-Oscillator Theory of Microwave Generation by Spin-Polarized Current". In: *IEEE Trans. Magn.* 45.4 (2009), pp. 1875–1918. DOI: 10.1109/TMAG.2008.2009935. URL: http://dx.doi.org/10.1109/TMAG.2008.2009935.

[46] B. zyilmaz et al. "Current-Induced Excitations in Single Cobalt Ferromagnetic Layer Nanopillars". In: *Phys. Rev. Lett.* 93.17 (2004). DOI: http://dx.doi.org/10.1103/PhysRevLett.93.176604. URL: http://dx.doi.org/10.1103/PhysRevLett.93.176604.

[47] Q. Mistral et al. “Current-driven microwave oscillations in current perpendicular-to-plane spin-valve nanopillars”. In: *Appl. Phys. Lett.* 88.19 (2006), p. 192507. DOI: http://dx.doi.org/10.1063/1.2201897. URL: http://dx.doi.org/10.1063/1.2201897.

[48] W. Rippard et al. “Direct-Current Induced Dynamics in C o 90 F e 10 / N i 80 F e 20 Point Contacts”. In: *Phys. Rev. Lett.* 92.2 (2004). DOI: 10.1103/PhysRevLett.92.027201. URL: http://dx.doi.org/10.1103/PhysRevLett.92.027201.

[49] A. Ruotolo et al. “Phase-locking of magnetic vortices mediated by antivortices”. In: *Nature Nanotech* 4.8 (2009), pp. 528–532. DOI: 10.1038/nnano.2009.143. URL: http://dx.doi.org/10.1038/nnano.2009.143.

[50] S. M. Mohseni et al. “Spin Torque-Generated Magnetic Droplet Solitons”. In: *Science* 339.6125 (2013), pp. 1295–1298. DOI: 10.1126/science.1230155. URL: http://dx.doi.org/10.1126/science.1230155.

[51] Alexey V. Nazarov et al. “Spin transfer stimulated microwave emission in MgO magnetic tunnel junctions”. In: *Appl. Phys. Lett.* 88.16 (2006), p. 162504. DOI: http://dx.doi.org/10.1063/1.2196232. URL: http://dx.doi.org/10.1063/1.2196232.

[52] Alina M. Deac et al. “Bias-driven high-power microwave emission from MgO-based tunnel magnetoresistance devices”. In: *Nat Phys* 4.10 (2008), pp. 803–809. DOI: 10.1038/nphys1036. URL: http://dx.doi.org/10.1038/nphys1036.

[53] D. Houssameddine et al. “Spin transfer induced coherent microwave emission with large power from nanoscale MgO tunnel junctions”. In: *Appl. Phys. Lett.* 93.2 (2008), p. 022505. DOI: http://dx.doi.org/10.1063/1.2956418. URL: http://dx.doi.org/10.1063/1.2956418.

[54] B. Georges et al. “Origin of the spectral linewidth in nonlinear spin-transfer oscillators based on MgO tunnel junctions”. In: *Phys. Rev. B* 80.6 (2009). DOI: http://dx.doi.org/10.1103/PhysRevB.80.060404. URL: http://dx.doi.org/10.1103/PhysRevB.80.060404.

[55] Graham E. Rowlands et al. “Time Domain Mapping of Spin Torque Oscillator Effective Energy”. In: *Phys. Rev. Lett.* 111.8 (2013). DOI: http://dx.doi.org/10.1103/PhysRevLett.111.087206. URL: http://dx.doi.org/10.1103/PhysRevLett.111.087206.

[57] R. H. Liu, W. L. Lim, and S. Urazhdin. “Spectral Characteristics of the Microwave Emission by the Spin Hall Nano-Oscillator”. In: *Phys. Rev. Lett.* 110.14 (2013). DOI: http://dx.doi.org/10.1103/PhysRevLett.110.147601. URL: http://dx.doi.org/10.1103/PhysRevLett.110.147601.

[90] W. Rippard et al. “Current-driven microwave dynamics in magnetic point contacts as a function of applied field angle”. In: *Physical Review B* 70.10 (2004). DOI: 10.1103/physrevb.70.100406. URL: http://dx.doi.org/10.1103/PhysRevB.70.100406.

[91] J.C Slonczewski. "Excitation of spin waves by an electric current". In: *Journal of Magnetism and Magnetic Materials* 195.2 (1999), pp. L261–L268. DOI: 10.1016/s0304-8853(99)00043-8. URL: http://dx.doi.org/10.1016/S0304-8853(99)00043-8.

[92] Shehzaad Kaka et al. "Mutual phase-locking of microwave spin torque nano-oscillators". In: *Nature* 437.7057 (2005), pp. 389–392. DOI: 10.1038/nature04035. URL: http://dx.doi.org/10.1038/nature04035.

[93] Ferran Macià, Andrew D Kent, and Frank C Hoppensteadt. "Spin-wave interference patterns created by spin-torque nano-oscillators for memory and computation". In: *Nanotechnology* 22.9 (2011), p. 095301. DOI: 10.1088/0957-4484/22/9/095301. URL: http://stacks.iop.org/0957-4484/22/i=9/a=095301.

[94] Vladislav E. Demidov et al. "Control of spin-wave emission from spin-torque nano-oscillators by microwave pumping". In: *Phys. Rev. B* 83.6 (2011). DOI: 10.1103/physrevb.83.060406. URL: http://dx.doi.org/10.1103/PhysRevB.83.060406.

[95] H. Ulrichs et al. "Spin-torque nano-emitters for magnonic applications". In: *Applied Physics Letters* 100.16 (2012), p. 162406. DOI: 10.1063/1.4704563. URL: http://dx.doi.org/10.1063/1.4704563.

[96] S. Urazhdin et al. "Nanomagnonic devices based on the spin-transfer torque". In: *Nature Nanotech* 9.7 (2014), pp. 509–513. DOI: 10.1038/nnano.2014.88. URL: http://dx.doi.org/10.1038/NNANO.2014.88.

[97] Amikam Aharoni. "Demagnetizing factors for rectangular ferromagnetic prisms". In: *J. Appl. Phys.* 83.6 (1998), p. 3432. DOI: 10.1063/1.367113. URL: http://dx.doi.org/10.1063/1.367113.

[98] Arne Vansteenkiste et al. "The design and verification of MuMax3". In: *AIP Advances* 4.10 (2014), p. 107133. DOI: 10.1063/1.4899186. URL: http://dx.doi.org/10.1063/1.4899186.

[99] N. Vlietstra et al. "Simultaneous detection of the spin-Hall magnetoresistance and the spin-Seebeck effect in platinum and tantalum on yttrium iron garnet". In: *Physical Review B* 90.17 (2014). DOI: 10.1103/physrevb.90.174436. URL: http://dx.doi.org/10.1103/PhysRevB.90.174436.

Chapter 6

Easy plane spin Hall oscillator with NiCo free layer

The cone angles for Permalloy (Py) based spin Hall oscillators (SHO), as shown in the previous two chapters, have been limited to $\sim 20^o$ due to the squashed (elliptical) magnetization trajectories along the out-of-plane (OOP) axis, the z-axis as shown in Fig. 6.1(a), caused by the demagnetization field[41]. When self-oscillations are excited, the magnetization will follow a trajectory such that the energy supplied by the spin torque cancels out with the

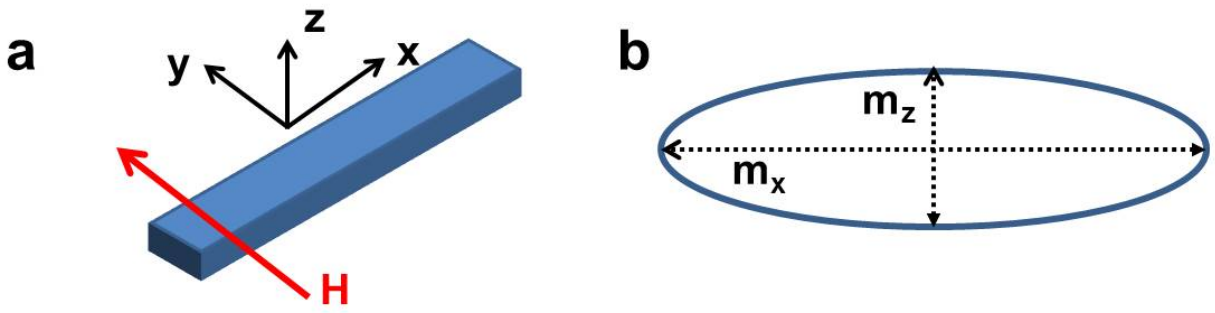

Figure 6.1: **Magnetization trajectory. (a)** Illustration of a ferromagnetic nanowire and its **(b)** self-oscillatory magnetization trajectory when only shape anisotropy is present and an external magnetic field along the y-axis.

energy lost from Gilbert damping in the system. Since the magnetization is restricted to a unit sphere and the self-oscillatory state is excited about the y-axis, the polarization axis of the spin current from the spin Hall effect, the m_x will be maximum when m_z is minimum and vice versa. The energy at both of these points are equal therefore the effective magnetic field must be equal as well. This means, how far the magnetization tilts in each axis is determined by the magnetic anisotropy energy along that axis such that the larger the energy, the smaller the tilt towards it. An illustration of the magnetization trajectory of the Py based SHO is shown in Fig. 6.1(b) where the anisotropy field is largest when $m_z = 1$ and smallest when $m_x = 1$. Therefore, when self-oscillations are excited, the trajectory forms an ellipse-like shape. Due to the magnetization being restricted to the unit sphere, m_y will also oscillate leading to a time-varying magnitude of spin torque.

If additional magnetic anisotropy is introduced along the z-axis such that it cancels out the demagnetization energy, then the maximum tilt along the x-axis and z-axis will be the same thus creating a circular orbit. This then eliminates the oscillations about m_y leading to a static magnetitude of spin torque. This ideal case of magnetic anisotropy for SHO is called easy-plane magnetic anisotropy and allows the magnetization to rotate fully in the x-z plane thus maximizing output power. This chapter covers the thin film growth, micromagnetic simulations, and device testing necessary to produce such samples along with preliminary microwave signal generation results.

6.1 Introduction

One of the requirements for spin torque oscillators (STO) to see pratical use is large output power. In order to meet this requirement, the device needs to have high magnetoresistance and large amplitude of magnetization oscillations. Typically, STOs have reduced amplitudes of oscillations due to the high cost of energy for the magnetization to rotate OOP. This is due

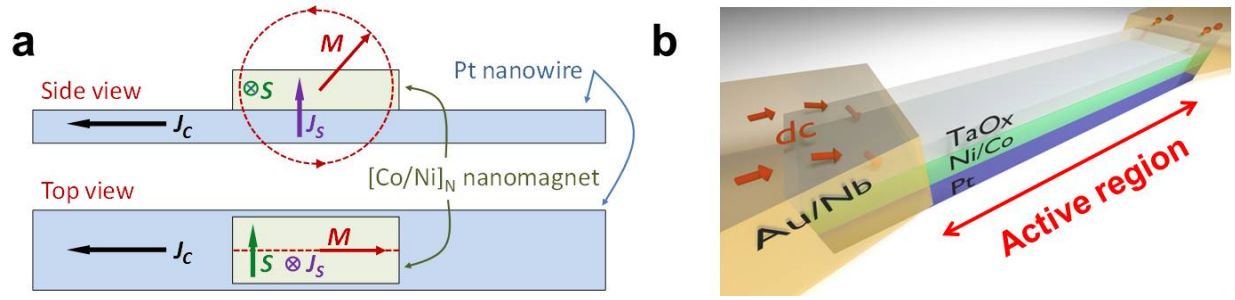

Figure 6.2: **Easy-plane spin Hall oscillator. (a)** Schematic of easy-plane spin Hall oscillator utilizing platinum as the spin current source and Co/Ni superlattice nanomagnet as the magnetic free layer. When easy-plane anisotropy is present normal to the spin polarization and the self-oscillatory state is excited, the magnetization can rotate fully in the easy-plane. **(b)** Schematic of easy-plane spin Hall oscillator where the nanomagnet is replaced with a nanowire.

to the demagnetization field which tends to align the magnetization along the longest axis of the device. To overcome this, interfacial OOP magnetic anisotropy can be introduced which will lower the energy for the OOP state and if equal to the demagnetization energy, will create an easy-plane magnetic anisotropy normal to the in-plane short axis of the device[100]. For a spin Hall oscillator (SHO), this plane will then also be normal to the spin polarization of the spin current generated by the spin Hall material that is injected into the ferromagnetic layer as shown in Fig. 6.2. Therefore, when a saturating magnetic field is applied normal to the easy-plane and dc current bias is applied to the sample in the anti-damping configuration, the magnetization can fully rotate in the easy-plane thus achieving maximum power output for the device. The device can either be a nanomagnet, Fig. 6.2(a), or a nanowire, Fig. 6.2(b), with the long axis parallel to the Pt nanostripe and each has its advantages. It is easier to acheive a single domain state in the nanomagnet compared to the nanowire structure however the fabrication is harder and magnetoresistance is smaller due to additional shunting paths in the former rather than the latter. Therefore, the nanowire structure is used for this study.

In order to introduce interfacial OOP magnetic anisotropy, the magnetic layer is changed from Permalloy to a Co/Ni superlattice. When Ni and Co are grown fcc with (111) OOP texture at a 2:1 ratio of thickness, the magnetization is pulled OOP due to

the anisotropy field generated at the interface between Ni and Co[101,102]. This arrises from symmetry breaking and the number of valence electrons shifting the Fermi energy to different bands than the bulk that favor OOP magnetization due to spin orbit coupling[35]. This field scales inversely with the thickness of each individual layer therefore, this anisotropy energy can be tuned by changing the thickness of the layers. There will also be an additional interfacial OOP magnetic anisotropy created at the Pt/Co and Ta/Ni interfaces due to spin orbit coupling that is inversely proportional to the thickness of the total magnetic material rather than the individual layer thickness. Additionally, bulk OOP magnetic anisotropy is present due to the strain of the film from growing the magnetic layers on Pt that depends on the ratio between the thickness of the total magnetic material and the characteristic relaxation length since the strain is reduced as the thickness increases.

$$K_{eff}^{OOP} = \frac{K_{Pt/Co}^{s} + K_{Ta/Ni}^{s} + (2n-1)K_{Co/Ni}^{s}}{t_m} + K_{strain}^{v}[\frac{t_s}{t_m}] \qquad t_m = 3nt_{Co} \tag{6.1}$$

Due to the different origins of perpendicular magnetic anisotropy (PMA), careful characterization needs to be done for multiple wafers in order to determine the right superlattice stack for the desired size of the device.

6.2 Thin film characterization

The first step of characterization is checking the texture of the films grown. A thin Pt seed layer was sputtered on a c-plane sapphire substrate at 585^o C and annealed for 1 hour[42]. After cooling to room temperature and Ar plasma cleaning the surface, an additional 2 nm of Pt was deposited at room temperature along with the Co/Ni superlattice and the capping layer that naturally oxidizes. For the x-ray diffraction samples, $[Co(0.5)/Ni(1)]_{10}$ and a Al(2) capping layer samples were used. The OOP texture of the film is revealed in Fig. 6.3(a) where the (111) and (222) peaks are present for both Pt and the Co/Ni superlattice

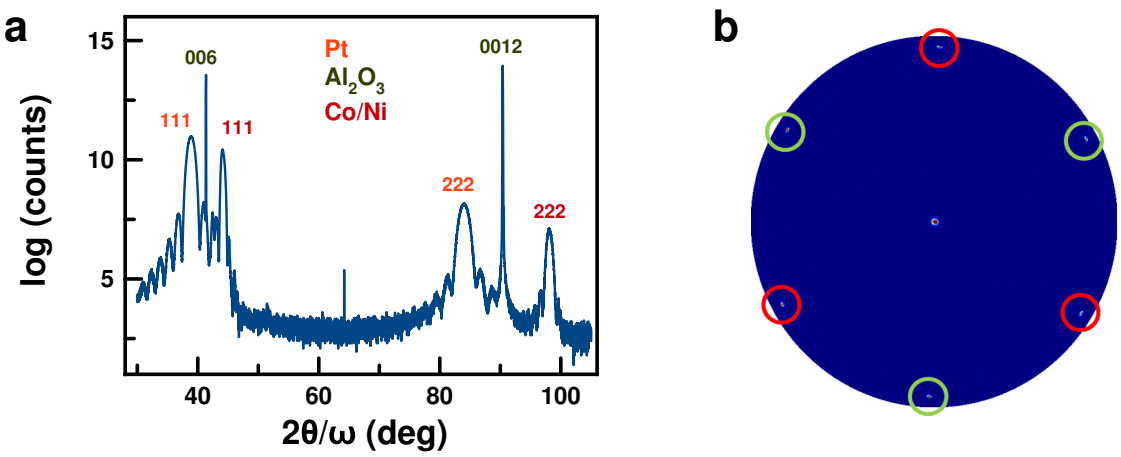

Figure 6.3: **X-ray diffraction characterization of Co/Ni films.** **(a)** Out-of-plane texture of Pt(7)/$[Co(0.5)/Ni(1)]_{10}$/AlOx(2) thin film which shows (111) texture for Pt, Co and Ni without phase impurities. **(b)** Pole figure about Pt (111) which shows in-plane texture with 60^o twinning.

while the other phases are absent. Due to the similar crystal structures of Ni and Co, their individual peaks are inseperable and are instead seen as an average of both. The presence of Pendelösung fringes indicates smooth films which is necessary for good PMA[43]. In order to check in the in-plane texture of the films, a pole figure measurement was performed about the (111) peak of Pt which is shown in Fig. 6.3(b). The expected 3 fold symmetry for a fcc (111) plane is seen with a 60^o rotated twin common for fcc materials grown on c-plane hcp substrates[42]. Therefor, high qualtiy films were grown that are capable of strong PMA.

In order to measure the magnetic anisotropy field of the thin films, B_{eff}, field domain in-plane inductive ferromagnetic reasonance was utilized at room temperature. The effective magnetic anisotropy is the combination of both shape anisotropy and PMA which is shown in eq. (6.2) where B_{eff} is in Gauss, M_s is the average saturation magnetization in emu/cm^3 and K_{eff}^{OOP} is the OOP magnetic anisotropy energy in J/m^3.

$$B_{eff} = 4\pi M_s - 10 * \frac{2K_{eff}^{OOP}}{M_s} \tag{6.2}$$

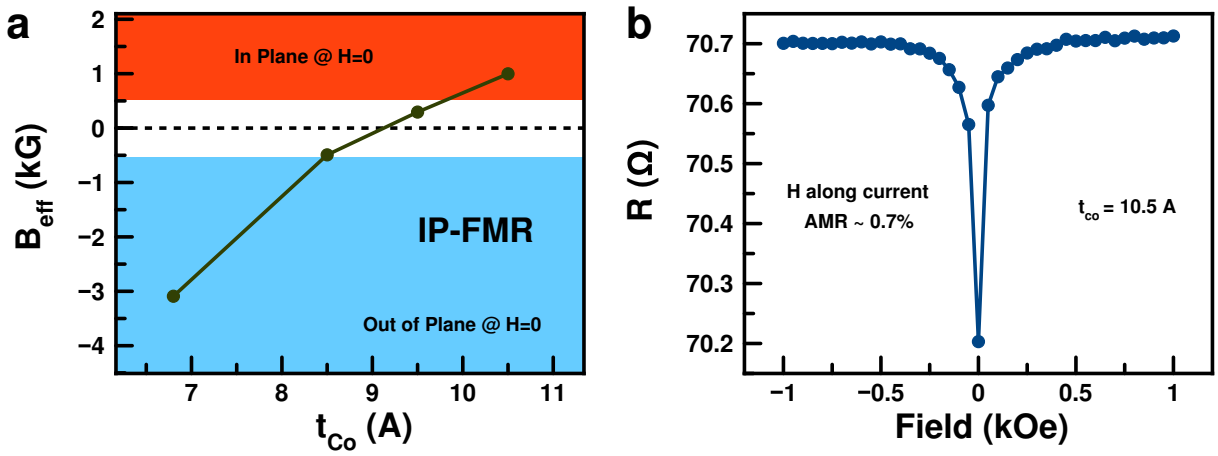

Figure 6.4: **Magnetic properties of Co/Ni films. (a)** Magnetic anistropy of Pt(6)/ $[\mathrm{Co}(t_{Co})/\mathrm{Ni}(2t_{Co})]_2$/TaOx(2.5) thin films determined by in-plane inductive ferromagnetic reasonance. Negative B_{eff} (blue region) results in OOP magnetization at zero field while postive (red region) results in IP magnetization with the crossover point happening at $t_{Co} \approx 9\mathring{A}$. **(b)** Anisotropic magnetoresistance verses magnetic field applied colinear to the electric current for the $t_{Co} = 10.5\mathring{A}$ film shows an MR of $\sim 0.7\%$.

Films consisting of Pt(6)/$[\mathrm{Co}(t_{Co})/\mathrm{Ni}(2t_{Co})]_2$/TaOx(2.5) were used where t_{Co} was varied from 6.5 to 10.5 $\mathring{A}$ and the results are shown in Fig. 6.4(a). For $t_{Co} = 6.5$ $\mathring{A}$, $B_{eff} = -3.091$ kG indicating the film is OOP at zero magnetic field while for $t_{Co} = 10.5$ $\mathring{A}$, $B_{eff} = 998$ kG which means the film is IP at zero magnetic field with the transition occuring around $t_{Co} \sim 9$ $\mathring{A}$. Since patterning the films results in reduced in-plane magnetic anisotropy due to the reduction of the OOP demagnetization term, a film with $B_{eff} \sim 1.5 - 2.5$ kG is required. Due to origins of the PMA, there will be a temperature dependence of the magnetic anisotropy. Therefore, optimization of the thickness of the layers will need to be done at the device level based on the desired size of the device and operating temperature. The resistance verses magnetic field applied collinear to the dc current bias for the $t_{Co} = 10.5$ $\mathring{A}$ film is shown in Fig. 6.4(b) which shows a sufficient value of AMR which is $\sim 0.7\%$.

6.3 Micromagnetic calculations of auto-oscillatory dynamics

In order to understand the characteristics of the nanowire SHO when at and near the easy-plane magnetic anisotropy case, micromagnetic simulations using MuMax^3 were performed[98]. A 2.5 micron x 45 nm x 6 nm nanowire with $M_s = 725\ emu/cm^3$ (weighted average between Co and Ni) was simulated with a magnetic field of 3000 G applied 5^o off the hard axis of the magnetic easy-plane and a bath temperature of 0 K. This means the shape anisotropy is constant throughout the simulations. The wire was broken up into 512 x 8 x 1 cells, with the x-axis being along the nanowire axis, y-axis being the in-plane short axis which is normal to the easy-plane, and the z-axis being the OOP direction. An exchange value of J_{ex} = 10e-12 J/m, damping constant of $\alpha = 0.03$, spin Hall angle of $\alpha_{SH} = 0.07$ and a Dzyaloshinskii-Moriya strength of D = 0.44e-3 J/m^2 was used[103–105]. The active region size, defined as the distance between the leads where dc current flows through the sample, was varied between 75, 250 and 500 nm while the OOP magnetic anisotropy constant, K_p, was varied between 244 (near perfect easy-plane case), 256, 273 and 285 kJ/m^3. The Oersted field was either turned off or scaled linearly with the dc current density in the active area of the device, J_{dc}, such that $H_{Oe} = 32\ G$ at J_{dc} = 8e7 A/cm^2 in the active region which reduces the internal field locally. Outside of the active region, the Oersted field is assumed to be 1/5 the strength and in the opposite direction than that of the active region. This is due to the current flowing through the leads rather than through the Pt layer which increases the distance between the current and the magnetization. The magnetization was allowed to evolve to steady state dynamics before being analyzed.

In order to study the effects of the PMA strength on the auto-oscillation characteristics, micromagnetic simulations were done without an Oersted field present and an active region of 75 nm shown in Fig. 6.5. The emission spectra of the x-component of

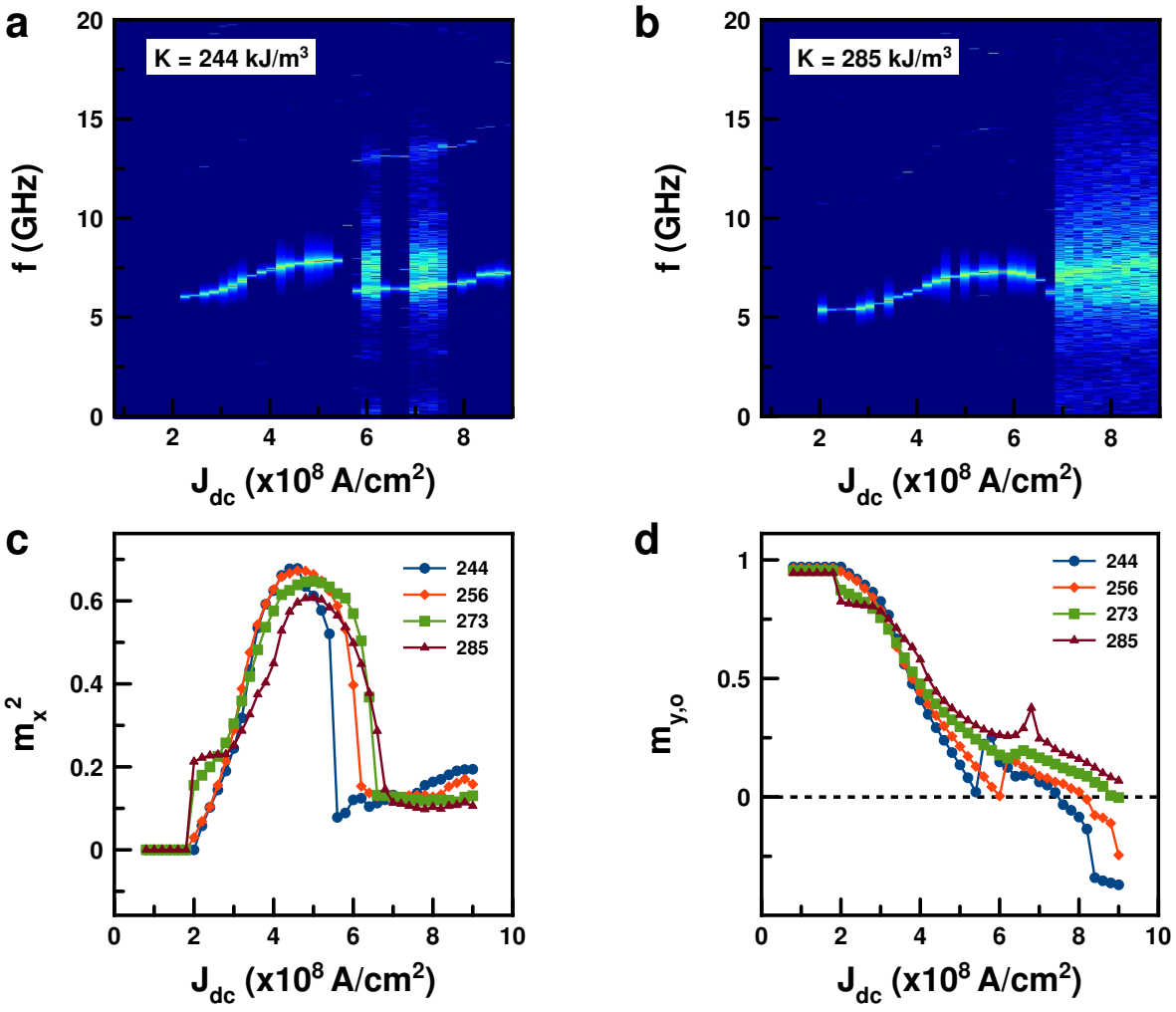

Figure 6.5: **Anisotropy dependence of the emission spectra.** Micromagnetically calculated emission spectra verses dc current bias without an Oertsed field for a 30 nm wide nanowire with 75 nm long active region with a magnetic field of 3000 Oe at an angle of $\theta = 5^o$ for the OOP anisotropy energy of **(a)** $K = 244\ kJ/m^3$, which is the easy-plane anisotropy case, and **(b)** $K = 285\ kJ/m^3$. **(c)** Integrated power of the emission spectra normalized to 1 and **(d)** average magnetization normal to the easy-plane as a function of dc current bias for $K = 244\ kJ/m^3$ (blue circles), $K = 256 kJ/m^3$ (orange diamonds), $K = 273\ kJ/m^3$ (green squares) and $K = 285\ kJ/m^3$ (burgundy triangles). Dashed line in **(d)** indicates when magnetization crosses the hemisphere such that negative values of $m_{y,o}$ corresponds to magnetization parallel to the spin polarization of the spin current.

the magnetization, m_x, as a function of dc current bias, J_{dc}, for the easy-plane case of $K = 244\ kJ/m^3$ and the weakly easy-plane case, when the magnetic anisotropy slightly favors one axis over the other, of $K = 285\ kJ/m^3$ is shown in Fig. 6.5(a) and (b) respectfully. For $K = 244\ kJ/m^3$, single-mode, stabile oscillations are found over a large current range. At first, only the first harmonic is present and the frequency of the mode is constant but experiences a blue shift shortly after the critical current is reached. The frequency stops blue shifting before a state change occurs at $J_{dc} = 5.6e8\ A/cm^2$ where the frequency jumps downward and partially destabilizes along with the 2nd harmonic now existing. The frequency remains relatively static with a slight blue shift and goes through periods of stability and instability. The characteristics for the $K = 285\ kJ/m^3$ case is very similar however the state change occurs later, $J_{dc} = 6.8e8\ A/cm^2$, with the frequency jump being smaller and the oscillations completely destabilze after the state change.

To better understand the predicted dynamics, the integrated power of $m_x(t)$ as a function of dc current bias is shown in Fig. 6.5(c) for various values of PMA where $m_x^2 = 1$ corresponds to 360^o rotation of the magnetization in the easy plane. First, the oscillations achieve very large cone angles, $\sim 70\%$ of the possible maximum output power, and is reduced as K is farther from the easy-plane case although still remains large. Second, the integrated power quickly drops at the same current density as the state change observed in the emission spectra. The nature of this state change is exposed by looking at the average magnetization in the y-axis, $m_{y,0}$, as a function of the dc current density. Initially, the magnetization points along the field direction leading to $m_{y,o} \approx 1$ and then reduces as the oscillation amplitude increases. As $m_{y,o} \rightarrow 0$, there is a sudden increase in $m_{y,o}$ at the same current density that the state change is observed in the emission spectra along with the sudden decrease in integrated power. After the state change, $m_{y,o}$ keeps decreasing and eventually crosses hemispheres such that the magnetization is in the same hemisphere as the applied magnetic field. During this process, the oscillations are unstable until another state change occurs, as seen by the reduction of $m_{y,o}$ for $K = 244\ kJ/m^3$ at $J_{dc} = 8.4e8\ A/m^2$.

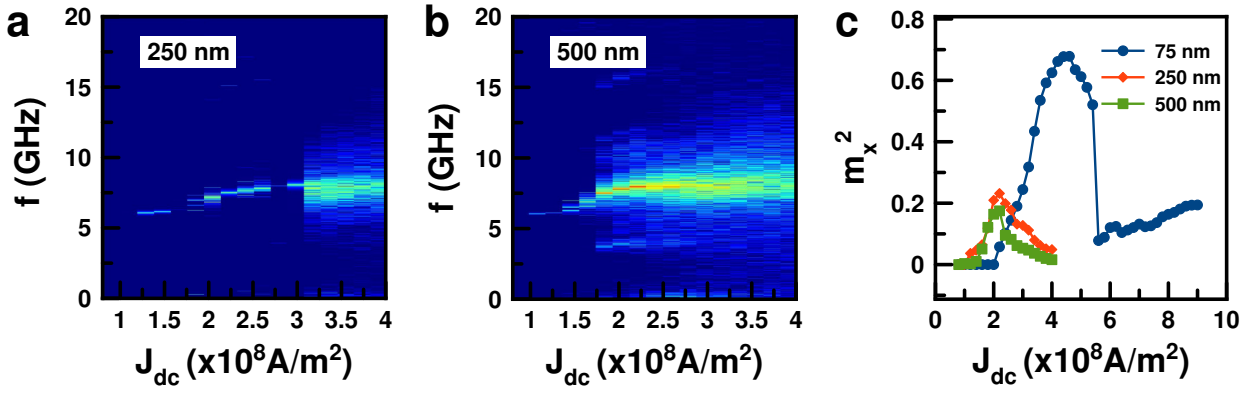

Figure 6.6: **Active region size dependence of the emission spectra.** Micromagnetically calculated emission spectra verses dc current bias without an Oersted field for a 30 nm wide nanowire with a magnetic field of 3000 Oe at an angle of $\theta = 5^o$ for the OOP anisotropy energy of $K = 244\ kJ/m^3$ for an active region length of **(a)** 250 nm and **(b)** 500 nm. **(c)** Integrated power of the emission spectra normalized to 1 for the active region lengths of 75 nm (blue circles), 250 nm (orange diamonds) and 500 nm (green squares).

The active size dependence on the self-oscillatory dynamics without the presence of an Oersted field is shown in Fig. 6.6 where K is fixed at 244 kJ/m^3. The dc current bias dependence of the emission spectra for the active region size of 250 nm and 500 nm is shown in Fig. 6.6(a) and (b) respectfully. A single mode is excited in both cases still and a blue shift is seen in the frequency with increasing J_{dc}, however, the oscillator destabilizes much sooner as the width increases resulting in stability up to $J_{dc} = 3.0e8\ A/cm^2$ and $J_{dc} = 1.2e8\ A/cm^2$ for 250 and 500 nm respectfully. The integrated power, shown in Fig. 6.6(c), is also dramatically reduced when the active size is increased. Interestingly, the integrated power does not show a sharp decline after reaching the maximum integrated power as present in the 75 nm long oscillator but rather, the power gradually declines after reaching the maximum value.

The influence of the Oersted field on the oscillatory dynamics is shown in Fig. 6.7. The dc current bias dependence on the emission spectra is shown in Fig. 6.7(a) with an active region size of 250 nm and K= 244 kJ/m^3. Again, the notable blue shift of the frequency is seen, however, the oscillator is stable to a higher dc current bias of $J_{dc} = 3.4e8\ A/m^2$ than without the presence of the Oersted field. The integrated power and $m_{y,o}$ for 250 nm (blue) and 500 nm (burgundy) with (shapes) and without (dashed line) the Oersted field is shown

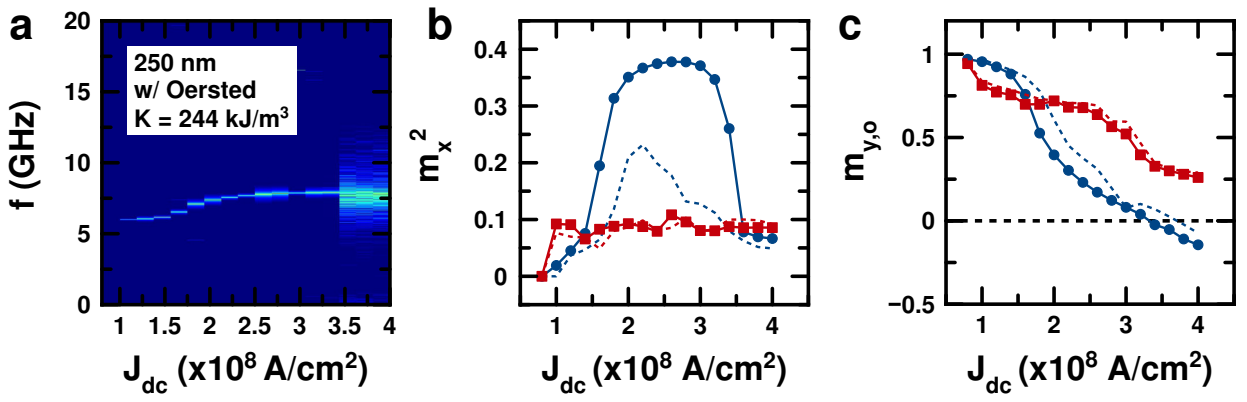

Figure 6.7: **Oersted field dependence of the emission spectra.** **(a)** Micromagnetically calculated emission spectra verses dc current bias with an Oersted field of 32 Oe at $J_{dc} = 8e7\ A/cm^2$ that scales linearly for a 30 nm wide nanowire with a magnetic field of 3000 Oe at an angle of $\theta = 5^o$ for the OOP anisotropy energy of $K = 244\ kJ/m^3$ and an active region size of 250 nm. **(b)** Integrated power of the emission spectra normaized to 1 and **(c)** average magnetization normal to the easy-plane as a function of dc current bias for $K = 244\ kJ/m^3$ (blue) with an Oersted field (circles) and without an Oersted field (dashed line) and for $K = 285\ kJ/m^3$ (burgundy) with an Oersted field (squares) and without an Oersted field (dashed line). Dashed line in **(c)** indicates when magnetization crosses the hemisphere such that negative values of $m_{y,o}$ corresponds to magnetization parallel to the spin polarization of the spin current.

in Fig. 6.7(b) and (c) respectfully. For the 250 nm case, the presence of the Oersted field restores the characteristics seen in the 75 nm case without an Oersted field. The integrated power reaches a much higher value of 0.38, stays near the maximum value over a larger dc current bias range, and the decline after reaching the maximum power is much sharper. Interestingly, $m_{y,o}$ is only weakly affected by the presence of the Oersted field and no state change is seen even though the magnetization crosses hemispheres which is qualitatively different than the 75 nm case. For the 500 nm case, the Oersted field has little impact on the oscillator characteristics and the integrated power hovers near 0.1 for all J_{dc}.

In conclusion, in order to produce the highest output power for an easy-plane SHO, the active region should be small in order to promote uniform oscillations due to the higher cost of exchange energy for higher order modes in smaller active regions. Also, the presence of the Oersted field creates a spin wave well which helps isolate the active region from the rest of the device. This prevents the energy from being pumped away from the active region

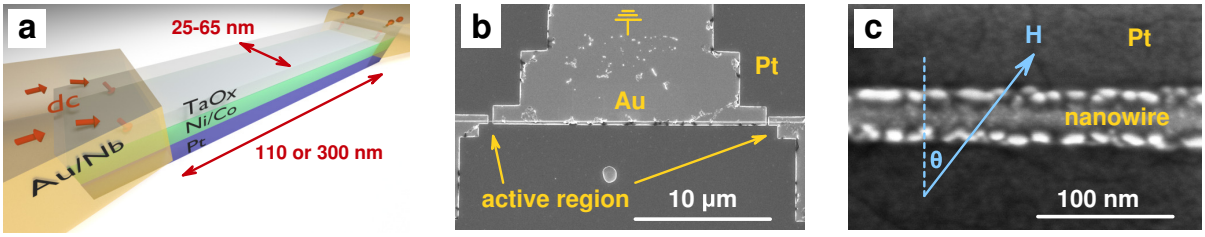

Figure 6.8: **Device Design.** **(a)** Device schematic for nanowire easy-plane spin Hall oscillator where Pt provides spin current and free layer consists of Co(t_{Co}) and Ni($2t_{Co}$) bilayer which is then capped by naturally oxidized Ta. Electric leads defines active region of spin Hall oscillator which is either 110 or 300 nm long. The width of the wire varies from 25 to 65 nm. **(b)** Birds eye view scanning electron microscope image of the 3 terminal device where electric current is applied through either edge lead and extracted through the middle lead. The seperation between the active regions are either 10 or 20 μm long. Scale bar is 10 μm **(c)** Close up SEM image of nanowire consisting of Co, Ni, TaOx and HSQ. The magnetic field is applied at an angle θ with respect to the hard axis (in-plane short axis of the nanowire). Scale bar is 100 nm. The background in **(b)** and **(c)** is Pt which is etched away before measuring.

allowing for higher amplitude of oscillations. Lastly, as the OOP magnetic anisotropy is increased away from the easy-plane case, the integrated power decreases slowly allowing for a rather large tolerance in PMA for a working easy-plane SHO.

6.4 Experimental results

6.4.1 Device

Using the results from section 6.4.1, 3-terminal devices were fabricated as shown in Fig. 6.8 such that 2 SHO are possible per device. A schematic for a single SHO is shown in Fig. 6.8(a) where dc current bias is injected through the lead on the left which passes through the Pt(7)/Co(1.5)/Ni(3)/TaOx(2.5) nanowire that is varied between 25 and 65 nm wide in different devices and exits through the lead on the right that is 110 or 300 nm away. This separation between the leads defines the active region of the SHO. Fig. 6.8(b) is a scanning electron microscope (SEM) image of the device where the nanowire is 40 microns long and

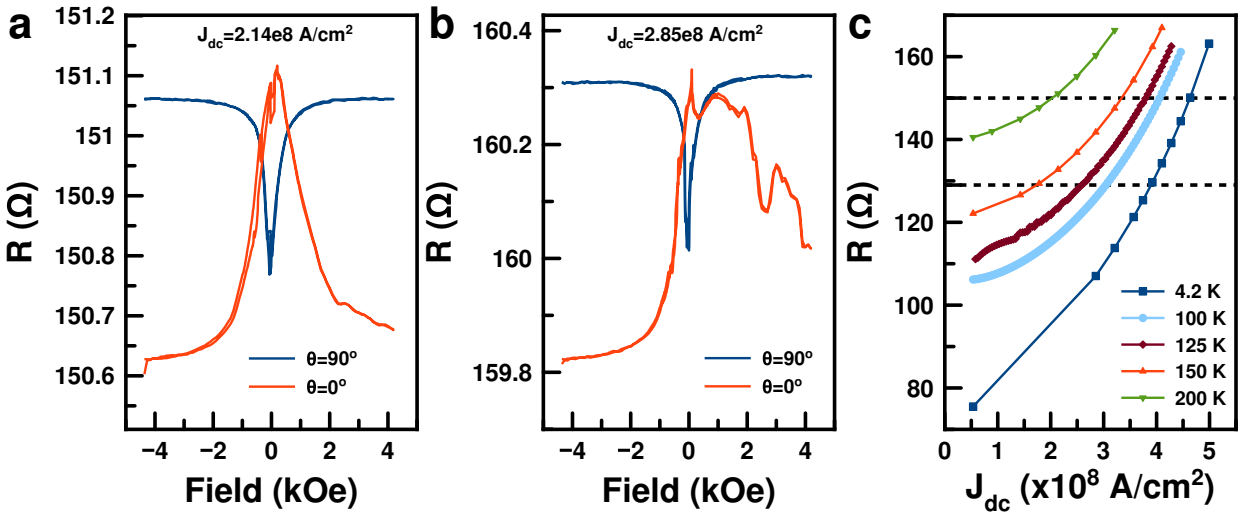

Figure 6.9: **Resistance of 50 nm wide nanowire with 300 nm long active region.** Resistance of Pt(7)/Co(1.5)/Ni(3)/TaOx(2.5) 51 nm wide nanowire with 300 nm long active region at a bath temperature of $T_b = 200\ K$ verses external magnetic field applied at $\theta = 90^o$ (blue) and $\theta = 0^o$ (orange) with a dc current bias of **(a)** $J_{dc} = 2.14e8\ A/cm^2$ and **(b)** $J_{dc} = 2.85e8\ A/cm^2$. **(c)** Resistance verses dc bias current with a saturating external magnetic field applied at $\theta = 0^o$ at bath temperatures of $T_b = 4.2$ K (dark blue squares), 100 K (light blue circles), 125 K (burgundy diamonds), 150 K (orange up triangles) and 200 K (green down triangles). Inbetween horizontal dashed lines designates easy-plane anisotropy region.

the distance between the 2 active regions is either 10 or 20 microns. The left and right leads serve as dc current injectors for their respective active regions while the middle lead is grounded. Fig. 6.8(c) is a close up SEM image of a $\sim$ 40 nm wide nanowire device where the magnetic field, H, is applied at an angle, θ, away from hard axis of the nanowire. The Pt in the background seen in both SEM images is removed before measuring the devices.

6.4.2 Charactization

The resistance of a 51 nm wide nanowire with a 300 nm active region under various bath temperatures T_b, dc bias currents J_{dc} and magnetic field H is shown in Fig. 6.9. The resistance of the sample is shown in eq. (6.3) where T_b is the bath temperature, R_o is the resistance of the sample at $J_{dc} = 0\ A/cm^2$ and $T_b = 0$ K, c is the rate the resistance increases with increasing sample temperature in Ω/K, b is the efficiency of the dc power converting

into sample temperature in K/W, A is the cross-sectional area of the wire, ρ_{AMR} is the AMR ratio, S_N is the transverse Seebeck coefficient in V/K and ΔT_z is the OOP thermal gradient.

$$R = \frac{T_b + \frac{R_o}{c}}{\frac{1}{c} - b * (J_{dc} * A)^2}(1 + \rho_{AMR} * m_x^2) + \left|\frac{S_N * \Delta T_z[J_{dc}]}{J_{dc} * A}\right| * m_y \tag{6.3}$$

The first term is the base resistance of the sample that is assumed to linearly depend on sample temperature due to the increased electron-phonon scattering in the all metallic sample at elevated temperatures. This is true over small temperature ranges near the Debye temperature, $\Theta_D^{Pt} = 240K$ and $\Theta_D^{Py} \approx 450K$, and at high temperatures which is the case for this work. The sample temperature depends on both the bath temperature and the dc power being dissipated by the device and is the dominate term for the resistance. The second term is the AMR term that is the dominate magnetoresistive term at low bias currents.

The third term is the anomalous Nerst effect (ANE) term that arrises from the thermal gradient produced by the ohmic heating in the sample. The ANE is the thermoelectric equivalent of the anomalous Hall effect where the thermal gradient in the OOP direction in the Co/Ni layer produces a voltage gradient perpendicular to the magnetization due to spin orbit coupling. Since the power dissipated by the device scales with J_{dc}^2, the thermal gradient will too therefore the ANE term is the strongest magnetoresistive term at higher current densities.

The resistance of the sample at $T_b = 200$ K with $\theta = 90^o$ (blue) and 0^o (orange) for $J_{dc} = 2.14e8\ A/cm^2$ and $J_{dc} = 2.85e8\ A/cm^2$ is shown in Fig. 6.9(a) and (b) respectfully. When $\theta = 0^o$, the resistance is minimum at saturating negative magnetic fields since $m_z \to 0$ and $m_y \to -1$. As the field is increased, the resistance increases due to the magnetization rotating towards the nanowire axis which increases the AMR and ANE terms. Once the field reaches postive values, the AMR term starts decreasing again while the ANE term keeps

increasing due to the magnetization being pulled back towards the nanowire short axis. The ANE term is larger for the higher current density due to the increased thermal gradient from the increased ohmic heating. Also visable are spin torque effects on the magnetization that is in the anti-damping configuration when the magnetic field is postive. The complex dependence of the resistance on positive fields is likely due to different oscillatory states being excited at different field values.

When $\theta = 90^o$, the ANE term is absent as expected since the magnetic field is parallel to the nanowire axis which minimizes m_y. The AMR term is maximized at high fields and is reduced as $H \rightarrow 0$ which is indicative of the magnetization rotating OOP. The resistance at zero field for $\theta = 90^o$ and $\theta = 0^o$ doesn't match due to thermal drift of the sample, however, the resistance does lie inbetween the maximum and minimum values which indicates a tilted or mixed state. The field that the resistance reaches 90% of the maximum value is greater for the lower current density than the larger which means the magnetic anisotropy shifts more IP at higher sample temperatures. Therefore, the sample temperature needs to be monitored carefully during self-oscillatory measurements such that the magnetic anisotropy can be determined. This however, allows the magnetic anisotropy to be tuned by altering the bath temperature such that different regiems can be explored. The combination of this two facts leads to a complicated J_{dc} and T_b dependence on the oscillatory characteristics.

In order to map the magnetic anisotropy to its J_{dc} and T_b pairing, the resistance when $\theta = 90^o$ and an postive saturating magnetic field is applied is shown in Fig. 6.9(c) for various bath temperatures and current densities. Inbetween the two horizontal dashed lines is when the magnetic anisotropy is near the easy-plane case found by inspecting the saturation fields for the resistance verses magnetic field as shown in Fig. 6.9(a) and (b). Therefore, self-oscillatory measurements will be made only when the resistance of the sample is between 129 and 150 Ω.

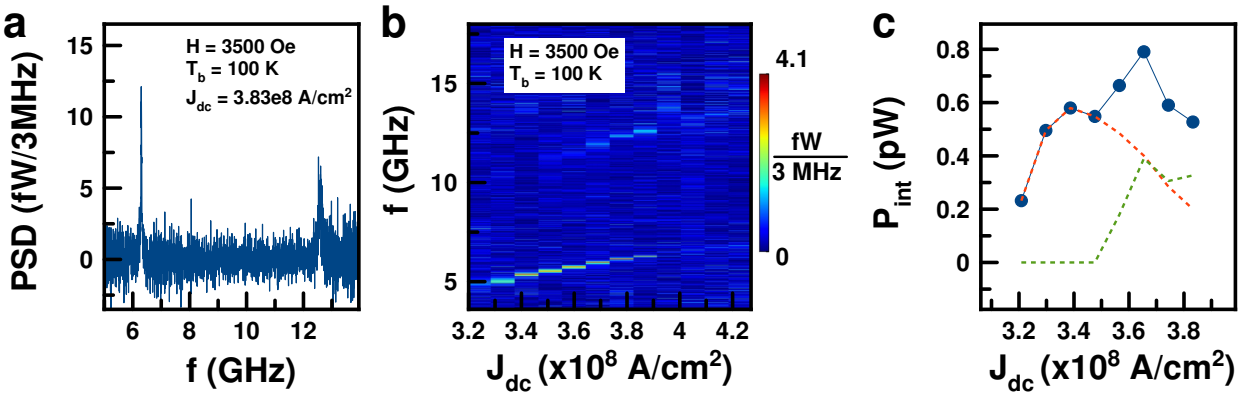

Figure 6.10: **Experimental emission spectra.** **(a)** Example emission spectra from 51 nm wide nanowire with 300 nm long active region with a magnetic field of H=3500 Oe at an angle of $\theta = 0^o$ with a dc current bias of $J_{dc} = 3.83e8\ A/cm^2$ and a bath temperature of $T_b = 100$ K where the first and second harmonic signals are seen. **(b)** Current dependence of the emission spectra shown in **(a)** over the dc current bias range that exists in the easy-plane region. **(c)** The ingrated power of the first harmonic (orange dashed) and second harmonic (green dashed) and the sum (blue circles) for the spectra shown in **(b)**.

6.4.3 Microwave Emission

The emission from the 51 nm wide and 300 nm long active region at H=3500 Oe, $\theta = 0^o$ and $T_b = 100$ K is shown in Fig. 6.10. The emission spectra at $J_{dc} = 3.83e8\ A/cm^2$ is shown in Fig. 6.10(a) where the first and 2nd harmonic of the signal is seen and the magnetic anisotropy is IP favored easy-plane. The unexpected presence of the first harmonic of the signal can originate from either the AMR and the average magnetization being tilted away from the y-axis, from either misalignment of the field or incomplete saturation of the magnetization, or from the ANE and the magnetization undergoing an orbit that oscillates about m_y. The current dependence of the emission spectra is shown in 6.10(b) over the dc current bias range where the magnetic anisotropy is near easy-plane. A blue shift in the frequency as J_{dc} increases is seen as expected from the micromagnetic simulations.

The integrated power of the first (orange dashed) and second (green dashed) harmonic of the signal with the summation (blue) of both is shown in 6.10(c). At low J_{dc}, the second harmonic is absent and the first harmonic increases with increasing J_{dc}. At

$J_{dc} = 3.48e8\ A/cm^2$, the first harmonic starts decreasing and the second harmonic starts increasing. The integrated power of the first harmonic continues decreasing while the second harmonic reaches a maximum at $J_{dc} = 3.65e8\ A/cm^2$, hovers near the maximum until $J_{dc} = 3.83e8\ A/cm^2$, and then sharply decreases to 0. This suggests the presence of the first harmonic is caused by the tilting of the magnetization away from the y-axis since the saturation field is lower at higher dc bias currents. This leads to a reduced first harmonic and a stronger second harmonic as the magnetization becomes more aligned to the magnetic field due to the angular dependence of AMR.

The decrease of the integrated power at high J_{dc} can be caused by two mechanism. The first is a gradual process and is due to nonlinear linewidth broadening which spreads out the power of the signal over a larger frequency range. This causes the signal to noise ratio to reduce which ultimately leads to the signal becoming undetectable even though the actual integrated power did not decrease. The second possibility is an abrupt process where a state change occurs such that the new oscillation profile produces lower output power than the previous state and if low enough, be undetectable. Since the decrease of the integrated power is sharp and the linewidth of the signal is small before the decrease happens, the likely mechanism is a state change where the signal is now undetectable.

Lastly, the integrated power is very low at all J_{dc}. One possible explanation is that the easy-plane SHO state is not being achieved. In order to do so, different bath temperatures should be investigated that will allow different J_{dc} to be used such that a different phase space of the SHO dynamics can be reached. Also, a reduced active region should be investigated since micromagnetic simulations revealed smaller active regions increases the region where the easy-plane SHO is seen. Another possibility is that the easy-plane SHO is being achieved, however the excited state might be spatially non-uniform. This would result in a reduced signal even if the magnetization oscillations are large due to only a part of the active region would be producing a signal. The spatial profile of the excited self-oscillatory modes should

be investigated with micromagnetic simulations in order to determine if this is the cause. The reduction of the active region size would also help alleviate this problem as the exchange energy will become more dominate.

Future studies should focus on improving the stability of the magnetic anistropy at different current densities. Ideally, the current density should only affect the amount of spin torque generated by the Pt layer so that the microwave emission dependence on the spin current can be analyzed. In order to do so now, the bath temperature needs to be altered for each current density in order to keep the magnetic anisotropy constant which is a very arduous process. This can be done by figuring out how to reduce the ohmic heating in the sample by adding heat sinks to the device design. Additionally, devices with smaller active region sizes should be experimentally studied as these produced the best results in micromagnetic simulations. If struggles with the nanowire easy-plane SHO still exist, a nanomagnet design should be explored as preliminary micromagnetic simulations on a 75 $\times$ 25 nm easy-plane Co/Ni nanomagnet produced larger integrated powers of the magnetization than the nanowire design. A working fabrication recipe needs to be developed along with COMSOL simulations to predict the ohmic heating.

Bibliography

[35] Gerardus Henricus Otto Daalderop. *Magnetic anisotropy from first principles*. TU Delft, Delft University of Technology, 1991.

[41] Zheng Duan et al. "Nanowire spin torque oscillator driven by spin orbit torques". In: *Nature Communications* 5 (2014), p. 5616. DOI: doi:10.1038/ncomms6616. URL: http://dx.doi.org/10.1038/ncomms6616.

[42] M.L. Hildner, T.J. Minvielle, and R.J. Wilson. "Epitaxial growth of ultrathin Pt films on basal-plane sapphire: the emergence of a continuous atomically flat film". In: *Surface Science* 396.1-3 (1998), pp. 16–23. DOI: 10.1016/s0039-6028(97)00655-9. URL: http://dx.doi.org/10.1016/S0039-6028(97)00655-9.

[43] Haydn Chen. "Observation of pendellsung fringes in reflection-section topographs of bent silicon crystals". In: *Materials Letters* 4.2 (1986), pp. 65–70. DOI: 10.1016/0167-577x(86)90051-0. URL: http://dx.doi.org/10.1016/0167-577X(86)90051-0.

[98] Arne Vansteenkiste et al. "The design and verification of MuMax3". In: *AIP Advances* 4.10 (2014), p. 107133. DOI: 10.1063/1.4899186. URL: http://dx.doi.org/10.1063/1.4899186.

[100] M T Johnson et al. "Magnetic anisotropy in metallic multilayers". In: *Reports on Progress in Physics* 59.11 (1996), p. 1409. URL: http://stacks.iop.org/0034-4885/59/i=11/a=002.

[101] G. H. O. Daalderop, P. J. Kelly, and F. J. A. den Broeder. "Prediction and confirmation of perpendicular magnetic anisotropy in Co/Ni multilayers". In: *Physical Review Letters* 68.5 (1992), pp. 682–685. DOI: 10.1103/physrevlett.68.682. URL: http://dx.doi.org/10.1103/physrevlett.68.682.

[102] M. T. Johnson et al. "Orientational dependence of the interface magnetic anisotropy in epitaxial Ni/Co/Ni sandwiches". In: *Physical Review Letters* 69.24 (1992), pp. 3575–3578. DOI: https://doi.org/10.1103/PhysRevLett.69.3575. URL: http://dx.doi.org/10.1103/PhysRevLett.69.3575.

[103] T. Kato et al. "Time-Resolved Magnetization Dynamics and Damping Constant of Sputtered Co/Ni Multilayers". In: *IEEE Transactions on Magnetics* 47.10 (2011), pp. 3036–3039. DOI: 10.1109/tmag.2011.2158082. URL: http://dx.doi.org/10.1109/TMAG.2011.2158082.

[104] Yi Wang et al. “Determination of intrinsic spin Hall angle in Pt”. In: *Applied Physics Letters* 105.15 (2014), p. 152412. DOI: 10.1063/1.4898593. URL: http://dx.doi.org/10.1063/1.4898593.

[105] Hongxin Yang et al. “Anatomy of Dzyaloshinskii-Moriya Interaction at Co / Pt Interfaces”. In: *Phys. Rev. Lett.* 115.26 (2015). DOI: 10.1103/physrevlett.115.267210. URL: http://dx.doi.org/10.1103/PhysRevLett.115.267210.

Chapter 7

Conclusion

It is widely known that spin-polarized current can excite self-oscillations in 0-dimensional (0D) systems where the ferromagnetic layer is constricted. The first spin torque oscillators (STO) where shown in nanopillar structures where all of the layers are confined to ∼100 nm structure and the spin current is generated by a ferromagnetic layer[38]. Point contact STOs soon followed where only the current was localized but a ferromagnetic layer still generated the spin current. 5 years ago, the latest type of STO was discovered that utilizes the spin Hall effect to generate a spin current, however, they were still 0D. Additionally, the majority of the excited state was a self-localizing bullet mode rather than the spin wave eigenmodes of the ferromagnetic structure. The introduction of the this type of STO called the spin Hall oscillator (SHO) however, allowed for the exploration of different dimensional STOs.

One such work was an optical study using micro-focused Brillouin light scattering (BLS) on a 2D system where a 2 μm Permalloy (Py) disk was placed atop of a platinum (Pt) stripe which generates the spin current. When spin torque was applied in the anti-damping configuration, the reduction of the saturation magnetization was observed rather than self-oscillations[39]. This was attributed to magnon scattering where magnons from the potentially

excited state where scattered to less populated states as additional spin torque was supplied to the system thus preventing any one state from reaching the threshold of self-oscillations.

These results lead to the work covered in this thesis where the the 1D case was explored by using a 190 nm wide Py/Pt nanowire. It was shown by electrical means that self-oscillations do occur and that the modes excited were shown to be the bulk and edge spin wave eigenmodes by using finite bias spin torque ferromagnetic resonance, BLS, and micromagnetic simulations. Additionally, fine splitting modes occurred due to the spin wave well created at the leads due to the jump of the Oersted field as the current exited the nanowire. It was believed that self-oscillations existed in the 1D case because of the discretized backward volume spin wave (BVSW) spectrum which restricted the magnon scattering channels. This prevented the energy supplied from the spin torque to the potentially excited state to be siphoned away to other low population states thus allowing self-oscillations.

This thesis provided evidence of this theory by reporting the self-oscillatory dynamics in various widths of a Py/Pt nanowire such that the dimension of the wire crossed over from the 1D to the 2D case. This showed that the integrated power of the bulk modes decreased with increasing width while the total number of excited modes increased. This type of behavior is consistent with increased magnon scattering near the 2D case. Additionally, the integrated power of the bulk mode in a 530 nm wide wire was shown to exponentially decay to 0 as the bath temperature was increased while the critical current decreased linearly. This is believed to occur due to increased thermal magnons which then requires less energy for the potentially excited state to reach the threshold for self-oscillations while at the same time, increase scattering out of this state once the population becomes high. Also, the angular dependence of the critical current revealed that the spin Seebeck effect is negligible for these all metallic devices.

Lastly, the effects of replacing the Py layer with a Co/Ni bilayer whose thicknesses were engineered to create an easy-plane magnetic anisotropy were explored. Micromagnetic

simulations showed that large amplitude magnetic oscillations are possible, upwards to 70% of the maximum possible power, and these oscillations are stable over a large range of currents. Additionally, a stable oscillatory state was found even after the average magnetization crossed hemispheres. Preliminary electrical measurements were performed on these devices however the measured output power is significantly smaller than expected. This is due to the difficulties of a changing magnetic anisotropy due to ohmic heating and the temperature dependence of the out-of-plane magnetic anisotropy. Future efforts should be placed into resolving this issue. Another path that should be explored is the creation of a nanomagnet easy-plane SHO. Preliminary micromagnetic simulations showed even greater potential output power than the nanowire version with more stable oscillations. These devices could provide an avenue to large power and narrow linewidth STOs.

Bibliography

[38] S. I. Kiselev et al. "Microwave oscillations of a nanomagnet driven by a spin-polarized current". In: *Nature* 425.6956 (2003), pp. 380–383. DOI: 10.1038/nature01967. URL: http://dx.doi.org/10.1038/nature01967.

[39] V. E. Demidov et al. "Control of Magnetic Fluctuations by Spin Current". In: *Phys. Rev. Lett.* 107.10 (2011). DOI: http://dx.doi.org/10.1103/PhysRevLett.107.107204. URL: http://dx.doi.org/10.1103/PhysRevLett.107.107204.